INFORMATION TO USERS

This manuscript has been reproduced from the microfilm master. UMI films the text directly from the original or copy submitted. Thus, some thesis and dissertation copies are in typewriter face, while others may be from any type of computer printer.

The quality of this reproduction is dependent upon the quality of the copy submitted. Broken or indistinct print, colored or poor quality illustrations and photographs, print bleedthrough, substandard margins, and improper alignment can adversely affect reproduction.

In the unlikely event that the author did not send UMI a complete manuscript and there are missing pages, these will be noted. Also, if unauthorized copyright material had to be removed, a note will indicate the deletion.

Oversize materials (e.g., maps, drawings, charts) are reproduced by sectioning the original, beginning at the upper left-hand corner and continuing from left to right in equal sections with small overlaps. Each original is also photographed in one exposure and is included in reduced form at the back of the book.

Photographs included in the original manuscript have been reproduced xerographically in this copy. Higher quality 6" x 9" black and white photographic prints are available for any photographs or illustrations appearing in this copy for an additional charge. Contact UMI directly to order.

U·M·I

University Microfilms International
A Bell & Howell Information Company
300 North Zeeb Road. Ann Arbor. MI 48106-1346 USA
313 761-4700 800 521-0600

Order Number 9315480

A time-pulsed positronium beam and a study of oxides on silicon using positrons

Khatri, Ravinder Kumar, Ph.D.

City University of New York, 1993

U·M·I
300 N. Zeeb Rd.
Ann Arbor, MI 48106

A TIME PULSED POSITRONIUM BEAM
AND
A STUDY OF OXIDES ON SILICON USING POSITRONS

by

Ravinder K. Khatri

A dissertation submitted to the Graduate Faculty in Physics in
partial fulfillment of the requirements for the degree of Doctor
of Philosophy, The City University of New York.

1993

This manuscript has been read and accepted for the Graduate Faculty in Physics in satisfaction of the dissertation requirement for the degree of Doctor of Philosophy.

Leonard O. Roellig

Date

Prof. Leonard O. Roellig
Chair of Examining Committee

Nov 4, 1992
Date

Joseph B. Krieger

Prof. J. Krieger
Executive Officer

Prof. Martin L. den Boer

Prof. Karl F. Canter

Martin A. Kramer
Prof. Martin Kramer

Kelvin G. Lynn
Dr. Kelvin G. Lynn

Frederick W. Smith
Prof. Frederick W. Smith

Supervisory Committee

The City University of New York

Abstract

A TIME PULSED POSITRONIUM BEAM AND A STUDY OF OXIDES ON SILICON USING POSITRONS

by

Ravinder K. Khatri

Advisor: Professor Leonard O. Roellig

The studies on rare gas solid moderators were carried out with a 350 μCi ^{22}Na radioactive source. The corrected efficiency for neon moderator in conical geometrical configuration was as high as $(1.4 \pm 0.2)\%$. The conical configuration moderator performed better by a factor of (2.2 ± 0.2) than the cylindrical configuration. A time pulsed positron beam was built to carry out investigations on the positronium formation processes and positronium beam. This beam has the capability to store low energy e^+ in a magnetic bottle, with a magnetic bottle at one end and an electrostatic mirror at the other. These stored e^+ are then bunched to form a pulse with a buncher. The bunched beam had a FWHM of 17 nsec and contained 1 to 2 e^+/pulse. A thin carbon foil of 50 Å thickness was used for positronium formation by process of charge exchange. Positronium Annihilation Spectroscopy (PAS) was utilized to carry out studies on the activation energy of hydrogen at the interface of oxide and silicon substrate and the effect of irradiation on the oxides in $SiO_2/Si(100)$ sample. The activation energy of hydrogen at the interface of $SiO_2/Si(100)$ samples with n$-$ and p$-$type substrate was measured to be 2.60(6) eV and 2.47(6) eV respectively. The investigations of the samples irradiated with x$-$ray and $\gamma-$ray led to the first time identification of creation of E' centers with PAS.

Acknowledgements

I am grateful for the opportunity to carry out research at Brookhaven National Laboratory (BNL). I am also thankful to all the members of Particles Solid Interaction (P.S.I.) group for their extensive support and invaluable help during my stay at BNL. I owe my deep gratitude to Prof. Leonard O. Roellig, Dr. K. G. Lynn, Dr. A. P. Mills, Jr., and Prof. K. F. Canter for their continuous support, insightful guidance, interest in my general welfare, and scientific career. Prof. Leonard O. Roellig as my thesis advisor took great pain in making sure that I had all the opportunities possible to mature into a good experimental scientist. He also constantly provided sound advice and encouragement during all the stages of my research career. Besides this, I am also greatly indebted to him for his continuous interest in my welfare beyond the research activities. During my stay at BNL, Dr. Kelvin Lynn provided all the necessary support for the research carried out for this thesis. His enthusiasm, hard work, and his innovative approach to research had been a constant inspiration to me. I am also thankful for his willingness to go out of his way to help during needs. I am grateful to Dr. Allen Mills for exposing me to different aspects of research over the years. I would like to express my thanks to Dr. Allen Mills and his wife Vicki for their generosity and hospitality during my trips to AT&T Bell Labs. I am thankful to Prof. Karl Canter for his patience, constant guidance, inspiration, and his help throughout the period of this research. Members of the positronium group Dr. Shengzhang Tang, Dr. Marc Weber, and Dr. Art Viescas are thanked for their support and help throughout my association with the group. Also Dr. P. Asoka–Kumar and Dr. Bent Nielsen deserves

my special thanks for their friendship, assistance and continuous encouragement throughout my association with them. I am also thankful to Lie Ping Chan for her sense of humor, friendship, and support throughout the time. I also appreciate very much the help and constant encouragement of Don Becker during my stay at BNL. The special thanks are also extended to Mike Carroll, Harry Hecker, Don Horne, and Mike Taylor for their continuous help and friendship over the years. I am also grateful to J. J. Hurst for his helpful advice on various matters. I am thankful to Mrs. Eileen Morello for her friendship and great concerns for my welfare during my stay at BNL. Mrs. M. McKeown is thanked for her help on various computer related problems. Last but not least I would like to thank all the members, visitors, scientific and technical staff, and fellow students of the PSI group at BNL for their help, support, friendship, tolerance, and sense of humor throughout my interaction with them. I am greatly indebted to Ariane and Ashu for their constant encouragement and deep concerns for my welfare. I would also like to thank Ariane for performing the excellent and professional German to English translation of a German language thesis. Davender Malik is also thanked for his constant encouragement, concerns, and friendship over the years.

Finally I would like to express my deep gratitude to my parents for their sacrifice, continuous encouragement, support and guidance throughout my life. I am also grateful to my wife for her great understanding and constant encouragement.

Table of Contents

Chapter 4:

Chapter 5:

Chapter 6:

List of Figures

Chapter 1.

INTRODUCTION

Since the discovery of the positron and later the positronium atom, a bound state of an electron and a positron, there has been a great effort in investigating the potential of the positrons and the positronium atoms to provide more insight in the bulk and surface properties of the solids. The existence of the positron, an antiparticle of the electron with the same mass and spin but opposite charge and the magnetic moment, was predicted by the Dirac in 1930 [1]. It was later identified by Anderson [2-4] in 1932 in tracks of the cosmic rays, in an experiment using cloud chamber.

In 1934, Mohorovičić [5] postulated the possible existence of the positronium atom (Ps), the lightest hydrogenic system. Later Deutch [6-7] demonstrated the existence of this positronium atom, produced in an experiment involving the interaction of positrons with gases. He was able to measure the decay rate of the triplet positronium from these experiments. All these developments opened a new era for the researchers in atomic and solid state physics. The experiments of DeBenedetti and others[8] measuring the anti-collinearity of the annihilating γ-rays indicated that γ-rays emitted due to the positron/s annihilation with electrons are not exactly anticollinear. The angle between these two back to back γ-rays is dependent on the momentum of the electrons in the solids. Positrons are intrinsically stable unless they interact with matter. Their life time is closely related to the local electron density. In the earlier years, the efforts were mainly concentrated on lifetime measurements, angular correlation, and energy analysis of the annihilating $\gamma-$rays. These efforts led to a vast amount of information on the concentration, characteristics of the defects and the electronic structure of different kind of materials. The detailed account on these efforts is well documented in the review by Stewart and Roellig [9]. In order to extract the information mentioned above, the positrons from a radioactive source were made to implant deep inside the solids and then thermalized before annihilating with electrons in the solids. These studies had no control over the energy of the positrons implanted into the solids. This handicap on the control over the energy of the incident positrons imposed many constraints on the potential applications of the positrons.

It was Madanski and Rasetti[10] who realised that the continuous distribution in energy of the positrons emitted from the radioactive sources were a hindrance to the full exploitation of the positrons as a useful probe. This motivated an effort to moderate the positrons from a ^{64}Cu radioactive source but failed, and they were unable to obtain slow positrons. They speculated that their failure to obtain slow positrons could be because of the surface condition of the moderator, and suspected that the positrons were getting trapped in the solid or at the surface and possibly lost through other channels such as positronium formation. Later others were able to verify these speculations.

It was Cherry[11] in 1958 who finally succeed in producing a moderated positron beam with a chromium- plated mica as a moderator. The efficiency for this moderator was quite low ($\sim 3 \times 10^{-8}$), where efficiency is defined as the ratio of the slow positron yield to the total number of fast positrons emitted by the radioactive source. The major breakthrough in achieving reasonable efficiency for positrons moderation however came when Canter *et al.*[12] discovered ***smoked*** MgO as a moderator. They were able to get an efficiency of 3×10^{-5}, which was two orders of magnitude higher than any other moderator at the time.

Further studies investigating the interaction of positrons with the solids suggested that understanding interactions of positrons with solid surfaces is one of the critical parameter for obtaining better moderators. This insight led to the realization of the great care needed for surface preparation in order to obtain better moderators. The search for even better moderators in late seventies was carried out with well prepared and atomically clean surfaces in ultra high vacuum (UHV) environment. All this progress with understanding of moderators opened a new frontier for the application of slow positron beams to solid state surface physics experiments, and was subsequently able to provide explanation of many new exotic phenomena. This also made it possible to control the positrons penetration depth easily as compared to the handicap faced in the earlier experiments. A detailed account of the history of the development of low energy positron beams and their consequences in the solid–state physics applications can be found in more details in the review article by Schultz and Lynn [13] and Fermi school lecture notes edited by Brandt and Dupasquier [14].

By 1978, the majority of experiments were performed in UHV environment on atomically clean surfaces, and it was demonstrated that positrons implanted into a clean single crystal target can diffuse back to the surface and then can either be emitted as free positrons or as positronium atoms. Further the progress made in the understanding of positronium formation processes from solid surfaces, thin films and in gases, with the use of monoenergetic positron beams, suggested the possibility of exploring the positronium beam [15] also as a potential probe to study the surface of solids. A review of the fundamental properties of positronium can be found in excellent reviews by Berko and Pendelton[16] and Rich [17]. The positronium atom, as a neutral weakly bound light particle, has many appealing characteristics which could make it suitable for use in studies on surfaces of the solids. Its mass, about three order of magnitude less than any common neutral atom, makes it much more energetic for the same deBroglie wavelength as compared with other neutral atoms such as helium and argon. Also, as a neutral atom, its long range interaction with electrons or ion cores is expected to be weaker than the Coulomb interaction as for electrons, positrons, and the ions. The binding energy of positronium is 6.8 eV in the vacuum, and, therefore, makes it very susceptible to be ionized during the collision with electrons, ion cores, and atoms provided their kinetic energy is greater than the positronium binding energy.

The development of a high intensity monoenergetic positron beam at Brookhaven National Laboratory and other places led to an effort to study various energetic positronium formation processes. A variable energy positronium beam was constructed at Brookhaven National Laboratory in 1987 [18] and used to carry out investigations on positronium reflections and scattering from the crystal (100) surface of cleaved LiF [19] and cleaned Cu(100) surfaces [20].

The other most highly active research area for positrons has been the study of various types and concentrations of defects in crystalline solids [21]. These variable energy positron beams provide the new understanding on surfaces, thin films, multilayer structures, their interfaces, and the buried layers in semiconductors. The high sensitivity of positrons to defects [13] was first demonstrated by MacKenzie [22] in 1967 and since the development of variable energy positrons beams, it has readily become a powerful tool in defect profiling.

The availability of variable energy positron beams also made possible a better understanding of the interaction of positrons with surfaces utilizing techniques such as two dimensional angular correlation of annihilation radiation (2D ACAR), time of flight (TOF) measurements, low energy positron diffraction (LEPD), positronium emission measurements from surfaces , and positron Auger electron spectroscopy (PAES). More details on these techniques can be found in the excellent review by Schultz and Lynn [13] and comparisons of various surface studies using positrons with other available surface science techniques using electrons, ions, photons, X-rays, and neutral atoms etc. can be found in Tang's thesis [20] and references therein.

This thesis describes work performed on rare gas solid positron moderators, a state of the art positron beam for a time pulsed positronium beam, with the capability of storing and bunching positrons, study of defects at the semiconductor interfaces, and creation of defects due to irradiation in oxides of Si(100) using Positrons Annihilation Spectroscopy (PAS). Chapter 2 contains discussion on the processes involved in moderating positrons from a continuous distribution of β^+ particles emitted from a radioactive source. The neon moderator performance will be discussed in more detail. Chapter 3 outlines the properties of the positronium atom and the different processes involved in the formation of positronium atoms. Further discussion on the challenges involved in making a positronium beam will be provided in chapter 4. This chapter also has a detailed discussion of the time pulsed positronium beam, with relevant technical details and the present status of this project. This chapter also includes details of the storage of positrons in the magnetic bottle, positron bunching, and their subsequent use in the formation of a positronium beam with the process of charge exchange using thin carbon foils. The next chapter will discuss the use of PAS in studies of the technologically important SiO_2/Si system. Results on measurements of the activation energy of hydrogen from $SiO_2/Si(100)$ interfaces and a study of creation of defects in oxides of the irradiated $SiO_2/Si(100)$ system will be presented. Mostly the effect of X−ray and $\gamma-$ray irradiation on these systems will be investigated. Finally the last chapter contains conclusions and a brief outline of the future directions with this state of the art time pulsed positron beam and the potential of PAS for interface and defect studies on SiO_2/Si systems.

Chapter 2.

Positron Moderators and Beams

1. Overview

One of the biggest obstacle to the usefulness of positrons in solid state physics was the absence of variable energy positrons beams. It took almost thirty years to achieve reasonable efficiency of the moderation of high energy positrons for it to be of any use. Therefore, over the years a great effort has been invested continuously in search for better moderators. This chapter will first discuss different kinds of source and moderator geometries in use for maximizing the efficiency. The main emphasis will be placed on only two important kind of moderators namely thin foil transmission and rare gas solid moderators. Once the processes for obtaining low energy monoenergetic positrons are explained, the next section will discuss rare gas moderators in detail and measurements on the neon moderator carried out at Brookhaven National Laboratory will be discussed.

2. *Positron Sources*

There are two kinds of positron emission processes, namely radioactive β^+ decay and pair production, which are commonly utilized to generate low energy positrons for research needs. The utilization of radioactive β^+ decay process usually involves the use of radioactive materials such as ^{22}Na, ^{58}Co, and ^{64}Cu. On the other hand the utilization of the pair production is usually achieved with the bremsstrahlung of the high energy ($\gg 2m_ec^2$) electron beam, generated by a LINAC, hitting a target of high Z materials (e.g. a tungsten crystal).

The most widely used positron sources are radioactive nuclei such as ^{58}Co and ^{22}Na which have a reasonably long life times (half life of 71 days and 2.6 years for ^{58}Co and ^{22}Na respectively). ^{64}Cu is not so widely used due to its fairly short half life (only 12.8 hours), however it has been used occasionally in some experiments such as High Flux Beam Reactor (HFBR) based beam lines, described in detail in the dissertation of Weber [23] and Tang [20]. A positron beam which uses traditional radioactive isotopes as a source, does not need to be located in close proximity to big facilities and, therefore, can be constructed independently. But their intensities are limited by the availability of high activity commercial isotopes, and are also restricted due to the safety hazard involved in source installations. A LINAC based positron beam has the capabilities to deliver both high intensity and pulsed positron beams. Therefore, several LINAC based high intensity pulse positron beams have been built and are used for carrying out various positron research [24-25].

Another approach to increase the positron beam intensity is to produce high activity β^+ isotopes with the use of a cyclotron or a nuclear reactor. Some efforts to produce high purity ^{22}Na with a 18 MeV cyclotron were reported by Saam and others [26]. At Brookhaven National Laboratory (BNL), high activity ^{64}Cu was successfully produced by irradiating ^{63}Cu in the HFBR at BNL and was used as the positron source for the high intensity positron beam. The thermal neutron capture process $^{63}\text{Cu}\ (n_{th}, \gamma)\ ^{64}\text{Cu}$ (where n_{th} represents the thermal neutrons) was utilized in this production. The typical decay scheme [27] for a radioactive source e.g. ^{22}Na is shown in the Fig. 2.2.1 below.

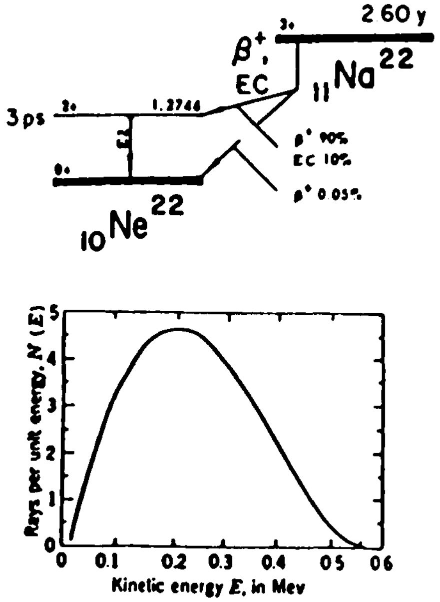

Figure 2.2.1 The decay scheme of ^{22}Na radioactive source together with the energy spectrum of the emitted β^+.

3. Positron Moderators

Positrons generated in a radioactive β^+ decay process or a pair production process are emitted over a very broad spectrum of energy. Monoenergetic positrons are utilized to study a wide range of interactions with solids. The need for monoenergetic positrons, and the desire for high flux, has led to a continuous effort to develop more and more efficient processes to moderate fast positrons emitted from a radioactive source.

The most commonly used approach to moderate fast positrons is to slow down these fast positrons in a crystal via excitations and other inelastic scattering processes. Most of the incident fast positrons are thermalized very quickly within $\sim 10^{-12}$ seconds. After thermalization, some of these positrons can diffuse back to the surface of the solid if the diffusion length of positrons in that solid is long enough and the implantation depth of the positrons into the solid is not so deep. The work function of the positrons ϕ_+, is negative for some solids and because of this, some of the thermalized positrons diffuse to the surface and are emitted from the surface with a maximum energy equal to the negative value of the work function. An illustration of the fate of the implanted positrons is shown in Fig. 2.3.1.

The efficiency of a moderator is usually defined as the ratio of thermalized positrons reemitted from the moderator to the total number of positrons emitted by the radioactive source. The characteristics of the moderated positrons and quantitative estimate of the efficiency of the moderator is dependent upon parameters such as the positron's implantation profile in the

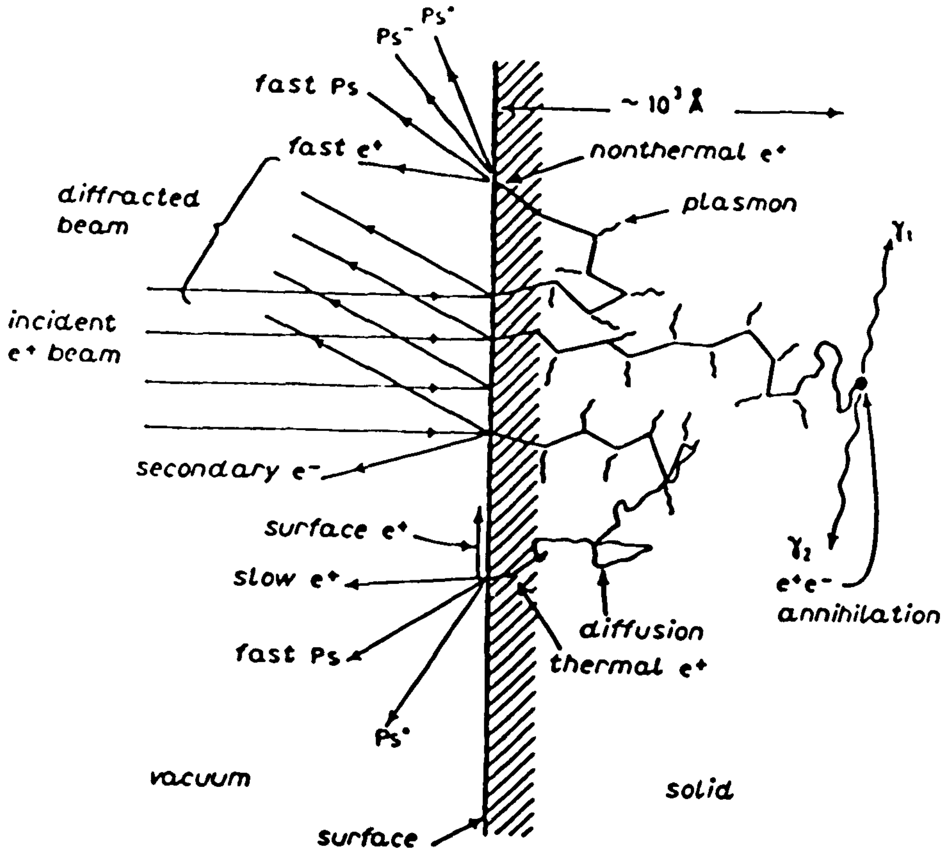

Figure 2.3.1 Outline of the possible interactions of the implanted positrons in the solids.(from ref. 14)

moderator, diffusion length in the moderator, work function of the moderator surface, and the positron reemission coefficient (which is defined as the ratio of the number of reemitted positrons to the total number of positrons diffusing back to the surface).

As mentioned earlier, when a positron enters a solid, it quickly slows down by losing its energy through processes such as inelastic scattering with electrons in the solid. The implantation probability for positrons is defined as the probability per unit distance for a β^+ being thermalized at a distance z from the surface of implantation, and can be expressed [28-30] as,

$$P_{im}(z) = \alpha e^{-\alpha z} \qquad (2.3.1)$$

where α is the attenuation coefficient of the moderator for the β^+ spectrum. The attenuation coefficient is empirically related to the density of the moderator, ρ, the end point energy, E_{max}, of the β^+ spectrum and an empirical constant A as,

$$\alpha = A\rho E_{max}^{-1.14} \qquad (2.3.2)$$

After thermalization, these fast positrons will diffuse around in the solid freely for a diffusion lifetime τ (typically about 10^{-10} sec) before they annihilate with electrons in the solid. Some of them may diffuse back to the surface, if the surface is within a diffusion length L_+. The probability P_d,of a positron at depth z' diffusing to the surface can be expressed as a function of the diffusion length L_+ as,

$$P_d(z') = e^{\frac{-z'}{L_+}} \qquad (2.3.3)$$

where $L_+ = \sqrt{D_{e^+}\tau}$ is the positron diffusion length and D_{e^+} is the diffusion coefficient of the positrons in the moderator.

The thermalized positrons which are able to diffuse back to the surface depend for reemission on several factors such as the surface electronic structure, the work function of the surface for positrons, and surface conditions such as the density of defects, and impurities at the surface. The electron work function ϕ_-, is defined as the minimum energy required for an electron to escape from the surface to infinity. This includes contributions both from the bulk, the electron's chemical potential μ_-, and the surface, the surface dipole barrier, D. The positron work function ϕ_+, is defined in exactly the same way as that for an electron, except the electron's chemical potential μ_-, is replaced by the positron's chemical potential μ_+, which includes the repulsion part from the ion cores and the attractive part from the electrons in the crystal, and the contribution of the surface dipole barrier D is reversed to negative instead of positive. Therefore work functions for electrons and positrons can be expressed as,

$$\begin{aligned} \phi_- &= +D - \mu_- \\ \phi_+ &= -D - \mu_+ \end{aligned} \tag{2.3.4}$$

The work function is typically a few eV for most crystal faces. The reversal of the surface barrier term in Eq. (2.3.4) makes the positron's work function very small and even negative for some crystal faces. For surfaces with negative positron work function, there will be a fraction of the thermalized positrons diffusing back to the surface which can be emitted to the vacuum with an energy equal to the negative value of the work function ϕ_+. Fig. 2.3.2 illustrates the potential experienced by a positron near a surface with a negative work function.

Only some of the thermalized positrons that reach the surface will be reemitted into the vacuum. As shown in Fig. 2.3.2, there is a small potential well just outside the surface due to the image potential which can trap some of the thermalized positrons that are trying to escape to the vacuum. Also, a fraction of these positrons can pick up electrons near or at the surface

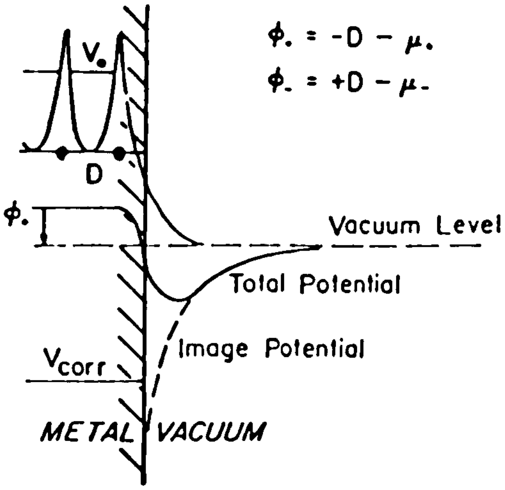

Figure 2.3.2 The single-particle potential for a thermalized positron at the surface region with a negative positron work function. The positron chemical potential includes the attractive correlation potential V_{corr}(from the conduction electrons in the crystal) and the repulsive zero-point potential V_0, from the ion cores. (from ref. 13)

and form positronium atoms, which are then emitted into the vacuum. The probability of these thermal positrons being emitted into vacuum once they reach the surface, P_{em}, depends upon parameters such as the material, the orientation of the crystal surface, and the surface conditions.

The longitudinal energy spread of the positrons reemitted from the clean crystal moderator surfaces is usually about 75 meV at room temperature [31-32], which is believed to be because of the thermal broadening due to the Maxwell-Boltzmann distribution of the positrons, and the angular spread of the reemitted positrons is on the order of $\sqrt{\frac{k_BT}{\phi_+}}$. Various positron source and moderator geometries have been used in the past in order to

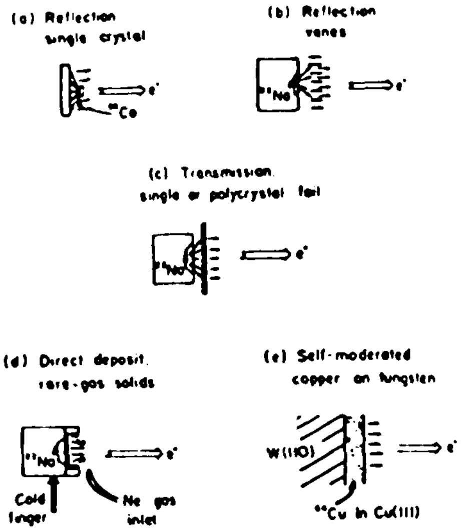

Figure 2.3.3 Schematics of some of the most commonly employed positron source and moderator geometries. (from ref. 13)

achieve the maximum combined efficiency. Fig. 2.3.3 shows a few source and moderator geometry combinations that are commonly employed.

It is not very easy to calculate accurately the efficiency of various type of moderators because of the contribution of additional factors such as self absorption in the source, variations in the geometry, surface conditions such as roughness and impurities, and differences in the extraction field together with the ones described earlier. The probability for the thermalized positrons to be emitted once they reache the surface is denoted as P_{em}, and then the final probability ϵ, of a thermalized positron diffusing back to the surface and being emitted after having been implanted at a distance z' is calculated by integrating $P_{em} \times P_d(z') \times P_{im}(z')$ over all z' and given as[30],

$$\begin{aligned}
\epsilon &= P_{em}\alpha \int_0^{\infty} e^{[-(\alpha+1/L_+)z'} dz' \\
&= \frac{P_{em}\alpha L_+}{(1+\alpha L_+)} \qquad\qquad (2.3.5)\\
&\simeq P_{em}\alpha L_+ \\
&\simeq \frac{(AP_{em}\rho\sqrt{D\tau})}{E_{max}^{1.14}}
\end{aligned}$$

In the final approximation above, the diffusion length L_+, is assumed to be much less than the mean implantation depth, which is valid for most metals and other high density materials. Eq. (2.3.5) gives an expression for calculating the efficiency of the moderator.

Also from Eq. (2.3.5), it is observed that the qualities desirable for a good moderator are a low end point energy of the β^+ decay, a long diffusion length in the moderator, a high density ρ, of the moderator, and a high emitting probability P_{em} at the surface. A majority of the positron moderators used are high density single crystals or polycrystals. These crystals usually have extremely low impurities and are annealed to ensure that the crystals have a large degree of crystal ordering and very low density of defects. This reduces the probability for positrons being getting trapped at impurity sites or defect sites. The thickness of the foil is usually selected to be on the order of the positron diffusion length L_+ in the crystal, as only those positrons that thermalize in the bulk within a distance of few diffusion length L_+, can diffuse back to the surface. In practice, very good quality W or Ni thin foils of thickness a few thousand to tens of thousands of Å are used. The thinner foils seems to provide higher efficiency of positron moderation, which is consistent with the above conclusions as L_+ is on the order of 1000 Å or less for most of the moderators usually used.

4. Rare Gas Solid Moderators

There has been many studies on the interactions of positrons in ionic crystals [13]. Measurements on the positron reemission by the ionic solids had indicated that when positrons were implanted into an ionic solid at keV energies, there was reemission of positrons with a spread of kinetic energies comparable with the band gap energy of the solids [33]. This suggested that solidified rare gases could be efficient emitters of low energy positrons. In the case of insulators, positron emission is not due to the surface having a negative work function ϕ_+, but is due to the fact that many of the positrons which return back to the surface are not thermalized and thus are able to overcome the surface barrier. It is a well known fact that in gas phase, rare gases are not very efficient in thermalizing positrons [34] and also that when solidified the energy loss processes are not that efficient at low energies. Among rare gas solid moderators, solid neon is by far the most efficient positron moderator known [35].

The energy loss mechanism for implanted positrons in rare gas solids is different than the energy loss processes for other moderators as discussed in the previous section. When fast positrons from a radioactive source are implanted in a rare gas solid, they will lose most of their initial energy through various scattering and excitation processes. However, there is a threshold of energy E_{th}, for inelastic scattering, below which positrons can lose their energy only through the process of phonon scattering. Therefore a very large fraction of the fast positrons implanted in the rare gas solids such as solid Ne would quickly be slowed down to the energy $E_{th} \sim 16$ eV, then diffuse in the solid neon for relatively long time before losing significantly more energy. Some of these positrons will be able to diffuse back to the surface, and overcome the surface barrier to make their escape to the vacuum. Because of the residual kinetic energy of these positrons and the inefficiency of the positron's phonon emission energy loss process in the solid neon at T $\sim$ 5 K, these positrons have very long effective diffusion lengths. Therefore, a relative large number of the positrons implanted in the solid neon will diffuse back to the surface and be reemitted into the vacuum again, resulting in a higher moderator efficiency. This energy loss mechanism is also responsible for the broader energy spread of these reemitted low energy positrons in comparison with other moderation processes.

All the advantages of attaining high efficiency for rare gas solids for positrons motivated us to undertake this project, and a neon moderator was investigated at a beam line at Brookhaven National Laboratory with a 350 μCi ^{22}Na sealed source, deposited on a 5 μm Cu/Be (made up of 98 % Cu and 2 % Be) window [36]. A schematics of the experimental set up is shown in Fig. 2.4.1.

The ^{22}Na radioactive positron source used for these studies was in thermal contact and kept electrically isolated from the cooling system. It was mounted at the source chamber end of the magnetically guided beam.

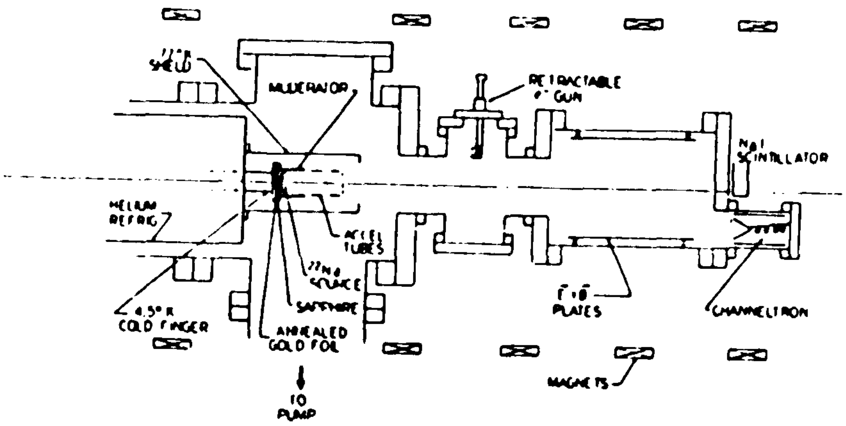

Figure 2.4.1 The schematics of the neon moderator and a magnetically guided positron beam with a ^{22}Na radioactive source. An $\vec{E} \times \vec{B}$ energy filter was utilized for selecting the energy of the moderated positrons.

A sapphire plate with an annealed gold gasket was used in order to provide both very good thermal contact and electrical isolation from the third stage of the cooling system. A closed cycle helium refrigerator was used to cool the source and the moderator assembly down to $\sim 5-7$ K. The axial magnetic field ($\sim$ 100 gauss) was utilized to transport the moderated positrons from the source to the detector end. The beam line was maintained in the ultra high vacuum (UHV) environment, with a typical pressure in the range of $\sim 2 \times 10^{-9}$ Torr. The vapor pressure of neon at 7 K is $\sim 10^{-9}$ Torr. In order to avoid contamination of the rare gases and hence of the moderator, the gas injection line was made UHV compatible and was maintained in the same pressure range as the beam line. Neon gas (as well as other rare gases) was deposited at the source/moderator assembly and the moderated positrons were extracted from the moderator using a combination of accelerating tubes and a grid assembly ($\sim$ 90 % transmission). The moderated positrons were extracted with an electric field of E $\approx$ 100 V/cm and transported at an energy of 100 eV. An $\vec{E} \times \vec{B}$ energy filter was used to filter out high energy positrons from the low energy moderated positrons. The transport of the positrons in the beam line was optimized by adjusting the magnetic field and the $\vec{E} \times \vec{B}$ filter. Slow positrons were counted using a channel electron multiplier (CEM) and a 3 in. × 3 in. NaI(Tl) scintillator detector in coincidence. The ratios of coincidences and the single counting rates of CEM and NaI(Tl) were used to measure the detector efficiencies and thus the absolute slow positron counting rate. Background contribution from the coincidence and the single rates was removed by taking the difference between the counting rates with the beam on and off.

As it is very easy to fabricate solid rare gas solids in unusual geometries (e.g. perforated plane, cylindrical, conical, parabolic, venetian blind, cylindrical rings, etc.), a number of different geometries were investigated. These geometries were: a number of cylindrical moderators in backscattering geometry with different aspect ratios (defined as the ratio of the length to the diameter), a combination of cylindrical geometry with a venetian blind of annealed polycrystalline Cu foils of thickness $\sim 7\mu$m, and a truncated conical configuration moderator made of oxygen – free high conductivity (OFHC) copper. Here OFHC copper was used especially for its good thermal conductivity and its future use with a ^{64}Cu radioactive source at Brookhaven National Laboratory. However, this can be substituted with any other material with high atomic number, Z, and good thermal conductivity (e.g. Au, Pt, etc.). The cross section of the moderator together with its geometries is shown in Fig. 2.4.2.

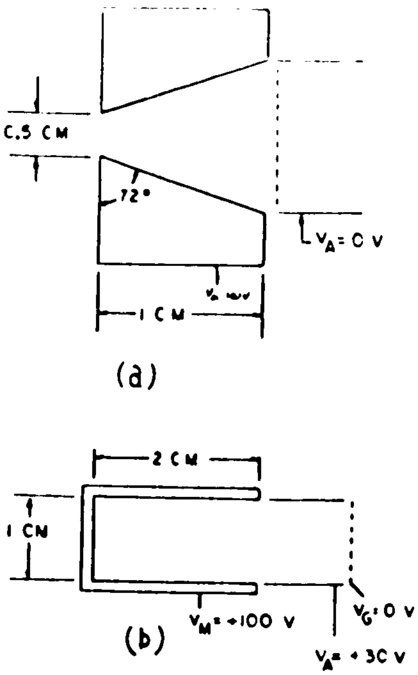

Figure 2.4.2 Schematics of the cross sectional view of conical and cylindrical moderator geometries used for rare gas deposition.

The thickness of the solid neon is one of the parameters that influences the efficiency of the neon moderator, as shown in Fig. 2.4.3. The measurements for a cylindrical surface with an aspect ratio of 2 indicated that the

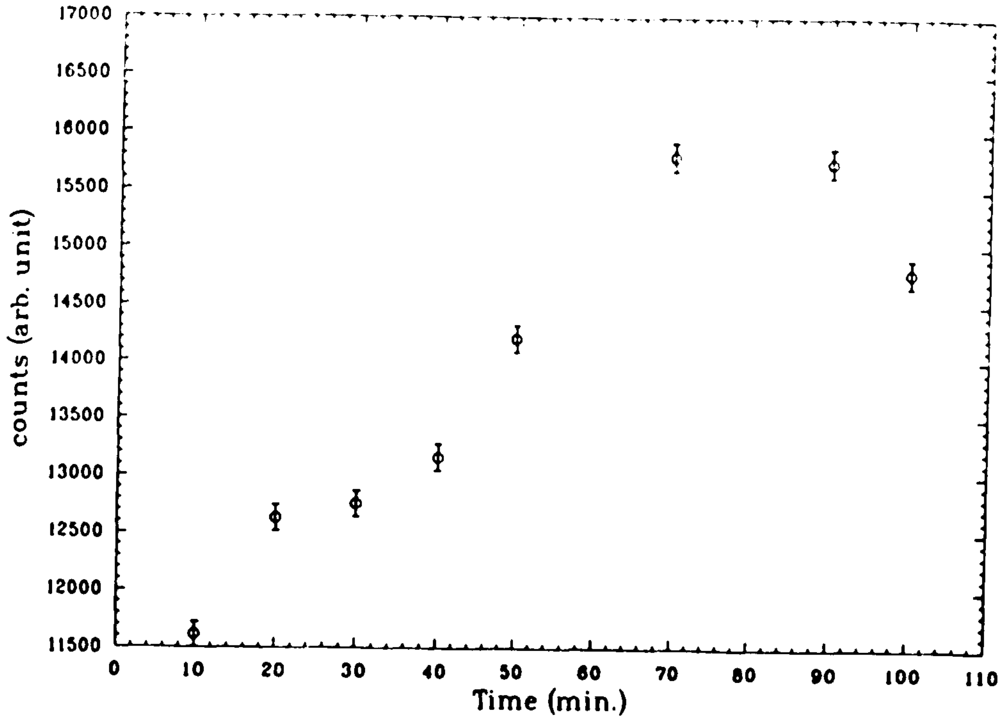

Figure 2.4.3 Slow moderated positron counts vs time neon was deposited onto ^{22} Na at 3.2 × 10^{-4} Torr.

efficiency for moderation increases as a function of the thickness of the solid neon and was observed to rise steadily to a maximum value, in agreement with the earlier observations [35]. To attain this, high purity neon gas was injected into the vacuum system at a pressure of 3.2 ×10^{-4} Torr for about ≈ 80 min.

The conical OFHC copper cup efficiency with neon was measured to be (4.6 ± 0.1) × 10^{-3}, while for cylindrical cup [35] with an aspect ratio of 2 was (1.7 ± 0.1) × 10^{-3}. It should be stressed here that these quoted efficiencies were measured for a cylindrical moderator with a sealed ^{22}Na source as compared to the efficiency $\sim 7 \times 10^{-3}$ for a bare ^{22}Na source coated with a thin layer of Krylon. Comparison indicated that the conical moderator performed better by a factor of (2.7 ± 0.2) than the cylindrical moderator. One of the reasons for this improved performance for the conical moderator might be that slow positrons were extracted more efficiently in this particular geometrical configuration [37]. It was also observed that other rare gas solids (e.g. Ar, Xe, Kr) at the same low temperatures were $\sim \frac{1}{6}$ as efficient as solid neon in the cylindrical configuration moderator with the same aspect ratio, in agreement with previous observations [35]. There was no enhancement observed in the efficiency of the neon moderator when a venetian blind configuration was inserted into the cylindrical moderator. One of the reason might have been that not enough layers of neon were deposited on the surface of the foils.

One of the other motivations for this project was to further investigate the feasibility of the neon moderator for use with an intense ^{64}Cu radioactive source to obtain a high flux beam of moderated positrons. The use of ^{64}Cu would involve vacuum depositing the ^{64}Cu on the conical/cylindrical surface and condensing neon gas (or other rare gases) on it to act as a moderator. Therefore, it is important to know the efficiency for a bare source such as ^{22}Na for these particular geometrical configuration. With conservative estimates, the efficiency of the encapsulated ^{22}Na source was underestimated to that for the bare ^{22}Na source by a factor of $\sim$ (3.1 ± 0.5). Thus the corrected efficiency for a neon moderator in the conical configuration with a bare ^{22}Na source will be $(1.4 \pm 0.2) \times 10^{-2}$. In conclusion this study has shown that for a bare source with a conical solid neon moderator, it should be possible to achieve efficiency as high as (1.4 ± 0.2) %. It is apparent that with improved field extraction techniques (e.g. concentric cylindrical rings connected together with a resistive chain), the cylindrical and other geometrical configurations can provide even better efficiency, although with a much larger energy spread Δ E. Using the conical configuration and a linear scaling to the HFBR generated ^{64}Cu source, it is estimated to be possible to obtain a moderated positron flux as high as 7.8×10^{9} e^{+}/sec [38].

Chapter 3.

Positronium Atom and Beams

1. *Overview*

The development of positron beams and the discovery of positronium atom led to an explosion of activities aimed at gaining more understanding of the positronium atom. The positronium atom, as the lightest leptonic system, offers a unique opportunity to carry out more investigations on the quantum electrodynamic aspects of a two body system. The realization of high flux positron beams led to an effort exploring the potential use of positronium beams as a useful tool for the study of surfaces. The group at Brookhaven National Laboratory has succeeded in observing the specular reflection of positronium atoms from the surface of a LiF crystal. The first section of this chapter outlines briefly the properties, annihilation characteristics, and the decay schemes of the positronium atom. It further discusses the energy level scheme of the positronium atom in analogy with the hydrogen atom. Finally it touches upon the impact of an electric field and the magnetic field on the energy levels of the positronium atoms. The next section looks into the different processes responsible for the production of the positronium atoms when positrons interacts with the solids and finally the production of energetic positronium beam. In the last part of this section, there is a brief discussion of the experimental results on the positronium beam obtained by utilization of different techniques.

2. Positronium Atom

Positronium is a bound system of an electron and its antiparticle, the positron. The positronium atom is very similar to the hydrogen atom except that the proton of the hydrogen atom is replaced by the positron. This system of a particle and antiparticle consists of two particles with the same mass, the same magnitude of the magnetic moment, and a combination of either parallel or anti–parallel alignment of the spins. Positronium provides an ideal ground to perform tests on the quantum electrodynamic hypothesis. It is a purely leptonic system which involves only weak electromagnetic interactions. In positronium atom, there is no strong force that complicates the calculations as in the case of the hydrogen atom.

Positronium Annihilation Selection Rules

Positronium bound state is quasi–stable as there is a finite probability for the wavefunctions of an electron and a positron to overlap and annihilate. The energy and momentum of this annihilating electron and positron pair is carried away by the emitted photons. The electron and positron pair can have orientation of their spins either parallel or antiparallel. The singlet state positronium (S = 0) is known as para–positronium while the triplet state positronium (S = 1) is known as ortho–positronium. The number of photons emitted during the annihilation are dependent upon parameters such as conservation of momentum, energy, total spin, and charge conjugation. The positronium does not annihilate via a single photon as both energy and momentum can not be conserved simultaneously (a photon can not have non vanishing energy without having non vanishing momentum in the center of mass frame of the positronium).

Charge conjugation is a operation under which it is possible to exchange the particles by their antiparticles without changing any physical property of a system such as momentum or spin. Charge conjugation is invariant during annihilation of the electron – positron pair. The charge conjugation operation in the positronium results in a factor of $(-1)^{l+s}$ in the wavefunction of the positronium. In this, a factor of $(-1)^{l}$ comes from the orbital wave function while a factor of $(-1)^{s+1}$ comes from the spin wavefunction, and another factor of (-1) from the fact that the electron and positron have opposite intrinsic parity. Also, charge conjugation contributes a factor of $(-1)^{n}$ to the wavefunction of an n–photon state due to a contribution of (-1) from each photon state [39, 16]. These selection rules for the positronium atom can be summarized as,

$$(-1)^{l+s} = (-1)^{n} \tag{3.2.1}$$

From this selection rule, it is evident that spin singlet states (s = 0, l = 0) annihilate to produce an even number of the photons, while spin triplet states (s = 1, l = 0) annihilate and produce an odd number of photons, except for single photon annihilation.

Conservation of energy and momentum for two photon annihilation process requires that the two photons be emitted in the opposite direction with the same energy of 511 keV in the center of mass frame of the electron – positron, pair whereas for the three photon annihilation, the conservation of the total momentum and energy allows the photons to be emitted over a continuous energy range, with a maximum energy of m_ec^2. The annihilation spectrum for three photon decay [40] is shown in the Fig. 3.2.1.

Positronium Decay Rate Scheme

The annihilation decay rates of positronium have been calculated using information about the electron – positron annihilation cross sections and the wave function of the positronium [41]. The cross section for the two photon annihilation in the nonrelativistic velocity limit ($v \ll c$) is given as [42],

$$\sigma_{2\gamma} = \frac{\pi r_0^2 c}{v} \qquad (3.2.2)$$

where r_0 is the classical radius of the electron, c is the velocity of light in vacuum, and v is the relative velocity of the electron – positron pair. The cross section for the three photon annihilation is much smaller as it is a higher order effect as compared to two photon annihilation. The ratio of the cross section between three photon and two photon annihilation, in the low velocity limit, is given as [41],

$$\frac{\sigma_{3\gamma}}{\sigma_{2\gamma}} = \frac{4(\pi^2 - 9)}{3\pi}\alpha \simeq \frac{1}{371.6} \qquad (3.2.3)$$

where α is the fine structure constant.

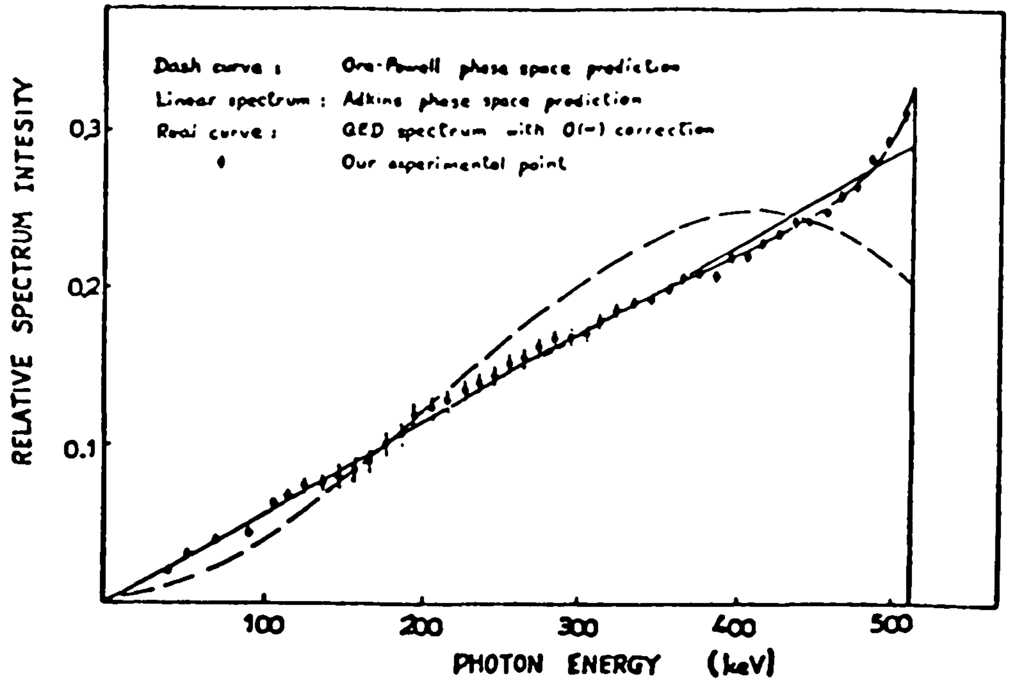

Figure 3.2.1 The experimental and theoretical energy spectrum of photons emitted in three photon decay of ortho–positronium. The dashed curve is from the Ore–Powell phase space predictions; the straight line spectrum represents the Adkiens phase space predictions, the solid curve is QED spectrum with $o(\alpha)$ correction; and open dots with error bars are experimental measurements. (from ref. 37)

From Eq. (3.2.3), it is evident that the cross section for three photon annihilation is smaller by a factor of approximately 3α compared to that for two photon annihilation. The cross section for four photon annihilation has been calculated to be a factor of 9×10^{-5} (i.e. of order α^2) less than that for two photon annihilation process [43]. Similarly, the cross section for n^{th} order even number photon annihilation is smaller by a factor of α^n as compared to two or three photon annihilation processes. From the cross section for the annihilation given by Eq. (3.2.2) and Eq. (3.2.3), and the wave function of the positronium, the life time of the para-positronium is [44-45],

$$\tau_1 = \frac{2}{\alpha^5}\frac{\hbar}{m_e c^2} \simeq 0.125 \quad \text{nsec} \tag{3.2.4}$$

whereas the life time of the ortho-positronium is given as [41],

$$\tau_3 = \frac{9\pi}{2(\pi^2 - 9)}\frac{1}{\alpha^6}\frac{\hbar}{m_e c^2} \simeq 141.8 \quad \text{nsec} \tag{3.2.5}$$

In the past, there has been a number of experimental efforts to measure the life time of the ground state of the positronium atom with high precision [16]. Measurements on the annihilation decay rates and the lifetimes for the excited states of the positronium has also been carried out [46].

The Fig. 3.2.2 shows the schematics of the decay rates for the ground and excited states of the positronium atom. The optical transition between different energy levels in a positronium atom follows selection rules similar to the hydrogen atom. These selection rules are,

$$\Delta s = 0, \ \Delta l = \pm 1, \quad \text{and} \quad \Delta j = 0, \pm 1 \tag{3.2.6}$$

where j = l + s. From Fig. 3.2.2 and Eq. (3.2.6), it is evident that 2P positronium can optically decay into the ground state. The probability for 2S → 1S decay is extremely low because of the selection rules in Eq. (3.2.6). This metastable state has a lifetime of 1.14 μsec and 1.0 nsec for triplet and

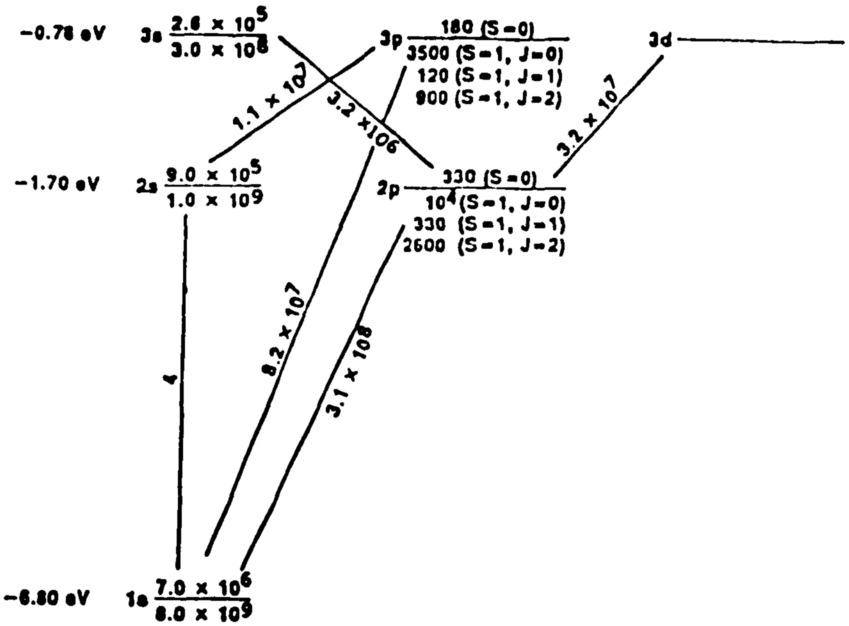

Figure 3.2.2 The rates of the positronium states for two and three photon annihilation and optical deexcitation. The units are in sec^{-1}. (from ref. 46)

singlet state respectively, much longer than the respective ground states. For excited states, a longer life time is also expected due to the decrease in the overlap of the electron and positron wave functions.

The optical decay rate for $2P \rightarrow 1S$ states of the positronium is higher than the annihilation decay rates. Therefore the majority of the 2P states optically decay via Lyman$-\alpha$ emission to the 1S state before they have the chance to annihilate in the excited 2P state. Once these state have optically decayed to the ground state 1S, then they decay through the channel of annihilation decay. The life time of different states can be determined by the annihilation decay rates. The lifetime of the triplet state 2S level is longer by a factor of 8 in comparison with the 1S state.

The short lifetime of para–positronium makes it extremely hard to utilize para–positronium atoms as a probe to study its interaction with solids. On the other hand, ortho–positronium atoms have a long enough lifetime for them to be exploited as a useful probe. The travel distance before decay is dependent upon the energy of the ortho–positronium atom and typically an ortho–positronium atom with energy of 1 eV can travel a distance of 6 cm in vacuum before it decays.

Positronium Energy Levels

Information on energy levels and annihilation rates of low lying states of the positronium atom are essential for carrying out studies on different aspects of quantum electrodynamics. The spectroscopic structure of positronium is similar to that of the hydrogen atom. For a hydrogen atom the reduced mass, μ_H, of the two body system is given as,

$$\mu_H = \frac{m_p m_e}{m_p + m_p} \simeq m_e \quad \text{as} \quad (m_p \gg m_e) \tag{3.2.7}$$

where m_p and m_e are the masses of a proton and an electron respectively. Similarly, the reduced mass for positronium can also be given as,

$$\mu_{Ps} = \frac{m_e m_{e^+}}{m_e + m_{e^+}} \simeq \frac{1}{2} m_e, \quad \text{as} \quad (m_e = m_{e^+}) \tag{3.2.8}$$

where m_{e^+} is the mass of the positron. In Eq. (3.2.8), this scaling of positronium mass will change the Schrödinger energy levels of hydrogen atom by a factor of $\frac{1}{2}$ and the energy levels for the positronium atom can be given as,

$$E_n(Ps) \simeq \frac{1}{2}E_n(H) = \frac{m_e c^2 \alpha^2}{4n^2} \tag{3.2.9}$$

where $\alpha = \frac{e^2}{\hbar c} \simeq \frac{1}{137}$ is the fine structure constant. From Eq. (3.2.9), the binding energy of the positronium atom is 6.8 eV, whereas the binding energy for the first excited state is 1.7 eV.

Similar to the hydrogen atom, each energy level E_n, of positronium atom is also further split into several sublevels. The reasons for this removal of degeneracy in energy levels for positronium atom is different than that for the hydrogen atom as the principal factors causing the removal of degeneracy are quite different. For hydrogen, the main contributing factor for degeneracy removal is the spin orbit (l−s) coupling. The interaction of the electron spin with the nuclear spin (s−I) coupling can be treated as a small perturbation as the magnetic moment of the nuclear spin is much smaller than the electron spin and the orbital angular momentum. This coupling gives the hyperfine structure splitting. However, for the positronium atom, the equality of the mass and the magnitude of the magnetic moment of the electron and positron makes the spin−spin (s−s) interaction a major contributor to the removal of the Coulomb degeneracy. Virtual electron−positron annihilation also contributes significantly to the removal of this degeneracy

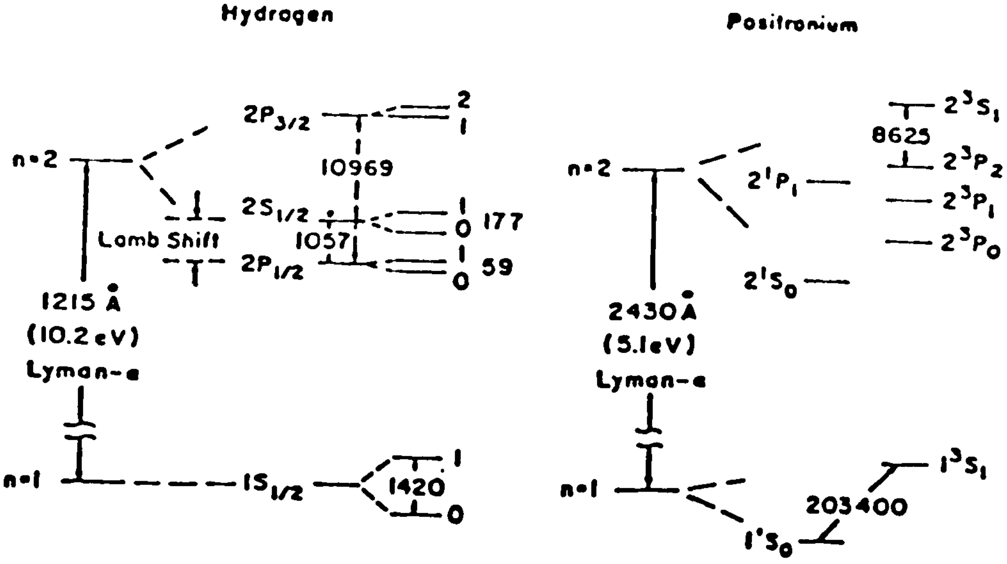

Figure 3.2.3 The schematical comparison of the n = 1 and n = 2 energy levels of the hydrogen and the positronium atom. The energy level differences are given in MHz. (from ref. 16)

as its contribution to the energy splitting is also on the same order as that from the spin–spin coupling [16].

Fig. 3.2.3 shows the energy level diagram for the positronium and hydrogen atom. Here the notations are defined similar to the spectroscopic notations in atomic physics as n $^{2s+1}L_j$ where j = l + s .

The fine structure splitting of the energy levels between the triplet and singlet states for the ground state, is given as, in the lowest order [16],

$$E(1^3S_1) - E(1^1S_0) = \Delta E_1 \tag{3.2.10}$$

where

$$\Delta E_1 = \frac{7}{3}\alpha^2 E_1(Ps) \tag{3.2.11}$$

In Eq. (3.2.11), the term $\frac{7}{3}$ includes a contribution of $\frac{4}{3}$ from spin–spin coupling and a factor of 1 from virtual annihilation processes. There have been calculations for the energy splitting with higher order corrections and to order α^6 terms are given as,

$$\Delta E_1 = \frac{\alpha^4 m_e c^2}{4}\left[\frac{7}{3} - \frac{\alpha}{\pi}\left(\frac{32}{9} + 2\ln 2\right) - \frac{5}{6}\alpha^2 \ln\alpha\right] \tag{3.2.12}$$

Similarly, the corresponding lowest order energy splitting between the triplet and singlet ΔE_2 for the excited state n = 2, is $\Delta E_2 = \frac{\Delta E_1}{8}$. Corrections to the n = 2 nonrelativistic energy levels to order α^4 and α^5, have also been calculated [46].

Positronium Atom in a Magnetic Field

The ground state (n = 1) of the positronium atom has no zero order Zeeman energy splitting, as the magnetic moments of the electron and the positron have exactly the same value but opposite sign. The positronium atom Hamiltonian in a static magnetic field B_0 is given as [46],

$$\begin{aligned}\mathcal{H} &= \mathcal{H}_t + \mu_0 g_1 s_1 . B_0 + \mu_0 g_2 s_2 . B_0 \\ &= \mathcal{H}_t + V\end{aligned} \tag{3.2.13}$$

where $\mathcal{H}_t$ is the unperturbed hamiltonian, μ_0 is the Bohr magneton ($= \frac{e\hbar}{2m_e c}$), g is the gyromagnetic ratio for the electron and positron with $-g_2 = g_1 = g$ and s_1 and s_2 are spin operators for the electron and positron respectively.

If B_0 is taken along the z-direction, the perturbation term V can be written as,

$$V = \frac{g_e \mu_0 B_0}{2}(\sigma_z{}^1 - \sigma_z{}^2) \tag{3.2.14}$$

where σ_z is the Pauli spin matrix. This leads to non-zero off-diagonal elements for the ground state,

$$\begin{aligned} \langle {}^1S_0, m = 0|V|{}^3S_1, m = 0\rangle &= \mu_0 g_e B_0 \langle {}^3S_1, m = 0|V|{}^1S_0, m = 0\rangle \\ &= \mu_0 g_e B_0 \end{aligned} \tag{3.2.15}$$

Energy levels for positronium atom under the magnetic field are,

$$\begin{aligned} E(1^3S_1, m = \pm 1) &= E(1^3S_1) \\ E(1^3S_1, m = 0) &= \frac{1}{2}[E(1^3S_1 + E(1^3S_0)] + \frac{1}{2}\Delta E_1\sqrt{1 + x^2} \\ E(1^1S_0, m = 0) &= \frac{1}{2}[E(1^3S_1) + E(1^3S_0)] - \frac{1}{2}\Delta E_1\sqrt{1 + x^2} \end{aligned} \tag{3.2.16}$$

where $x = \frac{2g_e\mu_0 B_0}{\Delta E_1}$ and ΔE_1 is as defined in Eq. (3.2.10).

It is evident from Eq. (3.2.16) that the magnetic field does not have an effect on the $m = \pm 1$ states. However, it causes mixing of the $m = 0$ triplet and singlet states. Fig. 3.2.4 shows the Zeeman splitting [16] of the n = 1 levels of the positronium atom.

The energy splitting between the $m = \pm 1$, and the m = 0 states for the ortho-positronium is,

$$\Delta E_{1,0}(1^3S_1) = \frac{1}{2}\Delta E_1(\sqrt{1 + x^2} - 1) \tag{3.2.17}$$

This is a small effect. The energy splitting is only about 0.7 % of ΔE_1 ($\sim 5.75 \mu eV$) for a magnetic field of 1 Tesla. This field is much higher than the fields typically employed for magnetic transport of the e^+ beams ($\sim$ 100 - 150

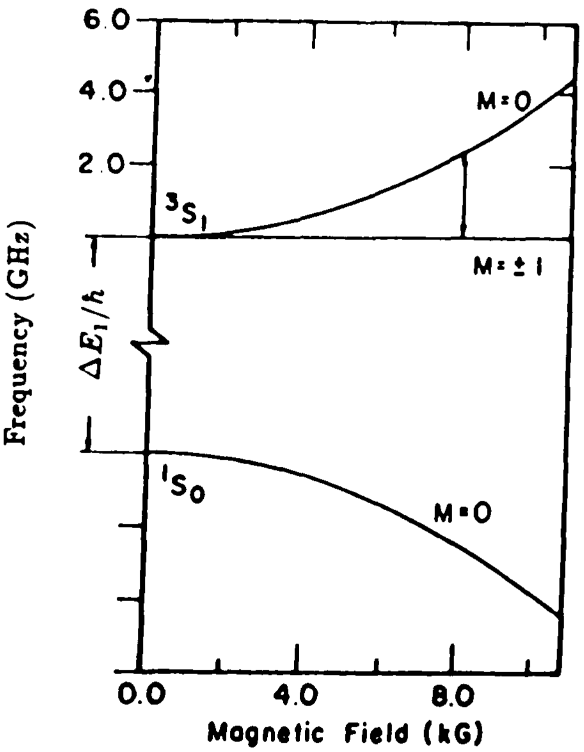

Figure 3.2.4 The Zeeman splitting of the n = 1 levels of the positronium atom. The frequency scale is in GHz. (from ref. 16)

gauss). This suggests that ortho-positronium is not effected under normal conditions. Recently it has been observed that ortho-positronium annihilation in magnetic field shows time oscillations in the angular distribution whose frequency is dependent upon the hyperfine splitting [48-49]. It has also been proposed that this phenomena can be utilized to investigate solids with the technique named as Positronium Spin Rotation (PsSR) [50].

Positronium Atom in an Electric Field

The Stark effect in the presence of an external electric field E does not affect the ground state energy levels of the positronium atom, as S state is the only orbital state in the ground state. However, it does generates state mixing between 2S and 2P states. The coupling matrix element $V_{2s,2p}$ is on the order of $6a_0e|E|$ where a_0 is the Bohr radius of the hydrogen atom. The state mixing is proportional to $V_{2s,2p}/\Delta E_{2s,2p}$, for the case where $V_{2s,2p}$ is small in comparison to $\Delta E_{2s,2p}$. Here $\Delta E_{2s,2p}$ is the energy difference between the 2S and 2P states.

The triplet 2 $^3S_1$ state has much longer lifetime than 2 $^3P_1$ state. The state mixing by Stark effect can cause the quenching of 2 $^3S_1$ states. Positronium atoms traveling in a magnetic field could be affected by a motional Stark effect due to an effective electric field, given as,

$$E_{eff} = \gamma\vec{\beta} \times \vec{B} \tag{3.2.18}$$

where $\vec{\beta} = \frac{\vec{v}}{c}$ and $\gamma = \frac{1}{\sqrt{1-\beta^2}}$. Here v is the velocity of the positronium atom, and B is the magnetic field. Only positronium atoms traveling perpendicular to the magnetic field are affected by this electric field [51].

The fine structure splitting of energy ΔE_1, for 1S state of the positronium atom was measured [52] for the first time in 1951, by measuring the small amount of mixing of the triplet and the singlet state in a uniform magnetic field. Since then, there have been many experiments carried out to measure the energy structure of positronium. Some of these efforts are the first observation of Lyman$-\alpha$ (2P → 1S) emission from positronium by Canter [53] *et al.*, the first observation and measurement of 2 $^3S_1 \rightarrow$ 2 $^3P_2$ energy splitting in the positronium atom by Mills [54] *et al.*, the observation of 1 $^3S_1 \rightarrow$ 2 $^3S_1$ transition in positronium atom with two photon excitation by

Chu and Mills[55], and finally the accurate measurement of the corresponding energy interval by Chu [56] *et al.*

3. Positronium Beam

The observation of positronium formation in gases has led to many other investigations on different positronium formation processes and study of other related interactions. In the past, energetic positronium was produced mainly in gases with positron gas interactions, but recently other positronium formation processes have shown a promise for the future, such as the interaction of positrons with thin foils to form energetic positronium. Thermal positronium production occurs when positrons are implanted into a solid surface, and has been used in many investigations on the fundamental properties of positronium. This section contains a brief account on the processes involved in positronium formation in solids and experimental results on energetic positronium production processes.

Processes for Positronium Formation in Solids

The physical processes that take place when positrons are implanted in the surface of a solid are shown in Fig. 2.3.1. One of them is the emission of thermal or energetic positronium from the surface. Several processes can contribute to the emission of positronium from the surface and the characteristics of the emitted positronium will reflect those emission processes.

When positrons are implanted in the solid, the majority of them will penetrate deep into the bulk and go through various energy loss processes, and are eventually thermalized. Some of these thermalized positrons can diffuse back to the surface if they happens to be thermalized within a distance of diffusion length L_+, away from the surface. These thermalized positrons, on their way back to the surface, may form positronium by picking up an electron at the surface and then are emitted from the surface with an energy $-\epsilon_{Ps}$, provided the potential outside the surface is negative and is given as,

$$\epsilon_{Ps} = \phi_+ + \phi_- - E_B^\infty \tag{3.3.1}$$

where ϕ_- and ϕ_+ are the work functions for the electron and positron respectively. The binding energy of positronium in vacuum is $E_B^\infty = 6.8$ eV. This large value of $E_B{}^\infty$ makes ϵ_{Ps} negative for many surfaces, which in turn makes it energetically more favorable for positron to be emitted from a solid as a positronium atom.

The other possibility for thermalized positrons diffusing back to the surface is to get trapped at the surface in the surface potential well. These trapped positrons can be thermally desorbed as positronium atoms at elevated temperatures and emitted into the vacuum. It has been also observed that in some insulators, positronium is formed in the bulk, with some of the bound electrons liberated during the energy loss of the implanted positrons. These positronium atoms diffuse out to the surface and then are emitted in the vacuum provided the work function for positronium [13,57], defined as

$$\phi_{Ps} = E_B - E_B^\infty - \mu_{Ps} \tag{3.3.2}$$

is negative. Here E_B is the positronium binding energy in the crystal and μ_{Ps} is the chemical potential of the positronium. Usually E_B is smaller than E_B^{∞}, therefore ϕ_{Ps} is negative for a number of crystals, e.g. LiF and NaF. All three processes discussed above involved positrons that were thermalized in the bulk. The positronium atoms produced in the above processes typically have energy ranging from thermal energy $\sim k_B$T to a few eV.

Another process that also leads to positronium formation involves non-thermal positrons. Although a large fraction of positrons are thermalized in the bulk, a small fraction will scatter back to the surface with relatively high energy, up to the incident energy. These positrons may pick up an electron at the surface to form a positronium atom, and may be then emitted into the vacuum with relatively high energy. The positronium produced in this process is usually emitted over a broad spectrum of energies. This energy spread results mainly from the energy spread of the energetic positrons. Since these positrons include positrons that have not been fully thermalized, their energies can range from the original incident energy for those scattered without energy loss, to a few eV for those which already have undergone various inelastic scattering and excitation processes.

The above mentioned positronium production process can be further enhanced in at least two different ways. One of them is to use a thin film. If the foil is sufficiently thin, some of the incident positrons would still be energetic enough when they approach the surface on the other side of the foil and some of these energetic positrons would pick up an electron at the surface to form positronium atom and leave the surface as an energetic positronium atom.

Another way to make positronium is to let positrons to strike the surface of a solid at a near glancing angle, so that a large fraction of the positrons can be scattered back towards the surface without penetrating deep inside the bulk and without too much energy loss. These backscattered energetic positrons have a good possibility to pick up an electron to form an energetic positronium atom on their way out and then be emitted into the vacuum. Another process which is also related to the positronium emission from the surface is the Ps^- emission. In this process, a positron can pick up two electrons instead of one at the surface and form a Ps^- ion. This emitted Ps^- can be accelerated after its emission and then stripped of its extra electron with a process of photodetachment [58] to give a positronium atom. The calculated binding energy of Ps^- against breakup into Ps and a free electron is 0.3266 eV and its expected 2γ annihilation decay rate [59] is $\Gamma \sim 2.09(9)\ \mathrm{nsec}^{-1}$.

Experimental Results on Positronium Production

The different processes for positronium formation described in the last section have been investigated and observed experimentally [13]. Energetic positronium production processes that involve non-thermal positrons and Ps^- production have promise for future application in the study of solid

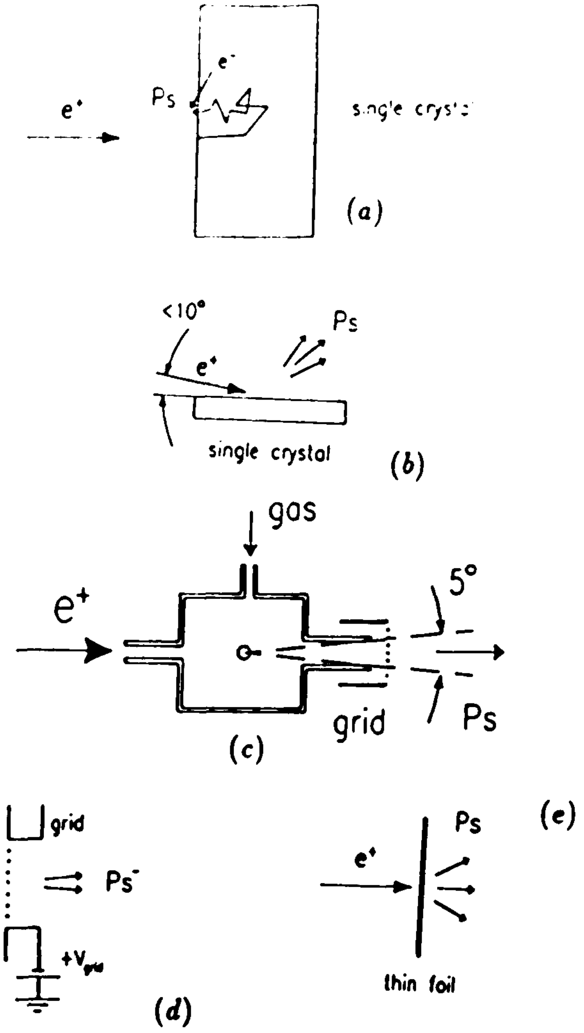

Figure 3.3.1 Schematics of different positronium production processes. (a) thermal and energetic positronium production from a single crystal surface; (b) emission of fast positronium by glancing angle incidence of low energy positrons on a single crystal surface of metal; (c) variable energy positronium production with a gas cell; (d) production of energetic Ps^- ions; (e) fast positronium production using a thin carbon foil. (from ref. 23)

surfaces. Fig. 3.3.1 shows some of the possible positronium production setups.

As shown in Fig. 3.3.1, positronium negative ions were observed by directing a 400 eV positron beam at a 40 Å carbon foil [60]. The efficiency for Ps^- was estimated to be $(2.28 \pm 0.3) \times 10^{-4}$. It is suggested theoretically that the Ps^- produced in this manner can be accelerated and then be neutralized (photodetachment) by a laser [58]. Energetic positronium of 10–500 eV, emitted from a 50 Å carbon foil, with a continuous energy spectrum approximately proportional to $E^{-3/2}$, when the foil was bombarded with a positron beam of a few keV, has also been observed [61]. The efficiency for positronium production was measured to be about 10^{-4} positronium per positron per eV per sec per steradian at 50 eV. This particular process of positronium formation is attempted in this thesis and described more in the next chapter.

An energetic 10–100 eV positronium production, with ~ 20° FWHM, by scattering a well collimated small diameter positron beam of 30–400 eV off single crystal of Al(100) and Cu(100) surfaces at glancing angle has also been reported [62]. A total efficiency of a few percent was reported, with no information on the energy distribution of the emitted positronium.

Monoenergetic positrons beams have also been used to carry out systematic studies of positronium formation in gases. In these experiments, positrons were thermalized in gas and formed positronium atoms by charge exchange with the gas atoms. The total positronium formation cross section for different gases has been measured [63]. There have been various theoretical calculations of both the total and differential cross sections for $n = 1$ and $n = 2$ states of positronium formation in H_2 and He gases [64-66]. Experimental details of positronium production in gases and their application to study of surface of solids are described in Weber's [23] and Tang's [20] dissertations.

The Ps^- production approach, with its possibility to be accelerated to any desirable energy and be energy filtered because of its charge, could be a useful way to make high energy monoenergetic positronium in the future. However, the short life time of Ps^- and presently, the lack of experience in photodetachment of Ps^-, makes it not so feasible presently. Positronium production with a thin carbon foil is a very practical approach to make positronium atoms with a range of energies. The positronium is produced in a UHV environment with this approach as compared to positronium production using the positron–gas interactions. This is a very important advantage for carrying out studies on surfaces. The handicap of this approach is a broad energy spectrum of the positronium atoms which requires an energy analysis using time of flight measurements. This has been incorporated in the state of the art beam line built at BNL for this thesis work and is discussed further in more details in the next chapter.

Chapter 4.

Bunched Positronium Beam

1. *Overview*

At Brookhaven National Laboratory, the production of positronium beam was carried out with the use of gases, on a HFBR based high flux positron beam line. As mentioned in the last chapter, the disadvantage of poor vacuum conditions using this process for positronium production are overcome by undertaking the present project. This project involves the use of carbon foils for positronium production and hence is a UHV compatible system. This can be used to carry out investigations on clean surfaces, without gas absorbants from the gases used in the earlier positronium production experiments. This new beam line uses a 30 mCi ^{22}Na source and a thin single crystal tungsten foil to produce a low energy positron beam, which is guided magnetically to a trap with the capability of storing these positrons, in a magnetic bottle at one end and an electrostatic mirror at the other end, and bunches these stored positrons at a rate of 1 kHz. These bunched positrons are made to hit a carbon foil target for the production of a positronium beam. This beam further has the capability of carrying out time of flight measurements, which in turn can provide useful information on the energy of positronium atoms reflected and diffracted from the solid surfaces[67]. This chapter is completely devoted to a discussion on the technical details of different components of this state of the art positron beam and the positronium beam. The last section of this chapter outlines the performance of this beam line and the present status of the project.

2. *Positron Beam*

A monoenergetic positron beam is constructed at BNL for carrying out investigations on the production of positronium atoms using thin carbon foils. The different kind of positron emission sources were discussed in detail previously in chapter 2. At BNL, there are two different means by which one can obtain monoenergetic positron beams. The most widely used one is radioactive β^+ decay from a ^{22}Na source and the other, not available at the moment, is radioactive β^+ emission from a ^{64}Cu source. It is expected to be available again by the end of this year, for use at the high flux positron beam facility recently built in Bldg. 480 of Brookhaven National Laboratory. Radioactive ^{22}Na is chosen for its reasonable half–life of 2.6 years, and the branching ratio for the positrons. The branching ratio is defined as the ratio of number of positrons emission to the total number of the decay emissions, and is 0.90 for a ^{22}Na source. The decay scheme for ^{22}Na is shown in Fig. 2.2.1 in chapter 2.

Positron Source

The ^{22}Na radioactive source used in this experiment was produced as a result of the development program undertaken at the Brookhaven to

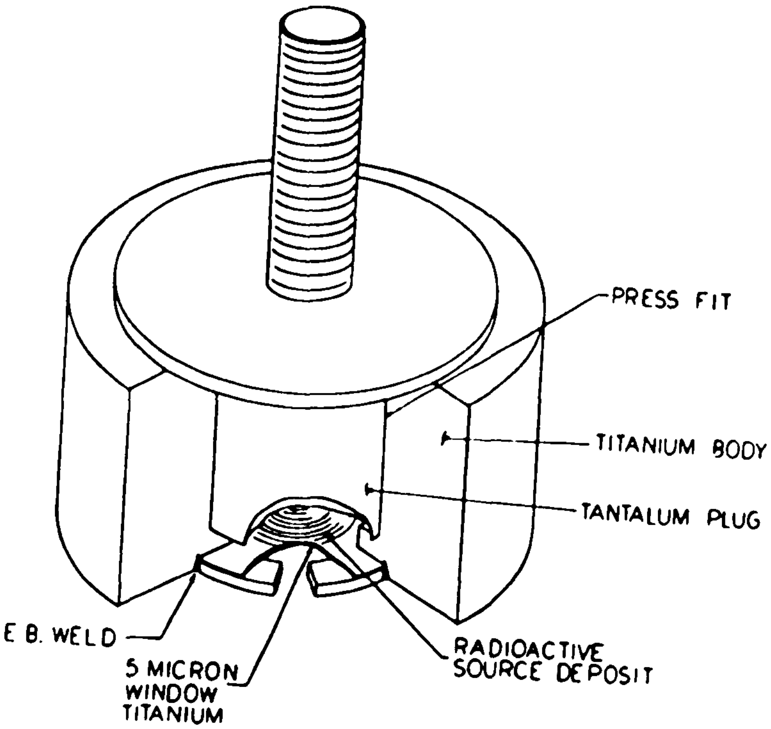

Figure 4.2.1 Schematic of the ^{22}Na source.

produce an intense, high positron yield ^{22}Na source [68]. A schematic of the ^{22}Na source capsule is shown in Fig. 4.2.1.

Details of the source deposition and the method used to determine the effective yield of β^+ are described in detail in the paper by Huomo *et al.*[68]. The source installed in this beam line had an activity of ~ 30 mCi, at the time of its installation in the beam, with a β^+ effective yield of ~ 25 %, and an active area of diameter ~ 6 mm.

Moderator

A detailed discussion on the processes involved in moderating the high energy positrons and the various geometrical configurations utilized for low energy positron beam production are described in chapter 2. The discovery of the moderation process revolutionized the low energy positron beam production by reducing the mean energy and the energy spread of the positrons. It also made it possible to enhance the usable range of the positron energy spectrum from various β^+ decay radioactive sources. The radioactive decay of ^{22}Na atoms produces positrons over a wide range of energy with the distribution having the shape of the usual β^+ decay spectrum. It is characterized by an end point energy of 0.545 MeV. The moderation process is usually performed with the use of a well annealed crystalline material, together with a radioactive source either in transmission or reflection geometry. The reflection mode of the moderator has the disadvantage of creating a shadowing of the source in the positron beam. On the other hand, the transmission geometry of the moderator has a well defined phase space for the positrons emitted by its surface and it is much easier to extract these positrons for transport with an electrostatic or a magnetically guided beam. Vane type moderators have the disadvantage of producing positrons with relatively large transverse energy spread [69].

The materials used for the moderator has a negative work function ϕ_+, for positrons, and the positrons emitted by the moderator surface are characterized by a typical mean longitudinal energy of $\sim$ 3 eV and an angular spread which is governed by the transverse energy of the emitted positrons.

The measured energy width (FWHM) for these emitted positrons is $\sim$ 75 meV at room temperature and this corresponds to an angular spread of about $\sim \pm 10^\circ$ normal to the surface of the moderator [32].

The historical development of different materials used for the moderators, with their efficiencies can be found in the literature [13,30]. The moderation efficiencies for different thin foils (thickness $\sim$ 0.3 to 7 μm), have been measured for many materials such as tungsten, nickel, tantalum, molybdenum, niobium, and copper [70]. These studies indicated that the moderator efficiency increases as the thickness of the single crystal decreases. Single crystals of tungsten and nickel provide the highest efficiency, $5.9(3) \times 10^{-4}$ and $6.6(3) \times 10^{-4}$ respectively. Although the nickel thin foil showed a higher initial efficiency, it degraded fast as compared with the tungsten thin foil when exposed to poor vacuum.

The tungsten single crystal has a good moderation efficiency and is not so sensitive to the vacuum conditions, making it a good choice for a moderator. For this beam, a 5000 Å thick foil of tungsten single crystal with (100) orientation was used. The thickness of the foil was of the order of the positron diffusion length L_+ inside the crystal. The moderator was sandwiched between two 90 % transmission high purity tungsten meshes. This mesh was spot welded onto a tantalum ring of thickness 0.040 inches, with an inner diameter of 10 mm. The moderator foil also had the same diameter of 10 mm. Before installing this moderator in the beam line, it was annealed and treated with oxygen in high vacuum (low 10^{-8} torr). This annealing was performed to ensure that the tungsten foil has large degree crystal ordering and very low density of defects. This enhances the moderator efficiency as positrons will not be trapped at impurity or defect sites and hence will have a large diffusion length.

The moderator assembly was mounted on a plate along with two extraction grids of 90 % transmission each. The plate itself was mounted on a six inch Conflat flange, and also had an electron gun assembly mounted on it. This electron gun can be used for annealing the moderator *in situ*. The chamber containing the source and the moderator assembly can be isolated from the rest of the beam line with a $4\frac{1}{2}$ inch gate valve, as shown in Fig. 4.2.2. The source end is maintained in UHV range (low $\sim 10^{-9}$ torr), with a Varian ion pump with pumping speed of 220 liters/sec.

The ^{22}Na radioactive source was mounted on a retractable linear feedthrough with 10 inch linear motion. This linear feedthrough is used to position the source on the beam axis and to center it with respect to the moderator assembly. Furthermore it can also be used to retract the source away from the moderator when the electron gun is used for annealing. The radiation from the radioactive source was completely shielded with a lead brick housing at the source end chamber of the beam line. The separation between the front of the source and the moderator was arranged to be $\sim 2-3$ mm, so that the large solid angle subtended by the source on the moderator surface produces the maximum number of high energy positrons incident on the moderator surface. The source and moderator assembly were also arranged so that both can be maintained at the same potential.

Positron Transport

The low energy positrons were electrostatically extracted from the source/moderator in transmission type geometrical configuration and were magnetically guided to the target. A schematic of this arrangement is shown in Fig. 4.2.2. The magnetic coils numbered 1 – 23 were used to transport magnetically the positrons from the source to the target. The different regions of the beam line as shown in Fig. 4.2.2 are discussed individually in more detail in the following sections. The positrons were transported from the moderator at very low energy, on the order of $\sim 2-5$ eV. For the positrons extraction from the moderator and their transport to the target, a special effort was made to ensure that positrons would not gain undesired transverse energy before they approach the region of the magnetic mirror. The axial magnetic field for transporting positrons was usually kept in the range of 100 – 110 gauss except in the region of the magnetic mirror.

Not shown in the schematic of the positron beam in Fig. 4.2.2 is a set of vertical and horizontal Helmholtz coils installed around the beam line to cancel out the effect of the residual earth magnetic field on the transport of the moderated positrons. This also helps to cancel the effect of the localized magnetic fields in the room. Eventually it can also be utilized to steer the beam along different regions of the beam line. The magnetic field in the magnetic mirror section was arranged to be more than twice the magnetic field used for transporting the positrons. The reason for this different magnetic field in the magnetic mirror region is explained in detail in the section on the magnetic mirror.

Once moderated positrons are electrostatically extracted from the source end, they are made to pass through a set of energy filters, named $\vec{E} \times \vec{B}$ filter. The $\vec{E} \times \vec{B}$ filter consists of a set of parallel plates so that the electric field between these parallel plates is transverse to the axial guiding magnetic field and hence to longitudinal velocity of the positrons. The effect of this transverse electric and magnetic field is to cause a drift in the gyration centre of the positrons, with a constant velocity [71] $\vec{u}$, where

$$\vec{u} = c\frac{\vec{E} \times \vec{B}}{B^2} \tag{4.2.1}$$

The transverse drift of the positrons depends upon their energy and the time they spend in the $\vec{E} \times \vec{B}$ region. The direction of the drift is independent of the sign of the charged particles, but does depend on the direction of the electric and magnetic field.

The beam line is also installed with two Hevi-Met (an alloy of tungsten and copper) collimators of 2 inch thickness and a 10 mm hole located off center by 0.625 inch and on center respectively. The off center collimator is located between two $\vec{E} \times \vec{B}$ filters, while the on center collimator is just after the second $\vec{E} \times \vec{B}$ filter. The positrons transported from the moderator consists of both low energy moderated positrons along with high energy positrons, which did not completely lose their energy in the thermalization process. To filter out these positrons, the moderated positrons are drifted off the axis of the beam line with the help of the first $\vec{E} \times \vec{B}$ filter and then brought back to the beam axis using the second energy filter. The high energy positrons transported along with the moderated positrons, do not get

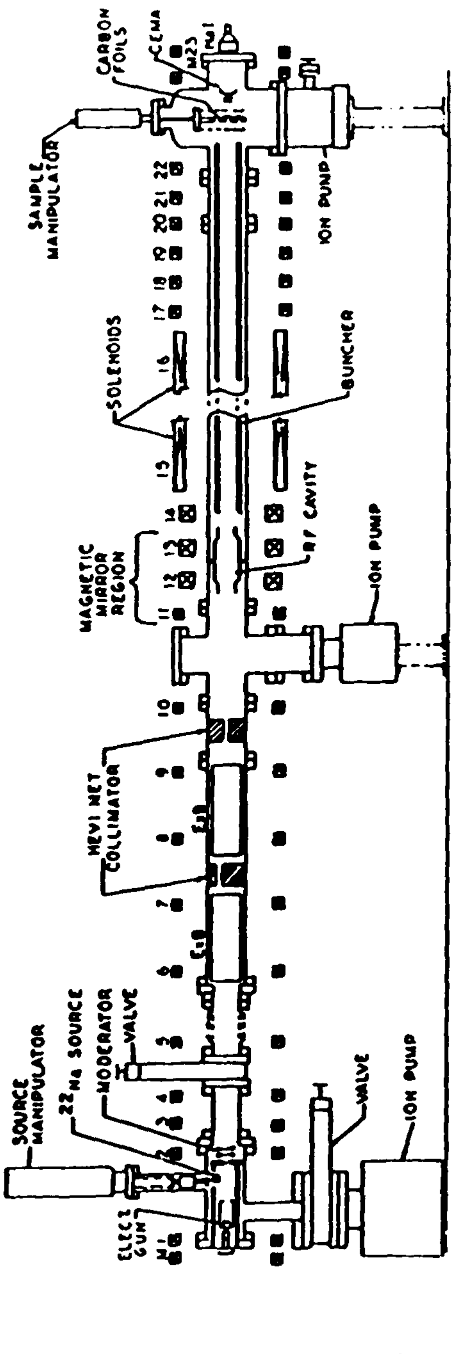

Figure 4.2.2 Schematic of the setup of the low energy positron beam for pulsed positronium. The labeled components are discussed in more detail in this chapter.

enough drift from the first $\vec{E} \times \vec{B}$ filter, as they spend less time in the filter than the moderated positrons. Hence these high energy positrons will be stopped and absorbed by the first collimator.

The total length of the beam line, shown in Fig. 4.2.2, from source to the target end, is $\sim$ 5.5 meter. The solid angle subtended by the moderator, with 10 mm diameter and a 10 mm aperture in the center of the Hevi - Met collimator, along with a detector of 25 mm diameter at the target end, is $\sim 10^{-5}$. Therefore in the present set up, both $\vec{E} \times \vec{B}$ filters along with the first off center Hevi - Met collimator are left out. However, if necessary, these $\vec{E} \times \vec{B}$ filters and the collimator can be installed at the positions indicated in Fig. 4.2.2. One of the disadvantage of using $\vec{E} \times \vec{B}$ filters is that they usually impart a transverse energy to the the positrons passing through them, due to the fringe fields at the edges of the parallel plates. In the present set up, it was crucial to avoid imparting any unnecessary transverse energy to the low energy positrons. Therefore, it was decided for the present experiment not to utilize any of the energy filters, but rather use a small solid angle to achieve a good signal to noise ratio.

The moderated positrons, on being transported further, make their way through the magnetic mirror, rf cavity, and finally through the buncher to the target chamber. In the target chamber, the positrons are detected either with a channel plate (CEMA) or a scintillator detector, on being annihilated at the annihilation plate. This beam can store the positrons in the combined region of the magnetic mirror and the active part of the buncher section of the beam line, and further bunch these stored positrons into a pulsed beam, whose pulse width (FWHM) is ~ 17 nsec. The buncher section of the beam line is responsible for providing this pulsed beam. The principles underlying these individual components utilized for storing positrons in a bottle, then bunching the stored positrons in the bottle, and then into a pulsed positron beam are discussed in the following sections.

Magnetic Bottle

For a charged particle in a uniform, static, magnetic field $\vec{\mathbf{B}}$ the transverse motion is periodic. The action integral for this transverse motion is given [71] as,

$$J = \oint \vec{P}_{\perp} \, . \, d\vec{l} \tag{4.2.2}$$

where $P_{\perp}$ is the transverse component of the canonical momentum and $d\vec{l}$ is a directed line element along the circular path of the particle. The canonical momentum is given as,

$$\vec{P} = \vec{p} + \frac{e}{c}\vec{A} \tag{4.2.3}$$

where c is the velocity of light in vacuum, $\vec{p} = \gamma m \vec{u}$ is the relativistic momentum, and $\gamma = \sqrt{1 - \frac{u^2}{c^2}}^{\,-1}$.

It is known that if a change in property is adiabatic i.e. slow as compared to the period of the motion, the action integral is invariant. In this case if the particle in motion is taken from a small magnetic field to a larger magnetic field which is changed adiabatically, the final motion of the particles will be such that the action integral has the same value as it had in the lower magnetic field. The action integral defined in Eq. (4.2.2), can also be written [71] as,

$$J = \gamma m\omega_B\pi a^2 = \frac{e}{c}(B\pi a^2) \qquad (4.2.4)$$

where $\omega_B = \frac{eB}{\gamma mc}$ is the gyration frequency of the particle in magnetic field B and $a = \frac{cp_\perp}{eB}$ is the gyration radius of the particle in magnetic field B. The quantity $B\pi a^2$ is the flux through the particle's orbit.

If the particle moves through regions where the magnetic field strength varies slowly in space or time, the adiabatic invariance of J in Eq. (4.2.4) means that the flux linked by the particle's orbit remains constant. If B increases, the radius a will decrease so that the quantity $B\pi a^2$ remains unchanged. This constancy of the flux linked with the particle motion can further be rephrased in several ways, involving the particle's orbit radius, its transverse momentum and its magnetic moment. These different statements all take the form that Ba^2, $p_\perp/B$, or $\gamma\mu$ are the adiabatic invariants, where $\mu = (e\omega_B a^2/2c)$, is the magnetic moment of the current loop of the particle in orbit. In the presence of static magnetic fields, the speed of the particle is constant and its total energy does not change.

A simple situation in which the magnetic field B is mainly in z direction, with a small gradient in the same direction, is illustrated in Fig. 4.2.3. In addition to the z component of the field, there is also a small radial component due to the curvature of the lines of force. For a cylindrical symmetric magnetic field B_0, the magnitude of the velocity of the particle is a constant. So at any position along the z axis, the velocity is,

$$v_\parallel^2 + v_\perp^2 = v_0^2 \qquad (4.2.5)$$

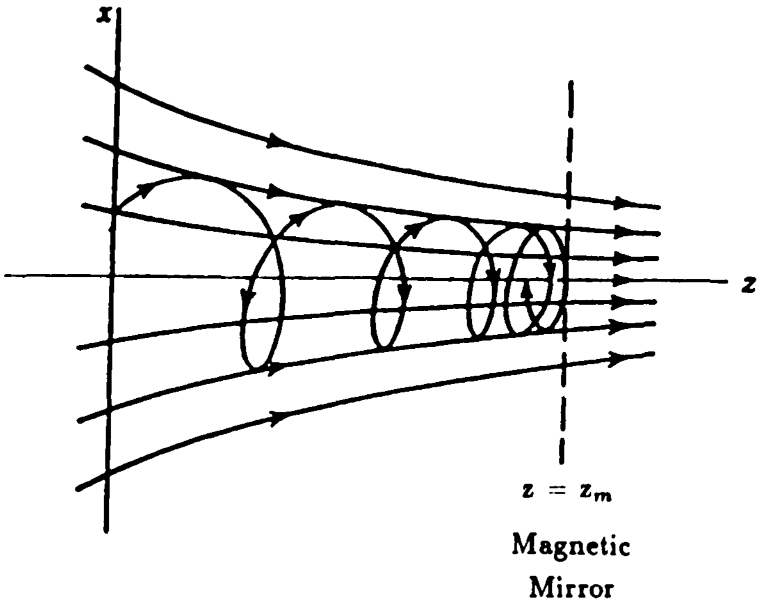

Figure 4.2.3 An illustration of the behaviour of a charged particle in a magnetic field with a gradient and its reflection from the region of the magnetic mirror. (from ref. 71)

where

$$v_0^2 = v_{\perp 0}^2 + v_{\parallel 0}^2 \tag{4.2.6}$$

is the velocity of the particle at $z = z_0$, and $v_{\parallel 0}$ and $v_{\perp 0}$ are the parallel and perpendicular components of the velocity of the particle at position $z = z_0$.

As the flux linked with the magnetic field is a constant of the motion, for two different regions of the magnetic field, it can be written as,

$$\frac{v_\perp^2}{B} = \frac{v_{\perp 0}^2}{B_0} \tag{4.2.7}$$

where B is the magnetic field at $z = z_1$. This relation can be used to find the parallel velocity at any position along the z-axis. Substitution of this relation in Eq. (4.2.5) gives,

$$v_{\parallel}^2 = v_0^2 - v_{\perp 0}^2 \frac{B(z)}{B_0} \tag{4.2.8}$$

If B(z) increases enough, eventually the right hand side of Eq. (4.2.8) will vanish at some point $z = z_m$. Physically this implies that the particles spirals in an ever tighter orbit along the lines of force, converting more and more of its translational energy into energy of rotation, until its axial velocity vanishes. Then it turns around, still spiraling in the same sense, and moves back in the negative z-direction. Hence the particles are reflected back by this spatially varying magnetic field. This is the principal behind the magnetic mirror i.e. the reflection of the charged particles by regions of strong magnetic field. The magnetic mirror is shown Schematically in Fig. 4.2.3.

The condition for particles to be reflected back is that the parallel component of the velocity $v_{\parallel}$ of the particle is zero. Therefore Eq. (4.2.8) can be rewritten, substituting v_0 from Eq. (4.2.6), as,

$$\begin{aligned} \frac{v_{\parallel 0}^2}{v_{\perp 0}^2} &= (\frac{B_m}{B_0} - 1) \\ \frac{v_{\parallel 0}}{v_{\perp 0}} &= \sqrt{(\frac{B_m}{B_0} - 1)} \end{aligned} \tag{4.2.9}$$

So from Eq. (4.2.9), it is evident that the criterion for trapping is,

$$\left| \frac{v_{\parallel 0}}{v_{\perp 0}} \right| < \sqrt{(\frac{B_m}{B_0} - 1)} \tag{4.2.10}$$

The magnetic field distribution as shown in Fig. 4.2.3 can be produced with solenoidal windings over some region of space, and additional coils at the end to provide a much higher magnetic field at that end. The particles injected in this magnetic field region will spiral, along the beam axis and be reflected by the magnetic mirror at the end. If the ratio of the field at the mirror end B_m, to the field away from the magnetic mirror B_0, is very large, then only particles with a very large component of the velocity parallel to the axis can penetrate.

If the particle velocity makes an angle θ with the direction of the magnetic field along z−axis, then the Eq. (4.2.7) can be expressed as,

$$\sin^2\theta = \frac{B}{B_0}\sin^2\theta_0 \qquad (4.2.11)$$

Here θ_0 is the initial value of θ in the region where the magnetic field value is B_0. For a magnetic mirror field B_m, all particles for which $\sin^2\theta_0$ exceeds B_0/B_m will be reflected back. This angular distribution of velocities can be related to a quantity called the coefficient of reflection R defined as the fraction of the particles reaching the magnetic mirror per unit time that are reflected, provided the velocity distribution is isotropic. For a particle with initial velocity v, the number of particles reaching the magnetic mirror per second, in the interval of solid angle $d\Omega$, will be proportional to $\cos\theta_0 d\Omega$. The coefficient of reflection is,

$$R = \frac{\int_{\theta_0=\theta_1}^{\pi/2}\cos\theta_0 d\Omega}{\int_{\theta_0=0}^{\pi/2}\cos\theta_0 d\Omega} \qquad (4.2.12)$$

where $\sin^2\theta_1$ equals B_0/B_m. As $d\Omega$ equals $2\pi\sin\theta_0 d\theta_0$, R simplifies to,

$$R = 1 - \frac{B_0}{B_m} \tag{4.2.13}$$

Since R does not depend on the assumed initial velocity, the same coefficient of reflection applies for an arbitrary velocity distribution, provided that the distribution is isotropic. It also shows that only particles with incident angle $\theta > \theta_0$ will be reflected by the magnetic mirror.

RF Cavity

The rf cavity is located between the magnetic mirror and the front end of the electrostatic buncher. It is shown in the schematic of the positron beam in Fig. 4.2.2. The rf cavity has the very crucial function of imparting a transverse energy component to the low energy positrons passing through, so that they satisfy the condition for trapping in the magnetic mirror on their trip back from the electrostatic mirror. The rf cavity is driven by a Hewlett Packard rf frequency generator model no. HP 608 F, together with an Electronic Navigation Industries (ENI) broadband power amplifier model no. 601L with capability of 30 dBm gain. The rf frequency generator can be tuned to a range of frequencies from 200 – 480 MHz. The frequency and the amplitude (maximum ~ 1 V) of the driving voltage from the rf generator are carefully tuned to excite the cyclotron resonance frequency of the positrons and their optimum trapping in the hybrid trap, made up of a magnetic mirror at one end and an electrostatic mirror at the other. The Q factor of the rf cavity used in this experimental setup is large. Therefore it is not necessary to have a very accurate and highly stable rf frequency generator.

A cross section of the rf cavity is shown in Fig. 4.2.4. The rf cavity has a set of parallel plates which act as capacitor plates. These plates are 1 in. apart, 2.5 in. wide, and 4 in. long. The parallel inductance is provided by the vertical plates. There is no insulator placed in the cavity to hold these plates, as they could charge up and deflect the low energy positrons. The input impedance of the rf cavity is ~ 50 ohm and no impedance matching elements are required to drive it. The electric field between the parallel plates is transverse to the axial magnetic field.

The motion of the positrons in this crossed static magnetic field and rf electric field with frequency ω is worth examining in detail. Motion where the angular frequency ω of the rf field is equal to the cyclotron frequency ω_c of the positrons, is responsible for imparting the required transverse component of the energy to these positrons in the magnetic bottle.

An oscillatory electric field can be written as,

$$E = E_0 \cos \omega t \tag{4.2.14}$$

where E_0 is the amplitude of the field and is perpendicular to the magnetic field B, and the frequency of the field ω $(= \frac{eB}{mc})$, is in resonance with the cyclotron resonance frequency ω_c of the positrons.

The equations of motion for positrons in this rf driving field are,

$$\begin{aligned} \ddot{x} &= \frac{e}{m} E_0 \cos \omega t + \frac{e}{mc} B \dot{y} \\ \ddot{y} &= -\frac{e}{mc} B \dot{x} \end{aligned} \tag{4.2.15}$$

Here the positrons are moving in the z direction and the magnetic field B is in the z direction.

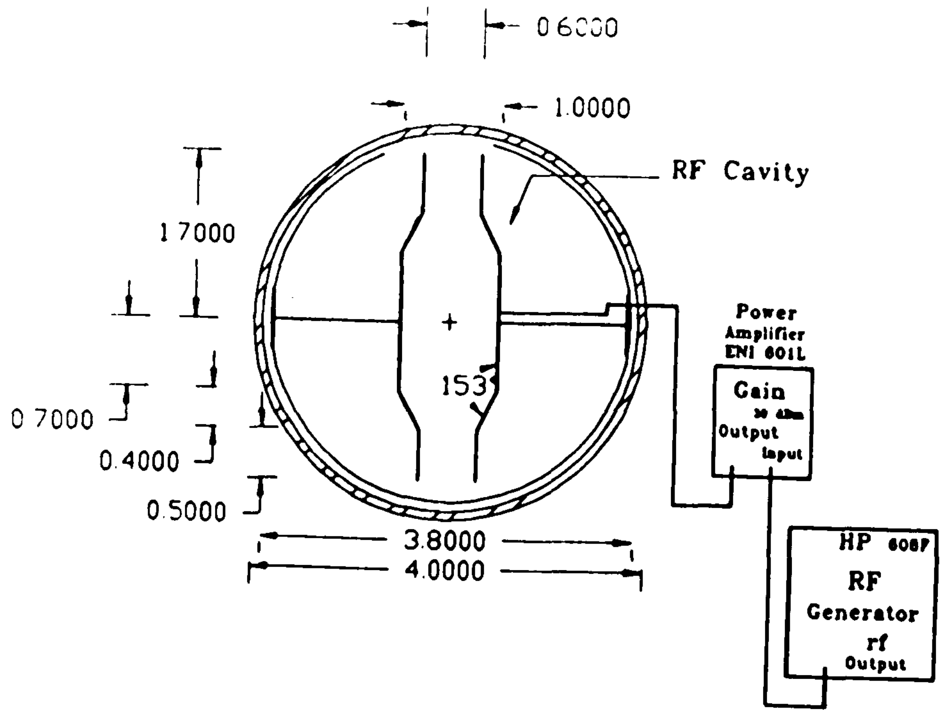

Figure 4.2.4 The cross section of the rf cavity for exciting cyclotron oscillations to trap positrons in the magnetic bottle. Also shown is the rf frequency generator and the amplifier used to drive the cavity.

Assuming the initial conditions,

$$x_0 = 0 \quad \text{and} \quad \dot{x}_0 = v_0$$

$$y_0 = r_0 \quad \text{and} \quad \dot{y}_0 = 0$$

where $r_0 = \frac{v_0}{\omega}$.

Integrating Eq. (4.2.15) and using the initial conditions, we have,

$$\begin{aligned} \dot{x} &= \frac{e}{m\omega} E_0 \sin \omega t + \omega y \\ \dot{y} &= -\omega x \end{aligned} \tag{4.2.16}$$

From Eq. (4.2.16), x can be eliminated and y can be given as,

$$\ddot{y} + \omega^2 y = -\frac{e}{m} E_0 \sin \omega t \tag{4.2.17}$$

and the solution to this equation of motion is,

$$y = \frac{v_0}{\omega} \cos(\omega t + \phi_0) - \frac{1}{2} \frac{e}{m\omega^2} E_0 (\sin \omega t - \omega t \cos \omega t) \tag{4.2.18}$$

Similarly Eq. (4.2.16) can be solved for x to give,

$$x = \frac{v_0}{\omega} \sin(\omega t + \phi_0) + \frac{1}{2} \frac{e}{m\omega} E_0 t \sin \omega t \tag{4.2.19}$$

The kinetic energy W of the positrons is,

$$W = \frac{1}{2} m (\dot{x}^2 + \dot{y}^2) \tag{4.2.20}$$

Differentiating Eq. (4.2.19) and Eq. (4.2.18) and substituting into Eq. (4.2.20) for $\phi_0 = 0$, the kinetic energy can be given as,

$$\begin{aligned} W = {} & \frac{1}{2} m v_0^2 + \frac{1}{2} E_0 e v_0 t + \frac{1}{8} \frac{e^2}{m} E_0^2 t^2 + \frac{1}{8} \frac{e^2}{m\omega^2} E_0^2 \sin^2 \omega t \\ & + \frac{1}{4} \frac{e v_0}{\omega} E_0 \sin 2\omega t + \frac{1}{8} \frac{e^2}{m\omega} E_0^2 t \sin 2\omega t \end{aligned} \tag{4.2.21}$$

In the equation above the first term represents the initial kinetic energy, the second increases linearly with time t, the third increases as the square of t, and the rest are oscillatory terms. These oscillatory terms do not have much significance. The time for which the impulse is given to the positrons in the cavity is short, therefore the third term mainly determines the absorption of rf energy by the positrons in the rf cavity.

Eq. (4.2.21) was considered for positrons with integration constant $\phi_0 = 0$. The effect of $\phi_0 \neq 0$ can be seen from the expressions for x and y in Eq. (4.2.19) and Eq. (4.2.18). As t increases, the term with factor ϕ_0 becomes negligible compared with the other terms. This means that the particles for which $\phi_0 \neq 0$ are eventually pulled into phase with the applied electric field and their energy W increases approximately as given by Eq. (4.2.21).

Electrostatic Buncher

The next component in Fig. 4.2.2 after the rf cavity is the buncher. This buncher and its related components were built under the direction of Dr. Allen P. Mills, Jr. at AT&T Bell Laboratories. Bell Laboratories also generously provided all the required parts and equipment needed for the project.

The basic constraint on any attempt to bunch particles is Liouville's theorem which states that the volume in phase space occupied by an ensemble of particles is conserved in the absence of dissipative forces [72]. Within this constraint, it is possible to increase the instantaneous intensity of a slow positron beam by trading energy resolution for spatial density.

The continuous beam of slow positrons is trapped in a magnetic bottle and bunched into short pulses using a parabolic accelerator [72]. The mechanical and electrical schematics for the electrostatic buncher are shown in Fig. 4.2.5. The positrons are trapped after passing through the pinched magnetic field at the entrance to the magnetic bottle with the use of a transverse rf field tuned to the positron cyclotron resonance frequency.

The buncher [73] is made up of 100 rings of non – magnetic 304 stainless steel and is 75 in. long. The rings have a 1.0 in. inside diameter, 1.375 in. outside diameter, and a length of 0.725 in. These rings were electroplated to avoid sharp edges. This helps in minimizing the perturbation of the uniform electric field along the rings and hence the buncher. These rings are supported on a 304 stainless steel frame. This stainless steel frame has 100 equidistant holes in the bottom plate consisting of ceramic mounts, holding the 100 rings of the buncher in place. The buncher rings are centered and electrically isolated from this frame by 0.5 in. diameter quartz insulator rods on each side. This assembly is shown schematically in Fig. 4.2.5. This whole assembly of frame and rings is arranged so that when mounted inside the beam line, made up of 6 in. conflat flange and 4 in. outside diameter vacuum tubing, the center of the rings of the buncher on this frame coincides with the center of the beam line.

The buncher accelerator is divided into two sections and these buncher rings are connected together with two separate resistor chains. The first one is an active part and the second one is a passive part. The length of the active part of the buncher is 45 in. while the passive part is 30 in. This division of the accelerator into two sections is useful in keeping down the spread in the positron bunch width. Ring number 49 is at about + 15 volts to repel the positrons prior to forming a bunched pulse, and hence it also closes the far end of the bottle. So positrons are trapped in a bottle

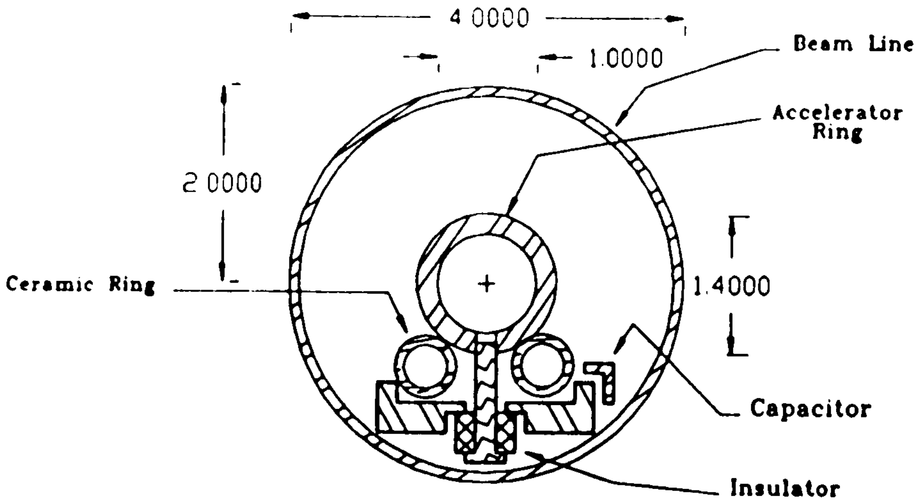

Figure 4.2.5 Schematic of the cross section of the buncher assembly, showing the buncher ring and its related support system.

consisting of the magnetic mirror at one end and the electrostatic mirror at the other end, i.e. ring number 49. The passive part of the accelerator is biased negatively at ring number 11. The first 39 rings, part of the passive part of the accelerator, are connected to the high impedance divider chain that approximates quadratic potentials at positions 11–49, of the form $V_z = \text{const.} \times z^2$. Here z–direction is taken along the beam axis and the origin is at the target. The resistors used for making this impedance divider chain are high precision metallic film resistors specially designed for ultra high vacuum application. Ring number 11 and a drift tube attached to it are biased at negative potential V_{11}.

The active part of the accelerator is designed to continue the quadratic potential and is actually a distributed 50 Ω attenuator. Buncher rings 50 – 110 are connected to the 50 Ω attenuator that continues the sequence of quadratic potential V_z = const. $\times z^2$. Parallel resistors are high power metallic thin film resistors. The values of different resistor are shown in Fig. 4.2.6. The series resistors leads were kept very short and were connected to the consecutive rings, by spot welding the short leads to thin foils of tantalum on each ring. This helped in minimizing the induction effect on delay of the propagating pulse along the buncher. A test pulse can be fed to ring number 110 and its delay to different parts of the buncher can be monitored. The parallel resistors as shown in Fig. 4.2.6. One end is connected to a capacitor plate C with capacitance $\approx 3nF$, and the other end of the capacitor is grounded. This capacitor is made by sandwiching a thin sheet of mica as a dielectric media between two stainless steel metal plates.

When a 5 nsec 10% – 90% rise time pulse is applied to ring number 110, the delay before it reaches ring number 58 is 4.2 nsec. The pulse spectrum at some of the resistors of the pulser is shown in Fig. 4.2.7. These spectrums were taken with LeCroy digital scope (model number 9450), with 350 MHz band width. The pulser used for the input pulse was from E – H research laboratories, model number EH 123A while the probe used to measure the output pulse from the accelerator was Tektronics model number P6122.

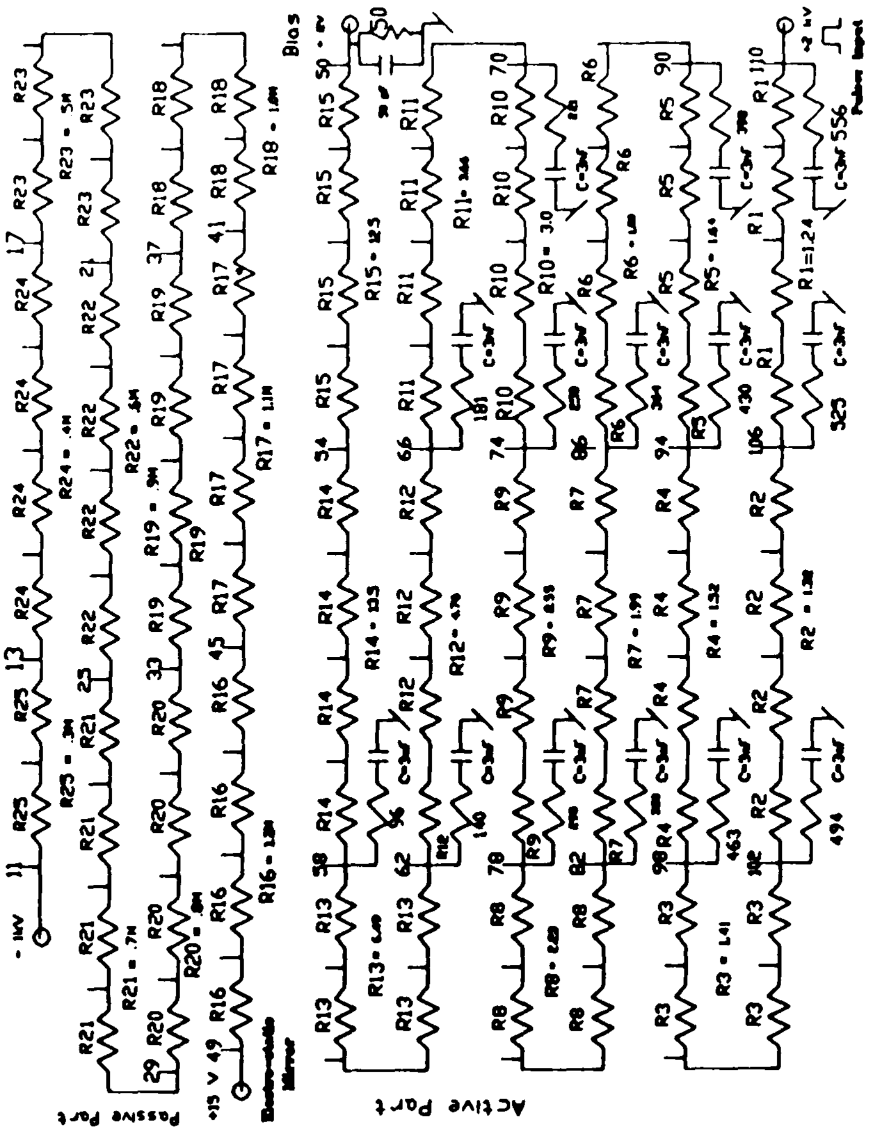

Figure 4.2.6 The schematics of the buncher voltage divider chain. It is arranged so that the impedance of the divider chain is matched with the driving source.

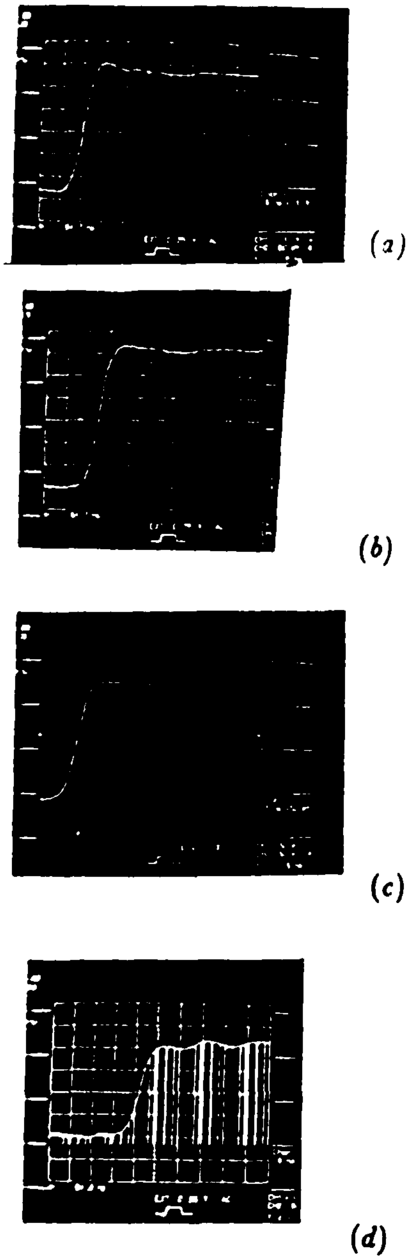

Figure 4.2.7 The pulse spectrum of the test pulse at different places in the accelerator. The front end of the pulse is shown at rings: (a) 110; (b) 98; (c) 86; and (d) 58 respectively.

The delay for the pulse propagation is ~ 1.3 times longer than that due to the velocity of light, principally because of the inductance of the series resistors and their connections. For an ideal case, with no inductance, this delay would have been ~ 3.3 nsec. At ring number 54, the rise time of the accelerator network is about 6 nsec with about ±10% overshoot.

The measured characteristic impedance of the the active part of the buncher installed in the 4.0 inch outside diameter beam line, between rings 110 and 50 is 50.2 Ω, while the impedance of the passive part between rings 49 and 11 is 29.10 MΩ.

Beam Pulser

The high voltage pulser for driving the buncher, is a thyratron based circuit [74]. A HY2 thyratron from EG&G Ortec is operated with a floating cathode. The grid of the thyratron is triggered by an avalanche transistor as shown in Fig. 4.2.8. The avalanche transistor is triggered by a pulse generator linked with a 1 : 1 transformer. The use of a zener diode across the avalanche transistor helps considerably in the improvement of the pulse shape. The pulser for triggering the avalanche transistor generates square pulses of amplitude ~ 2 – 5 volts and is usually operated at a frequency rate of 100 – 10,000 Hz.

The filament power is supplied through a high frequency transformer. This high frequency (~ 50 kHz) is generated by a Motorola programmable timer MC14536B, amplified by an Apex PA02 operational power amplifier and is finally linked to the heater tab by a transformer with a ratio of 2 : 1.

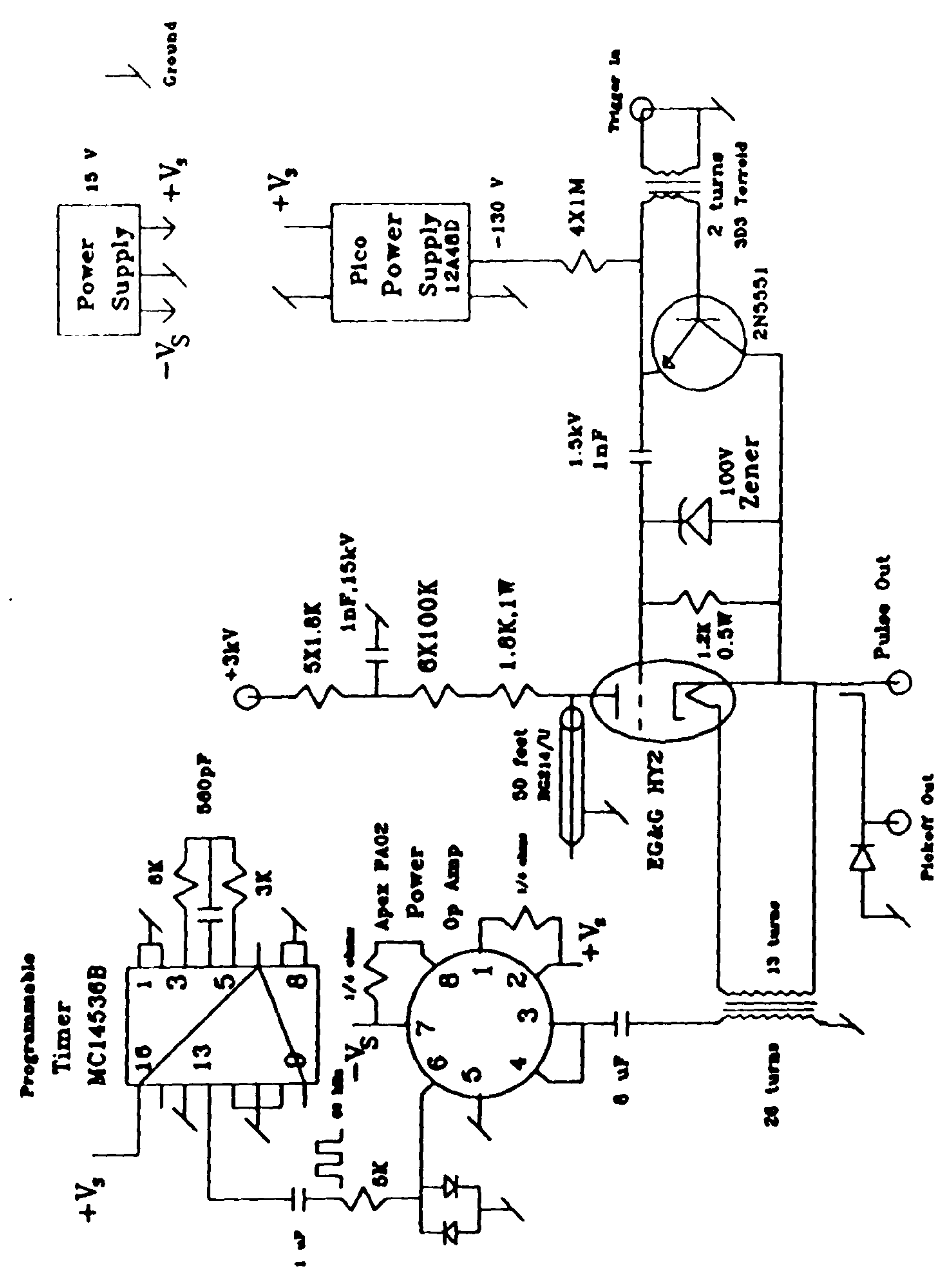

Figure 4.2.8 Schematic of the electrical circuit of the HY2 thyratron high voltage pulser that drives the accelerator section of the buncher.

The transformer has mylar tape insulation between its windings. This high frequency rf power supplied to the heater stub of the thyratron is adjusted to give 6.3 volts across the thyratron filament after it has warmed up. The anode circuit of the thyratron consists of a delay line for pulse shaping and a high voltage power input, V_A. The delay line is made up of a 50 foot long RG $-214/U$ coaxial cable. The output delay time is $\sim$ 150 nsec and its rise time is 15 nsec 10% – 90 %. This rise time of the pulse from HY2 thyratron to 15 nsec is achieved by adjusting the voltage $\pm$ V_s of the $\pm$ 15 volts power supply, as shown in Fig. 4.2.8.

The pulse output from the pulser is used to drive the active part of the accelerator, as discussed in the previous section, with characteristic impedance of $\sim$ 50 Ω. The typical width of the pulse is $\sim$ 200 nsec, more than the time required for collecting the positrons from the buncher. For example, the collection time for a buncher driven by a 2.5 keV pulse is about 100 nsec. The shape of the output pulses for three different input anode voltages V_A (from 1 to 3 keV) on the anode of the thyratron are shown in Fig. 4.2.9.

Whenever a pulse is generated by the pulser, a signal is picked up inductively. This inductively picked signal is used as one of the timing signal. This will be discussed more in the following sections.

3. Beam Operation

The moderated positrons are extracted electrostatically from the source chamber at low energy and transported with the axial guiding magnetic

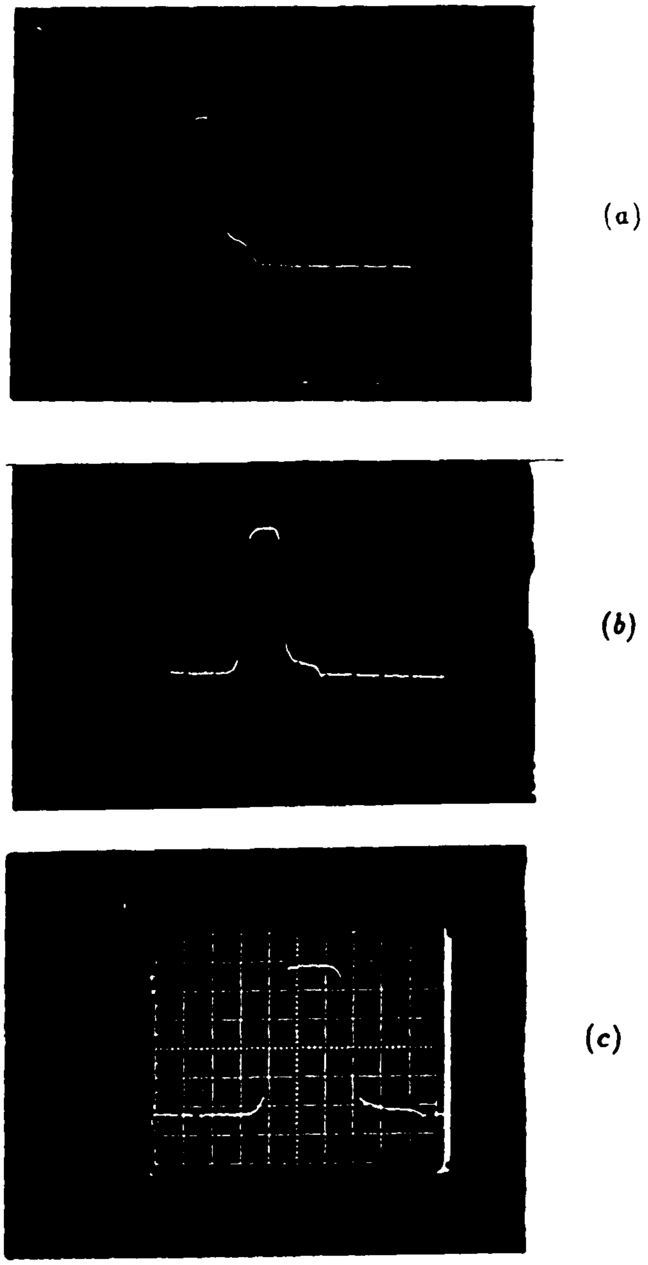

Figure 4.2.9 It shows the output pulse shapes from the pulser, driving a 50 Ω impedance load, for three different anode voltages V_A on the thyratron anode. The V_A voltages are 1, 2, and 3 keV respectively.

field to the target end. The voltage at the source/moderator assembly is $\sim$ 2.5 volts while the grids on the moderator assembly are grounded. The typical guiding field is $\sim$ 100 gauss along the whole beam line except in the region of the magnetic mirror. This region has a magnetic field ranging between $\sim$ 200–250 gauss, as shown in Fig. 4.2.2. Those low energy positrons with very small transverse energy component make it through the magnetic mirror region, are trapped in the magnetic bottle, and subsequently bunched into a short pulse using a parabolic potential accelerator. The positrons are trapped in the magnetic bottle after first passing through the pinched magnetic field at the entrance to the magnetic bottle and then through a transverse electric field tuned to the positron cyclotron resonance frequency. These positrons are imparted with a high transverse energy $E_\perp$ when they pass through the rf cavity. The frequency and the amplitude of the rf driving voltage is carefully tuned for optimum trapping. For the magnitude of magnetic fields mentioned earlier, the rf cavity tuning parameters are typically $\sim$ 280 MHz and amplitude of $\sim$ 0.8 volts for the optimal storage of the positrons in the magnetic bottle.

As discussed in the section on the magnetic mirror, the magnetic mirror transmits the particles if the ratio ($\frac{E_\parallel}{E_\perp}$) of the longitudinal ($E_\parallel$) to the transverse ($E_\perp$) energies for these particles is greater than $(B_m/B_0 - 1)$, where B_0 is the value of the magnetic field outside the mirror region while B_m is in the mirror region. The accelerator ring 49 is kept at a positive voltage and is adjusted to repel back the positrons during the accumulation period. This acts as an electrostatic mirror and closes the end opposite to the magnetic mirror in the bottle during this accumulation period for the positrons.

The active section of the buncher is also biased at a small positive voltage in order to slow down the positrons in the accumulation region. This is done by applying a positive voltage very close to the positron beam energy to ring number 50. This end is also terminated with a combination of a 50 Ω resistor and a capacitor. If the magnetic field B_0 is uniform, positrons will return back to the rf cavity in phase and again reflect back from the magnetic mirror. However, a non uniform field can cause an indefinite phase shift among the positrons. Therefore an effort is made to make the magnetic field uniform, with the use of solenoids, in the region of the accumulation stage of the buncher, as shown in Fig. 4.2.2. The positrons are dumped out of the magnetic bottle by the accelerator section as shown in Fig. 4.3.1.

In the active part of the buncher, the values of the resistors between the rings are chosen to make a quadratic potential well, whenever a high voltage pulse from the pulser is applied to the front end of the accelerator at ring number 110. The positrons initially have low velocity in the accelerator section and thus all will arrive at the minimum of the quadratic potential after one quarter of a simple harmonic oscillator period. The target is placed at this minimum 7.5 inches away from the last ring 11 of the passive part of the buncher. The active part of the accelerator is usually operated at 1 kHz or lower frequncy, and it is limited to this repetition rate because of the heating of the resistor chain in vacuum. When the buncher is operated, the

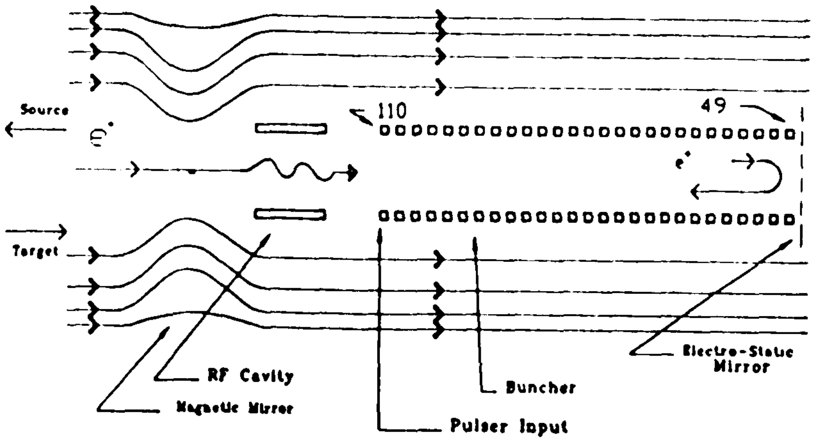

Figure 4.3.1 Schematic of the beam section containing magnetic mirror, rf cavity, active part of the buncher, and the electrostatic mirror region.

potential distribution along the length of the buncher looks like the quarter period of the simple parabolic potential as shown in Fig. 4.3.2.

As shown in Fig. 4.3.2, the front end of the buncher at ring number 110 has much higher voltage than the voltage on the electrostatic mirror end, at ring number 49. This makes all the positrons collected in the active region of the accelerator between ring numbers 100 and 49 dump out of the bottle

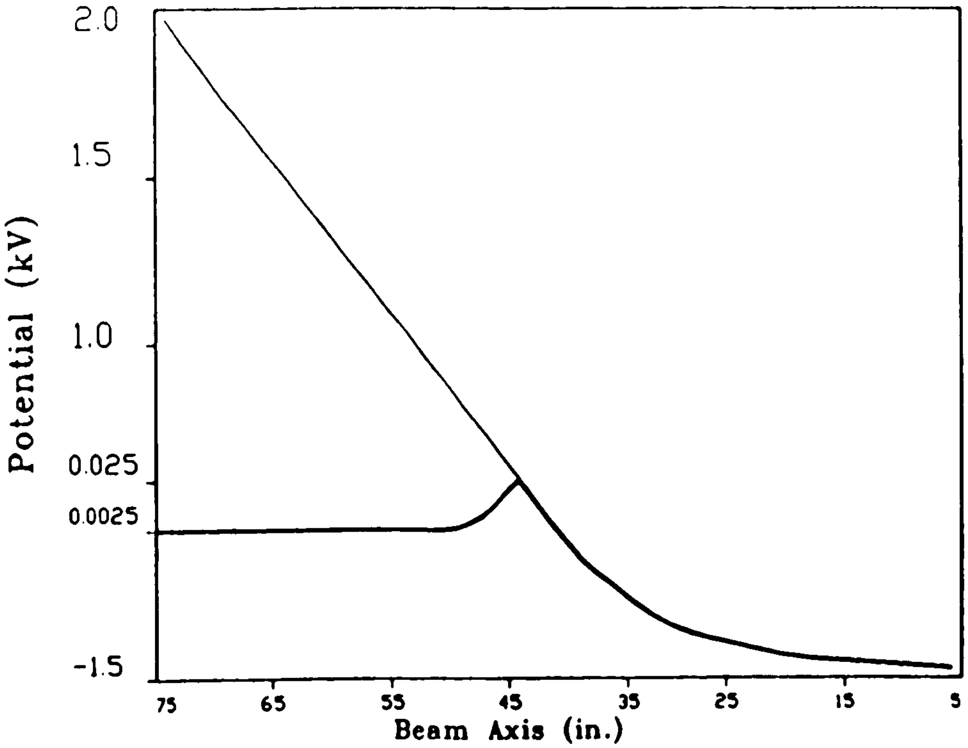

Figure 4.3.2 The potential distribution on the active and passive part of the buncher. The solid line indicate the pulsed potential distribution on the active part of the accelerator, when pulsed. The dark solid line indicates the potential distribution over the whole buncher during the accumulation stage.

and get bunched at the minima of the quadratic potential, which is also the center of the target chamber. It takes about 100 nsec for all the positrons collected during the accumulation period of the buncher to clear out of the whole length of the buncher.

The bunched positrons are detected at the center of the target chamber either by a 3 inch × 3 inch NaI(Tl) scintillator detector or a channel plate (CEMA : channel electron multiplier array). This channel plate is mounted on a linear feedthrough and is capable of 3 inch travel along the beam axis. It is also arranged so that when the target is mounted, the target sits at the center of the target chamber. The center of the target chamber is also arranged to be the minima position for the quadratic period of the harmonic potential well. The channel plate then can be moved back and forth behind the target on the beam axis and hence it is possible to change the solid angle subtended by the detector. The minimum distance that the channel plate can approach the target is $\sim$ 1 inch. A grid with 90 % transmission is placed behind the target, between the target and the channnel plate. This grid is used to repel charged particles, when the target is positioned at the beam line axis.

The photomultiplier tube used with the NaI(Tl) detector is a RS2238 photomultiplier manufactured by Hamamatsu. These tubes are designed so that they are less sensitive to magnetic fields than conventional ones. For detection using a NaI(Tl) scintillator, the positrons are annihilate first on an annihilation plate and then 511 keV γ−rays are detected with the NaI(Tl) detector. In case of channel plate detector, the positrons annihilate at the front plate of the detector itself. Later, the same channel plate is used for detecting the positronium beam. The channel plates efficiency for detecting γ−rays is about 10^{-3} while for charged particles it is much higher. This reduced sensitivity to γ - rays helps to reduce background from annihilating positrons at the target.

The target is mounted on a linear feedthrough capable of linear travel of 3 inch. The target holder consists of three $\frac{3}{4}$ inch holes. One hole is used to mount a 50 Å thick carbon foil on a grid mesh. The carbon foils are described in the section on the positronium beam. Another hole is covered with a stainless steel plate while the last hole is left open. This open hole is used for alignment of the beam and the target, while the hole covered with a stainless steel plate is used for measuring background counts.

4. Performance of the Beam

The performance of the rf cavity, magnetic mirror, and the buncher installed in this beam line is monitored by detecting positrons with the CEMA and then carrying out timing analysis of the detected positrons with respect to the signal from the pulser, which is also used for triggering the front end of the active part of the buncher.

Schematic of the necessary electronic setup is shown in Fig. 4.4.1. The pulse from the buncher used for driving the active part of the buncher is utilized as a start signal for the time to amplitude converter (TAC), and positrons stored in the buncher, on their arrival at the CEMA in a bunched form provide a stop signal. The typical efficiency of the CEMA for charged particles like electrons is 50 - 85 % in the energy range of 0.2 - 2 keV and 10 - 60 % in the energy range of 2 - 50 keV [75]. Positrons arriving at the

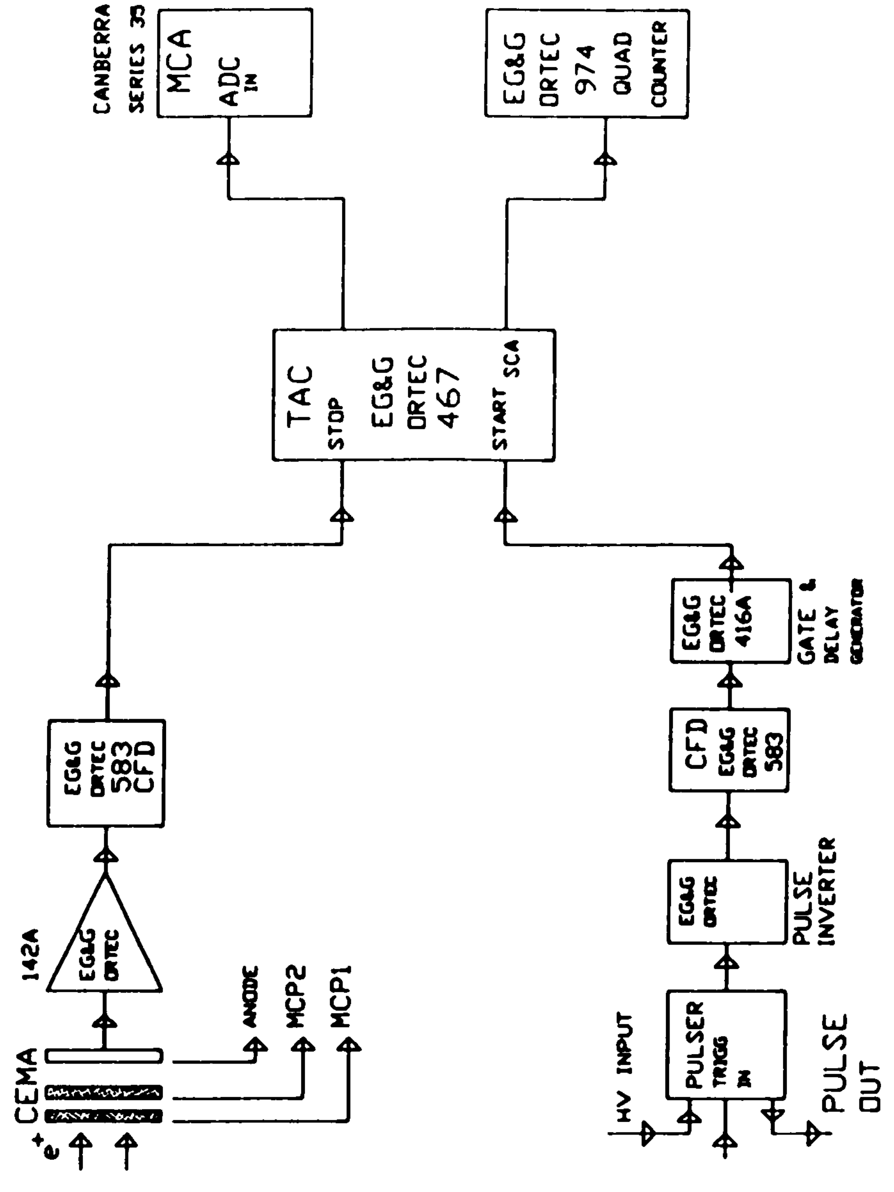

Figure 4.4.1 Schematic of the electronic setup for carrying out timing analysis of the positron bunches with respect to signal for triggering the front end of the buncher.

CEMA from the magnetic bottle and the active part of the buncher are correlated in time with the driving signal of the active part of the buncher. The spectrum of this time correlation was recorded on a Canberra series 35 multi channel analyzer (MCA). A typical time spectrum of the positrons arriving at the CEMA when the active part of the buncher was driven at 1 kHz is shown in Fig. 4.4.2. This data was collected for 5000 sec and the time window on TAC was 400 nsec. The channel numbers can be converted to time scale by multiplying channel numbers with a conversion factor of 0.098 nsec/channel. The maximum stop signals due to the bunched positrons at the CEMA were about 720 for 1 kHz rate of the start signals from the buncher. It was also observed that the rate of stop signals drops by at least a factor of 7 when the rf cavity was turned off or tuned away from the cyclotron resonance condition. The remaining signals were either due to the low energy positrons in transit in the buncher during the triggering of the buncher or the high energy positrons. The data in Fig. 4.4.2 shows the subtracted spectrum of beam on and beam off.

The bunched pulses of the positrons for this setup of the buncher and under the operating conditions described in the earlier sections of this chapter gave a time distribution of full width half maximum (FWHM) of $\sim$ 17 nsec. This time spread consists of both contributions from the electronics and from delay in pulse propagation along the buncher. The time spread in the pulse because of the contribution due to the buncher alone typically is about 8 nsec [73]. In the absence of the magnetic bottle, there was no indication of any peak in the time spectrum as the arriving positrons had no time correlation with the start signal. The shape of the timing spectrum in Fig. 4.4.2 was very much dependent upon the position of the CEMA with respect to ring number 11 of the buncher. With rough estimates of the efficiency of the source and the 63 % combined efficiency of the buncher and the bottle [73], it was estimated qualitatively that there were at least one to two positrons per pulse and the positrons were able to get trapped in the bottle at least in the range of 10^{-6} to 10^{-5} sec. This conclusion was based upon the estimates on the efficiency of the CEMA (50–85 % for positrons in the energy range of 300 eV to 2 keV) and a flux of 1×10^5 e^+/sec from the moderator. It was not possible at present to measure quantitatively the number of positrons per pulse due to the lack of equipment such as a digital storage oscilloscope and a fast scintillator detector. The number of positrons per pulse quoted here is only a lower limit on the possible number of positrons per pulse.

5. *Positronium Beam*

The positron pulses obtained from the buncher were made to strike a 50 Å thick carbon foil. The target was arranged to be about 7.5 inches away from the last ring (number 11) of the buncher, which is coincident with the minimum of the quarter period of the potential distribution of the buncher. The target, i.e. the carbon foils of varying thickness, was obtained commercially from Arizona Carbon Foils Co. [76] and delivered on glass slides. These foils were floated off onto a water surface and then mounted on

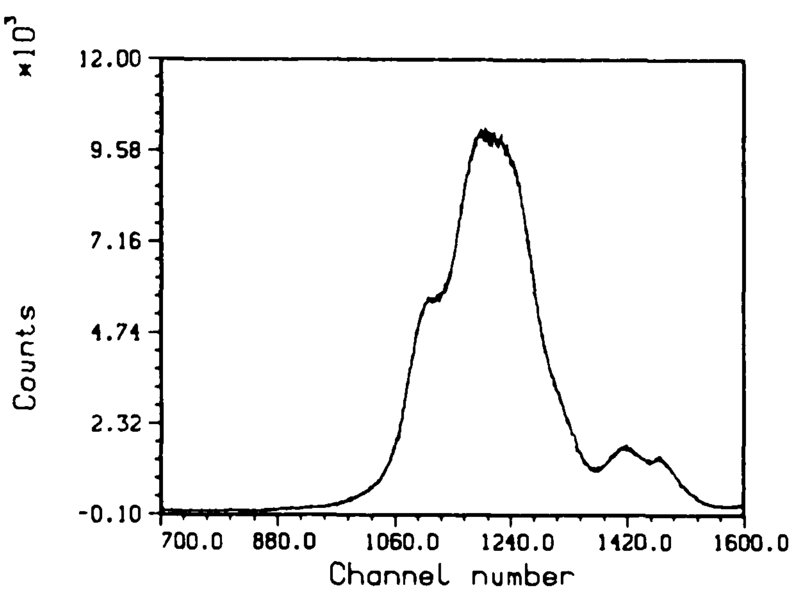

Figure 4.4.2 Typical time spectrum of bunched positrons arriving at the CEMA. The buncher was driven at 1 kHz. The zero of the time scale was taken as the opening of the electrostatic mirror end of the buncher. The channel numbers can be converted to time scale by multiplying it with 0.098, i.e. the conversion factor is 0.097 nsec/channel.

a target holder, which had a copper grid mesh with ~ 20 lines/inch, covering the 3/4 inch diameter hole in the target holder.

A positron on passing through the carbon foils can pick up an electron at the exit surface of the foil and with this process of charge exchange can form a positronium atom. Beside this process, it is also possible for positrons to undergo other processes such as Ps^- formation [60]. Positronium formed on transmission through the carbon foil was detected with the channel plate located about ~ 1 inch behind the foil while the grid in between the target and the channel plate was biased positive at $\sim +1200$ V with respect to the target to repel positrons which did not succeed in making positronium in their first trip through the target. The target potential was kept in the range of -300 to -500 volts. The front end of the channel plate was kept at a potential of ~ -1850 V while the anode was at $\sim +400$ V. This combined arrangement of potentials had a potential distribution such that the target was always at the minimum potential seen by the positrons while other potentials were arranged so that high energy positrons, secondary electrons, and other charged particles will be reflected before they would reach the detector and make a contribution to the signal at the detector.

With the assumption of about 2 e^+/pulse, at the rate of 10^3 pulses/sec, there will be about 2×10^3 e^+/sec incident on the carbon foil target. When the detector is located about 3 cm behind the target, the solid angle subtended by the detector at the target will be ~ 0.44 steradian. From earlier measurements by Mills *et al.*[61], the efficiency for ortho-positronium production with a detector solid angle of 0.44 steradians is about 2.6×10^{-2} positronium atoms per incident positron in the energy range of 1 eV to 500 eV. For the present case, the number of positronium atoms expected for 2000 e^+/sec (or 2 e^+/pulse) incident positrons and the detector subtending a solid angle of about 0.44 steradians will be about 52 Ps/sec, provided the efficiency for positronium detection by the channel plate is 100 %. But it is known that the efficiency for positronium detection by channel plate is dependent upon the energy of the positronium atoms and hence it is not expected that all the positronium atoms incident upon the detector will be detected and result in a signal. The fast positrons were the major source of constant background contribution to the signal during the positronium formation measurements. Typically there were about 14 stop signal due to fast positrons, for every 1000 starts in the 400 nsec time window at time to amplitude converter. With this constant background presence it was not possible to extract the positronium signal and make a very conclusive estimate on the efficiency for the positronium formation. However with conservative estimates, it could be concluded that the number of positronium atoms from a 50 Å thick carbon foil, detected on the channel plate was at least (7 ± 3) Ps/sec.

After carrying out many investigations with a 50 Å thick carbon foil as the target, it is concluded that with the present flux of positrons ($\sim 1 \times 10^5$ e^+/sec), it is not very conclusive to obtain a good estimate on the efficiency for the positronium production. Also for the same reason, it is extremely difficult to carry out investigations of the energy and the angular distribution of the positronium atoms produced. It is expected that in the future with the use of a higher intensity positron source from the high flux positron beam in Bldg. 480 at Brookhaven National Laboratory, it will be possible to continue investigations of positronium formation efficiency, angular distribution, and energy distribution of the positronium atoms.

Chapter 5.

Studies on SiO_2/Si(100) Systems

1. *Overview*

The importance of the SiO_2/Si system in modern electronics has made it an extensively studied system. The microscopic details of this system is not well understood and therefore there has been a great effort to get more insight utilizing techniques such as Transmission Electron Microscopy (TEM), Rutherford Backscattering Spectroscopy (RBS), Secondary Ion Mass Spectroscopy (SIMS), and Capacitance–Voltage (C–V) measurements. The shortcomings of some of these techniques has led to the utilization of Positron Annihilation Spectroscopy (PAS) to study these systems. Positrons are very sensitive to defects and are non destructive compared to other common techniques.

This chapter contains studies of SiO_2/Si(100) systems with PAS. In the first section of this chapter, processes for oxide growth on silicon substrates and the details of interface passivation are discussed briefly. The following section contains an introduction to the parameters and the concepts involved with PAS measurement technique. Finally some measurements utilizing PAS are presented and particularly measurements of hydrogen activation energy from interfaces of both n– and p–type substrates and the effect of irradiation on oxides are discussed in details.

2. Introduction

Variable energy positron beams have found a wealth of applications in the studies of surfaces, interfaces, thin films, multilayer structures, and buried layers [13]. Recently there has been much research concentrated on the studies of SiO_2/Si systems, due to its technological importance in the microelectronics industry [77]. The sensitivity of positrons to defects has played an important role in the understanding of oxides and interface defects of SiO_2/Si systems[78].

Oxidation Processes

Oxide layers in silicon integrated circuits provide surface passivation for a silicon device, work as diffusion masks, and isolate one device from another. Oxide layers grown on silicon substrate require control such that the electrical characteristics of the device are dominated by bulk rather than surface properties. This requires that the interface between silicon and the oxide should have a minimum, stable density of fixed oxide charge and interface traps, and the oxide must be sufficiently thick that the potential gradient along the air – oxide interface has a minimum influence on the semiconductor properties.

Silicon surface is highly reactive by nature, so that a layer of oxide forms rapidly on exposure to an oxidant gas and its rate of formation is reaction limited. As the oxide layer becomes thicker, its rate of formation becomes diffusion limited because the silicon and the oxidizing ambient are separated by the oxide layer and oxidant has to diffuse through this oxide layer. The oxidation process involves the sharing of valence electrons between oxygen and silicon to form four silicon–oxygen bonds. Each bond is largely covalent with a small ionic component at room temperature. This ionic component becomes more important at elevated temperatures. The oxide is usually grown either in a dry atmosphere of pure oxygen or in an atmosphere of water vapor. These growth conditions are known as dry and wet oxides respectively.

The stoichiometric chemical reaction for dry oxide growth is,

$$Si(solid) + O_2 \rightleftharpoons SiO_2(solid) \tag{5.2.1}$$

whereas the stoichiometric chemical reaction for wet oxide growth is,

$$Si(solid) + 2H_2O \rightleftharpoons SiO_2(solid) + 2H_2 \tag{5.2.2}$$

These reactions occur when a silicon surface is exposed to an oxidizing ambient, typically at a pressure of 1 atm., and at elevated temperatures in the range of $\sim 900-1200$ C. The rate of oxide growth is limited by availability of the reactants, namely, oxidant molecules and silicon–silicon bonds. Initially, oxide growth rate is limited by the availability of silicon–silicon bonds, as there are more than enough oxidant molecules present at 1 atmosphere. The supply of oxidant molecules becomes the limiting factor as an oxide layer grows as this oxide layer now separates the oxidant molecules in the ambient from the silicon–silicon bonds. Now the oxidant has to diffuse through the oxide layer in order to react at the Si–SiO_2 interface.

The oxide film is not coplanar with the original silicon surface because of a volume expansion during the oxidation process, due to the differences in the density of substrate and the oxide layer. The density of SiO_2 (2.21 g/cm^3) is slightly less than that of the silicon (2.33 g/cm^3). Oxides grown in pure dry oxygen have the best electrical properties, but require considerably longer time to grow the same thickness of oxide, at a given temperature, than in water vapor.

Passivation of Oxide Interface on a Silicon Substrate

The process of passivation is carried out to minimize undesirable surface effects and is usually obtained by forming a thin insulating layer of thermally grown oxide on the semiconductor surface [79]. This oxide layer also helps in preventing the contaminants from being injected into the surface devices. The oxide structure can be described as a noncrystalline continuous random network. The flexibility in the bond angles of Si–O–Si in SiO_2 makes it possible for the oxide to adjust to the crystalline silicon structure and make saturated chemical bonds at the interface of the oxide and the silicon. Both intrinsic and extrinsic impurities contribute to imperfections at the interface region of the oxide and the silicon. Parameters such as a mismatch of 6 % between silicon atom positions in silicon and silicon oxide create an intrinsic interface strain. The lower density of silicon atoms in oxide ($\sim 2.5 \times 10^{22}\ cm^{-3}$) as compared to silicon ($5 \times 10^{22}\ cm^{-3}$) also contributes to defects at the interface in the form of broken bonds. These intrinsic imperfection sites are chemically active and very likely to attract impurities. It is hard to distinguish individual contributions from intrinsic structural defects and extrinsic impurities.

Detailed accounts of the present understanding of the SiO_2/Si system can be found in excellent review articles summarizing work performed over three decades [80-82]. Three kinds of defects have been previously identified in the SiO_2/Si systems, classified as fixed oxide charge, interface trapped charge, and fixed trapped charge[83-84]. These defects along with their charges are shown schematically in Fig. 5.2.1.

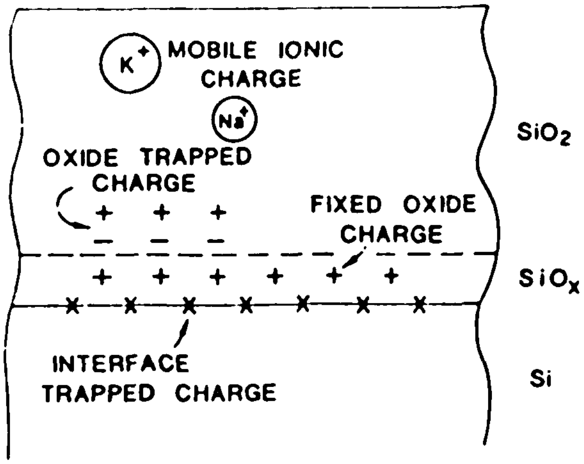

Figure 5.2.1 Schematics of different kinds of defects in thermally grown oxide on a silicon substrate. (from ref. 84)

Fixed oxide charge is positive and known to be located near the interface, about 25 Å from the $Si-SiO_2$ interface. These charges are immobile and do not exchange charge with the silicon, hence are not in electrical communication with the underlying silicon. This fixed oxide charge is not affected by hydrogen in oxidation or annealing processes. The origin and the mechanism of creation and annihilation of these charges is presently not well understood [81,85]. Techniques for controlling these defects in devices are largely empirical [83,86]. Interface traps refer to electrons or hole traps localized at interface sites that can change their charge states by exchange of carriers with silicon. The trap occupancy and the total charge in these traps changes with the surface potential. The broad distribution of trap energy levels throughout the silicon band gap indicates that there are several kinds of traps that leads to this energy distribution [81,87]. One kind of traps is a broken bond in which a silicon atom is bonded to only three other silicon atoms. The unpaired electron of this silicon atom (the trivalent silicon with a dangling bond) is chemically active. The observed reduction in interface traps at low anneal temperatures (400–500 C for 5–10 min) in the presence of hydrogen [88-89] is believed to be due to passivation of the unpaired electron with a hydrogen atom. Trivalently bonded silicon at the SiO_2/Si interface is also known as a P_b center, and has been verified experimentally [90-91] with experiments using electron spin resonance (ESR). The detection of P_b centers is mainly due to the fact that the spin of the unpaired electron localized at the trivalently bonded silicon atom interacts with the magnetic field used in ESR. The suggestion of hydrogen passivation of the dangling bonds has been supported by the reduction in the P_b centers after anneal in a hydrogen ambient.

Finally, oxide trapped charges are a property of the bulk oxide and prevails everywhere in the oxide. Trapped charges could be either positive or negative due to holes or electrons trapped in the bulk of the oxide. The effect of trapped charges is profound when they are located near the interface region. The control of oxide quality is important for minimizing these defects.

3. Investigation of SiO_2/Si with Variable Energy Positron Beam

The variable energy positron beam at BNL is utilized to carry out experiments on the SiO_2/Si systems. This beam has the capability of providing positrons with energy from 100 eV to 60 keV. The details of this beam can be found elsewhere [92]. The positrons annihilate with electrons in the sample and the energy distribution of these annihilating positrons is measured with a high purity Ge detector. The detected energy of the emitted γ - rays from these annihilating positrons is Doppler shifted and this shift is dependent upon the momentum of the electron–positron pair. Since the implanted positrons are thermalized before annihilation, the Doppler shift characterizes the electron momentum prior to the annihilation and is very sensitive to whether these positrons were in a freely diffusing state or in a trapped state at a defect site, at the time of annihilation. In Positron Annihilation Spectroscopy (PAS), it is common to quantify the Doppler broadening by a line shape parameter, called the S–parameter [93]. The S–parameter is defined as the ratio of the counts n, counted under a small fixed energy interval around the center energy of 511 keV to the total number of counts N, in the photopeak, i.e.

$$S = \frac{n}{N} \tag{5.3.1}$$

The S-parameter reflects the narrowness of the energy spectrum and this narrowness is a function of the momentum distribution of the electrons annihilating with the implanted thermalized positrons. A lower electron momentum around the annihilation site produces a sharper annihilation spectrum and hence a higher S-parameter value and vice versa. Typically materials with open-volume-type defects produce a sharper annihilation spectrum and hence a larger S-parameter value. For optimum sensitivity, the window of the central region which determines n in Eq. (5.3.1) for calculating S-parameter, is adjusted so that the S-parameter value is $\sim$ 0.5[94]. A typical S-parameter line shape is shown in Fig. 5.3.1.

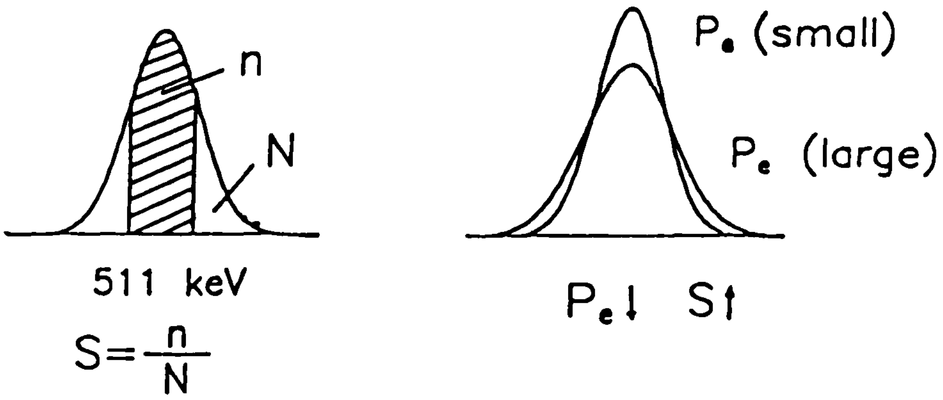

Figure 5.3.1 The schematics of the typical line shape of S-parameter is shown together with the effect of electron momentum P_e on the shape of S-parameter. (from ref. 92)

Positron Implantation and Diffusion

Implanted positrons in a solid thermalizes rapidly and then diffuse around until they annihilate with an electron by emission of two γ – rays, with an energy of 511 keV each. The thermalization time for the positrons is small compared to their lifetime. The positrons thermalize typically on a time scale of $\sim 10^{-12}$ sec whereas their typical lifetime in the materials is $\sim 10^{-10}$ sec. The spatial distribution of the positrons as a result of scattering events during the thermalization process is usually described by the implantation profile of the implanted positrons. The mean implantation depth $\bar{z}$ (in Å), for a uniform material is approximated by,

$$\bar{z} = AE^{n} \tag{5.3.2}$$

where the coefficient A is given empirically[95] by $\sim 332\rho^{-1}$ where ρ is the target density in g/cm^3, and E is the incident energy in keV. The parameter n is about 1.6 for most materials [96]. Sometimes n is also used as an energy and material dependent parameter, particularly for high Z materials[97]. Also it has been reported that the coefficient A depends upon the material of the target and the energy of the implanted positrons [98]. Monte Carlo simulations carried out for the implantation profile, P(z), of the positrons has been found to fit well a Makhovian distribution[99], is given as,

$$P(z) = \frac{mz^{m-1}}{z_0^m} \exp\left[-(\frac{z}{z_0})^m\right] \tag{5.3.3}$$

where $z_0 = \frac{2\bar{z}}{\sqrt{\pi}}$, is the mean implantation depth. In previous work, it has been found that the derivative of Gaussian distribution (m = 2, in the

Makhovian distribution) gives a good approximation to the implantation profile[100-101] and is given as,

$$P(z) = \frac{2z}{z_0^2} \exp\left[-(\frac{z}{z_0})^2\right] \tag{5.3.4}$$

Propagation of the positrons after thermalization is usually well described by the diffusion equation[102-103].

The positron density n(z,t) as a function of their position z and time t can be described by the diffusion equation[104] as,

$$\frac{\partial n(z,t)}{\partial t} = D\frac{\partial^2 n(z)}{\partial z^2} - \varepsilon(z)e\frac{D}{kT}\frac{\partial n(z)}{\partial z} - \frac{n(z)}{\tau_{eff}} + \dot{n}_0(z) \tag{5.3.5}$$

where D is the positron diffusion coefficient, T is the temperature, k is the Boltzmann constant, ε is the electric field, e is the positron charge, $\dot{n}_0(z)$ is the rate at which thermalized positrons are implanted at depth z, and τ_{eff}^{-1} is the effective lifetime of the positrons. This effective lifetime can further be expressed as,

$$\tau_{eff}^{-1} = \tau_{bulk}^{-1} + \mu C_d \tag{5.3.6}$$

where τ_{bulk} is the lifetime of the positrons in the bulk, μ is the specific trapping rate, and C_d is the defect concentration in the solid.

Under steady state conditions, i.e. $\frac{\partial n}{\partial t} = 0$, the time dependent diffusion equation reduces to an ordinary linear second-order diffusion equation, given as [104],

$$\frac{d^2 n(z)}{dz^2} - \frac{1}{\Lambda}\frac{dn(z)}{dz} - \frac{n(z)}{L^2} + \frac{\dot{n}_0(z)}{D} = 0 \tag{5.3.7}$$

where $L = (D\tau_{eff})^{1/2}$ is the positron diffusion length and $\Lambda = kT/\varepsilon e$ is a parameter with dimensions of length which characterizes the electric field ε.

Since only the relative fraction of positrons annihilating is required in the data analysis, Eq. (5.3.7) is normalized with respect to the total positrons deposit rate. The positron deposit rate $\dot{n}_0(z)$ in Eq. (5.3.6), is then modified to the normalized positron implantation profile. A complete solution to the diffusion equation in Eq. (5.3.7), can be found elsewhere [102,103].

The typical approach in studies of multilayered structures is to assume that each layer is homogeneous but distinctive from each other. The resultant lineshape S-parameter for these structures is then the average of the S-parameter values of the various layers, weighted by their respective annihilation fraction F and is given as [92],

$$S = \sum_{i=0}^{N} S_i F_i \tag{5.3.8}$$

where N is the total number of layers. S_i and F_i in Eq. (5.3.8) are the S-parameter and the annihilation fraction of positrons in the i^{th} layer respectively. The surface contribution is represented by the i = 0 term. The annihilation fraction F_i is obtained by the solution of Eq. (5.3.7) and represents the fraction of positrons annihilated in the i^{th} layer. Typically data analysis is performed by the simulation of the experimental S-parameter vs energy E, curves in Eq. (5.3.8). A computer code called Variable Energy Positron Fit (VEPFIT) [105] is widely used for modelling and fitting data to the model from positron depth profile experiments and S-parameter vs energy measurements. This program solves the one dimensional, steady state, diffusion annihilation equation (Eq. (5.3.7)), with a Gaussian derivative implantation profile for the positrons.

For multi layered structures with different material densities, an effective implantation profile $P_{eff}(E,z)$, is calculated by scaling the depth dependent density $\rho(z)$, with respect to the substrate density ρ_0. The modified implantation profile[106] is given as,

$$P_{eff}(E,z) = \frac{\rho(z)}{\rho_0} P(E,z') \tag{5.3.9}$$

where

$$z' = \int_0^z \frac{\rho(z)}{\rho_0} dz \tag{5.3.10}$$

where P(E,z) is the implantation profile for a constant density material, with a substrate density ρ_0.

4. *Activation Energy of Hydrogen in $SiO_2/Si(100)$*

It is common practice to use hydrogen to passivate the dangling bonds and hence improve the electrical properties of the devices [77,107]. It has been observed [77] that hydrogen can passivate interface states of the SiO_2/Si systems and can also alter the fixed and mobile charge in the oxide layer. The abundance of hydrogen in many fabrication processes and its impact on the properties of the SiO_2/Si system, has led to much research activity directed towards more understanding of its interaction with SiO_2/Si based devices. Here an effort is made to measure the activation energy of hydrogen from interface states of this technologically important $SiO_2/Si(100)$ system, with the use of Doppler broadening annihilation spectroscopy. The positrons has the tendency to get trapped at defect sites which happen to be sensitive to hydrogen trapping [108-110] also.

The samples used in this experiment had an oxide layer of 1172 Å, grown in dry O_2 under no HCl, on both n– and p–type Si(100) substrate with no post oxidation forming gas anneal.

The samples were annealed from room temperature to 700 C, in steps of 50 C *in situ*. The annealing process was carried out for 30 min. for each temperature and during annealing the base pressure of the target chamber ranged from 1×10^{-8} to the high 10^{-8} torr. For annealing, the samples were resistively heated by a tantalum foil in contact with the back side of the silicon. The temperature was measured with a K–type Chromel–Alumel thermocouple in contact with the oxide side of the sample. Temperature measurements with this arrangement were estimated to be accurate to within ± 20 C [111].

In order to observe the recovery of the interface states during these experiments, the samples were exposed to atomic hydrogen after the completion of the annealing cycles. The samples were maintained at 300 C during exposure to the atomic hydrogen. The atomic hydrogen for this post annealing treatment was obtained by dissociating molecular hydrogen in the target chamber with an ionization filament of a vacuum ionization gauge. Typically, for these experiments, the total hydrogen exposure was in $\sim 1.4 \times 10^7$ Langmuir (1 L = 10^{-6} torr–sec).

The S–parameter was measured for different incident energies E, of the positrons. A typical S–E curve for the SiO_2/Si system is shown in Fig.

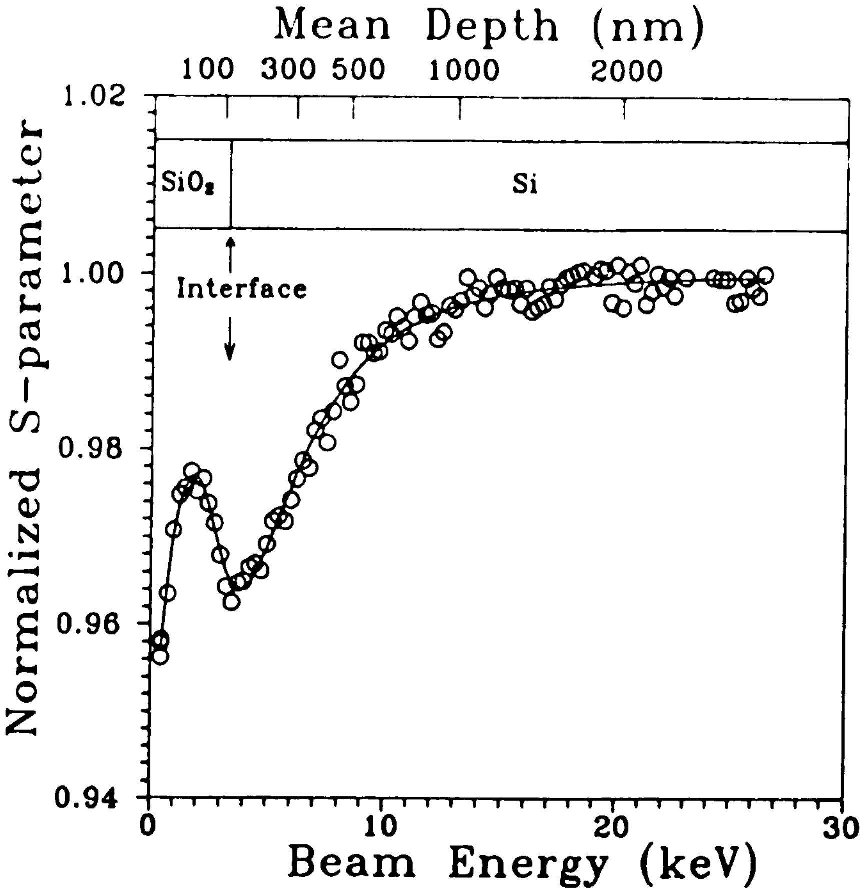

Figure 5.4.1 The S *vs* E spectrum shown above is typical for SiO_2/Si systems and shows distinct S-parameter values for the surface, oxide, interface, and the bulk silicon regions.

5.4.1. The data shows distinct signals corresponding to the surface, oxide, interface, and the bulk silicon regions [112].

Usually, a high value for the oxide S-parameter and a low value for the interface S-parameter is indicative of a good quality oxide layer and a good interface respectively [92]. Fig. 5.4.2 and Fig. 5.4.3 show the normalized S-parameter curves corresponding to different annealing temperatures, for n- and p-type substrate Si(100) respectively. The S-parameter shown in Fig. 5.4.2 and Fig. 5.4.3 are normalized to the bulk silicon S-parameter value. For 5×10^5 counts for each energy, the typical errors in the normalized S-parameter was 0.0011. For these measurements, the sample was allowed to attain the room temperature before starting the measurements. These curves show that the normalized S–parameter for the $SiO_2/Si(100)$ interface, for both n– and p–type substrate, undergoes substantial changes during annealing. The essential features of this behavior are more obvious from the data in Fig. 5.4.4 and Fig. 5.4.5, for n– and p–type substrate respectively. From Eq. (5.3.2), an implantation energy of ~ 4.0 keV corresponds to a mean penetration depth of 100 nm. Fig. 5.4.4 and Fig. 5.4.5 shows the curves for the normalized S - parameter at 4.5 keV incident energy of the positrons, corresponding to the interface region of the oxide and the substrate.

S–parameter goes to a minima at annealing temperature of about ~ 250 C, then increases with higher annealing temperatures and finally saturates at ~ 650 C. The decrease in S–parameter corresponding to the interface at ~ 300 C can be explained by the fact that hydrogen is liberated from the oxide layer [107,113] around this temperature. This liberated hydrogen then diffuses to the interface, passivates the unoccupied trap sites at the interface, and reduces the interface state density. According to the present understanding of positron behavior in SiO_2/Si systems, positrons and hydrogen prefers to be trapped at the same trap site, so that positrons will give a high S–parameter value if trapped at an activated site at the interface and a low value if the trap site is passivated with hydrogen. This argument tends to support the correlation between the behavior of S–parameter and the interface state density [92]. The increase in interface S–parameter at

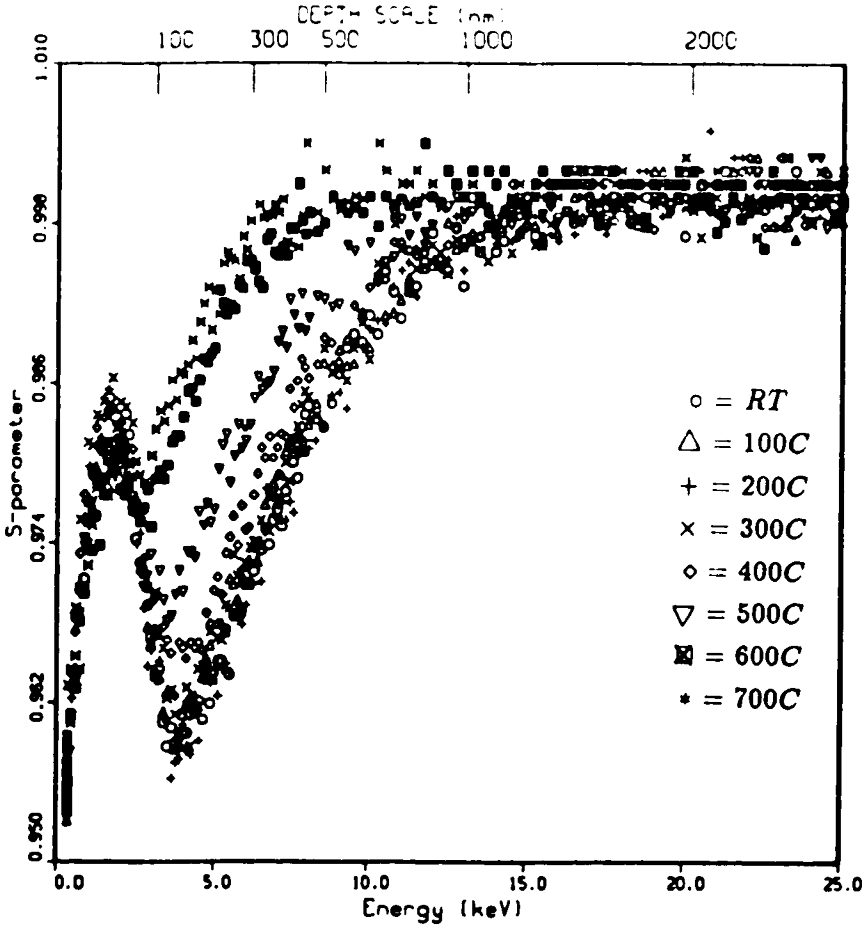

Figure 5.4.2 The normalized S–parameter *vs* E curves for a n–type substrate for different annealing temperatures. For clarity, the curves are shown for each 100 C annealing temperature steps. However the measurements were carried out in steps of 50 C. All measurements were performed after the sample was cooled down to room temperature.

higher annealing temperature can be attributed to activation of the hydrogen from trap sites at the interface, and causing an increase in the interface trap density.

The changes in S–parameter at interface during annealing are associated with activation of hydrogen from trap sites, as verified by exposing the

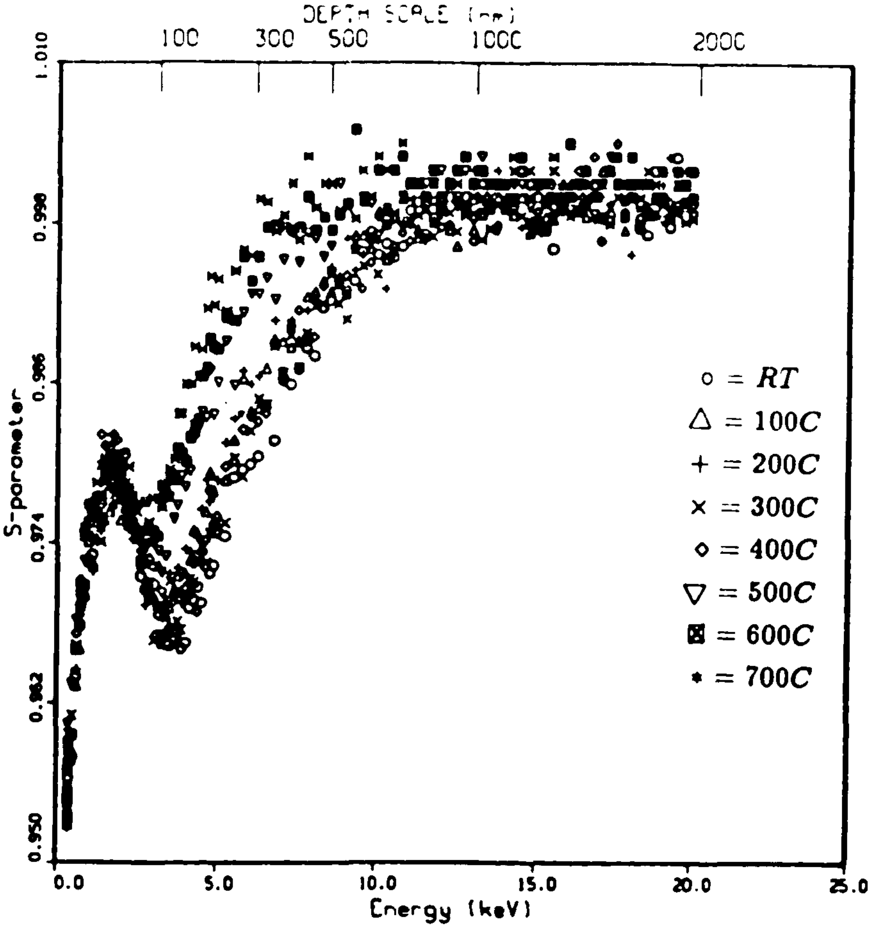

Figure 5.4.3 The normalized S-parameter *vs* E curves for a p-type substrate for different annealing temperatures. For clarity, the curves are shown for each 100 C annealing temperature steps. However, the measurements were carried out in steps of 50 C. All measurements were performed after the sample was cooled down to room temperature.

samples to atomic hydrogen after the annealing cycle, shown for a n-type substrate in Fig. 5.4.6. The recovery of S-parameter at interface is consistent with previous measurements [108,111].

Analysis to obtain the activation energy of hydrogen is carried out by considering a series of isochronal annealing processes at equally spaced

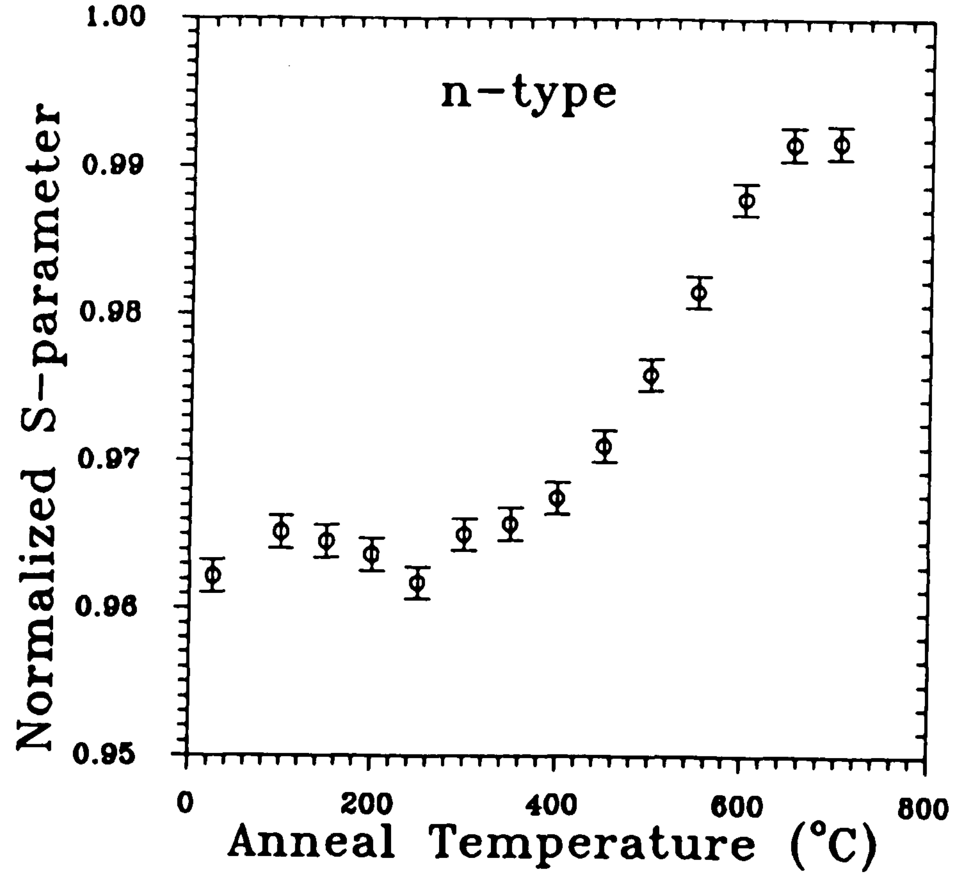

Figure 5.4.4 The normalized S−parameter *vs* annealing temperature for a n−type substrate, at an implantation energy of 4.5 keV. The annealing measurements were carried out in steps of 50 C. All measurements were performed after the sample was cooled down to room temperature.

temperatures T_i, for $i = 0, \ldots, N$ of duration τ sec. The hydrogen content $\mathcal{N}_H(i)$ at the beginning of the i^{th} cycle is given as [111],

$$\frac{d\mathcal{N}_H(i)}{dt} = -\mathcal{N}_H(i) K_0 \exp(-\frac{\mathcal{E}}{k_B T_i}) \tag{5.4.1}$$

where K_0 is the vibrational frequency, $\mathcal{E}$ is the activation energy, and k_B is the Boltzmann constant. It is assumed here that this isochronal annealing

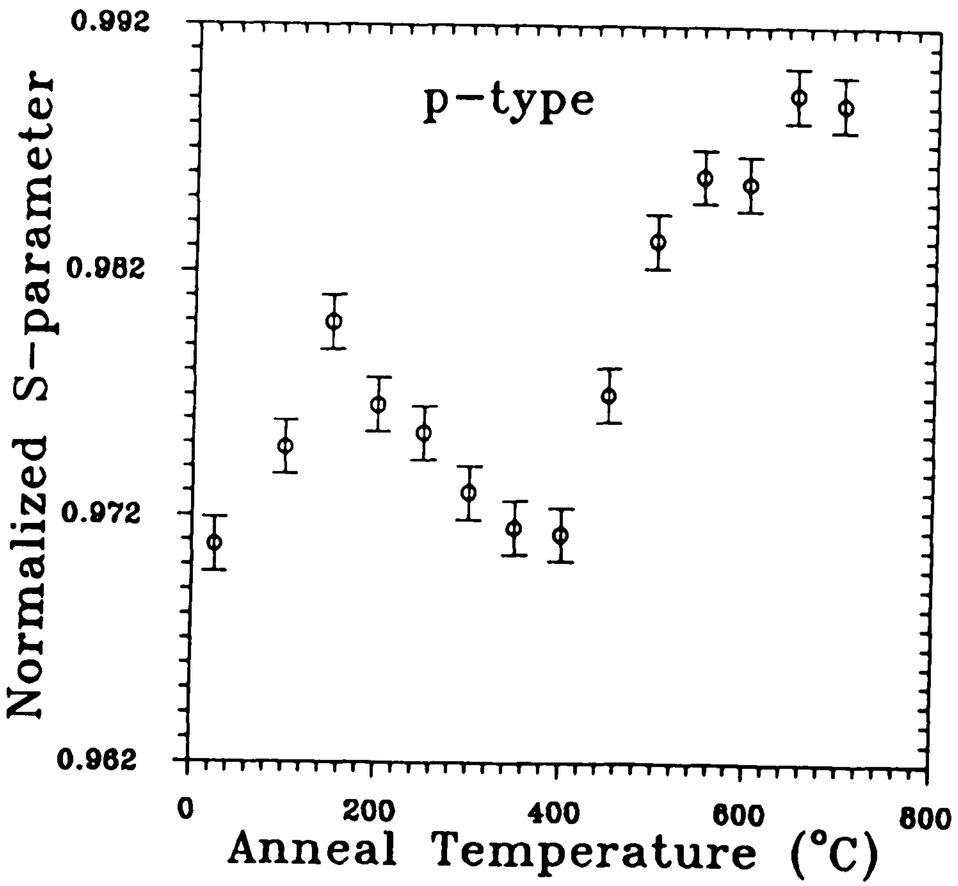

Figure 5.4.5 The normalized S−parameter *vs* annealing temperature for a p−type substrate, at an implantation energy of 4.5 keV. The annealing measurements were carried out in steps of 50 C. All measurements were performed after the sample was cooled down to room temperature.

is a first order process. Quantitatively, S−parameter at the interface can be taken proportional to the hydrogen content, $\mathcal{N}_H$. With this assumption, the activation energy can be written [111],

$$\mathcal{E} \simeq k_B T_m \ln\left[\frac{K_0 \tau}{\ln\left(\frac{T_f - T_i}{T_f - T_i - 2\Delta T}\right)}\right] \tag{5.4.2}$$

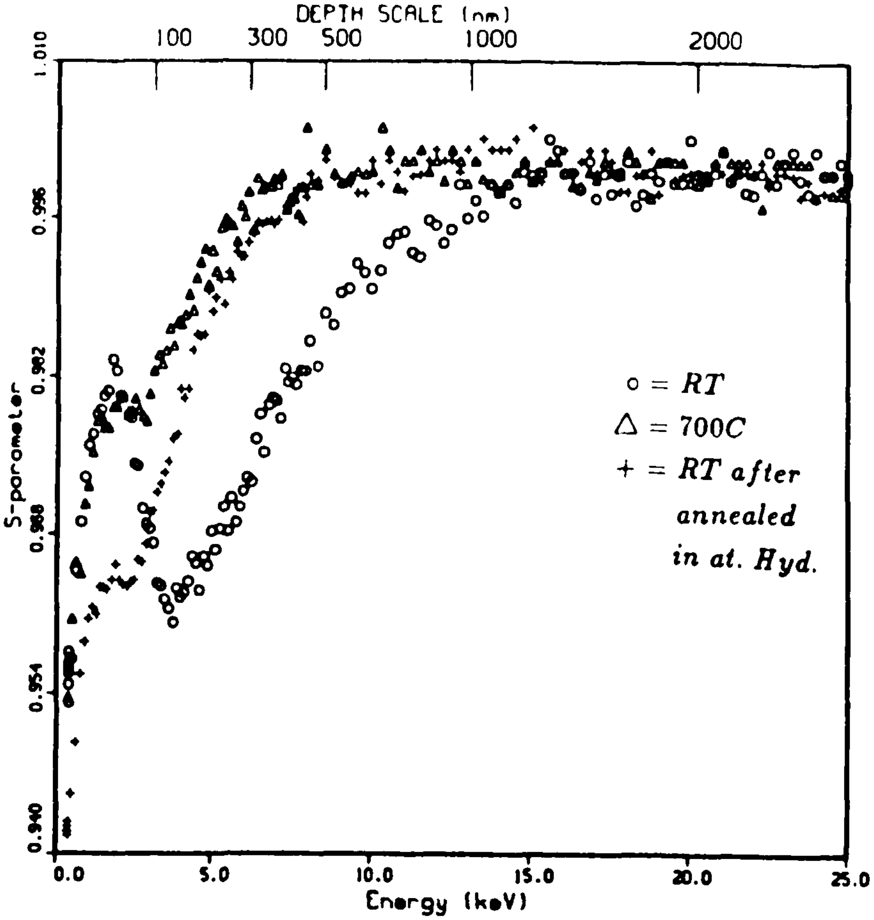

Figure 5.4.6 The normalized S-parameter *vs* E curves for an oxide on a n-type substrate. The measurements were carried out first at room temperature, then sample was annealed at 700 C for 30 min. *in situ*, and finally it was exposed to atomic hydrogen at 300 C for 30 min. and subsequently cooled down in atomic hydrogen ambient before the measurements.

where T_f and T_i are shown in Fig. 5.4.7. The parameter T_m is $T_m = (T_i + T_f)/2$ and Δ T is the step size in annealing temperature. In Eq. (5.4.2), the step size Δ is arbitrary but the activation energy is unique. The change in step size will change the total amount of time spent for carrying out the process of isochronal annealing and hence will affect the shape of the annealing curve. This change in shape of the annealing curve translates into the change in parameters such as T_i, T_f, and T_m, used in the relation for calculation of activation energy of hydrogen.

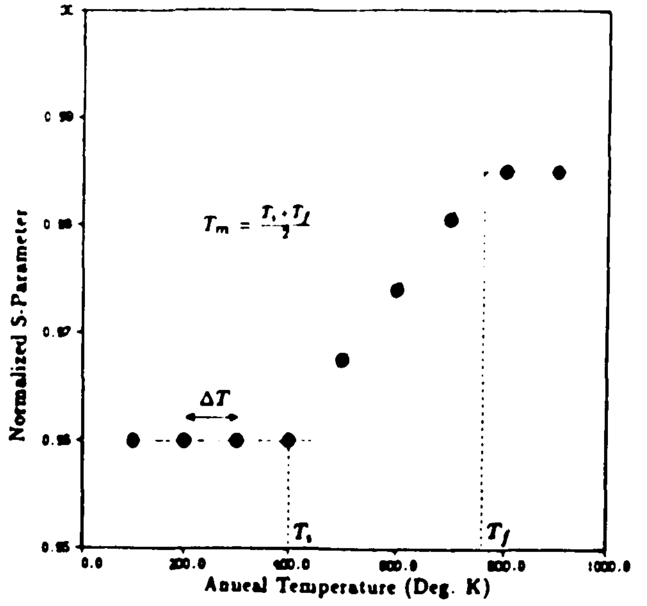

Figure 5.4.7 Schematic of the normalized S–parameter *vs* annealing temperature, showing different parameters used in the calculation for the activation energy in Eq. (5.4.2). (from ref. 111)

For an oxide on n–type Si(100) substrate, the parameters required for the calculations for the activation energy (as indicated in Fig. 5.4.7) were obtained from Fig. 5.4.4. Using appropriate values of T_i = 653.6 K, T_f = 925.4 K, T_m = 789.5 K, and ΔT = 50 K from Fig. 5.4.4 in Eq. (5.4.2), resulted in an activation energy for hydrogen $\mathcal{E}$ of 2.60 (6) eV. For this calculation, the vibrational frequency K_0, was taken to be 10^{13} sec^{-1}. Similarly, for an oxide on p–type Si(100) substrate, using appropriate values of T_i = 615.86 K, T_f = 887.29 K, T_m = 751.58 K from Fig. 5.4.5, and ΔT = 50 K, the activation energy for hydrogen was $\mathcal{E}$ = 2.47 (6) eV. The activation energy for hydrogen is dependent on the methods used to grow the oxide films. The values observed in our experiments are in reasonable agreement with the values observed in previous experiments [111,112].

5. *Study of Irradiated SiO_2/Si(100)*

The studies of radiation damage on the oxides in SiO_2/Si(100) is of great interest because of its consequences for the performance of this cornerstone of the microelectronics industry [114]. Exposure of devices to ionizing radiation such as X−rays, γ−rays, electrons, and ions can cause severe degradation of device performance and operating life time. On irradiation, the oxide and the interface layers suffers significant damage. This damage could consist of buildup of the trapped charges in the oxide, an increase in the number of interface traps and an increase in the number of bulk oxide traps.

An effort is made here to investigate the creation of defects in the oxides, irradiated with X−rays and γ−rays, with the use of Positron Annihilation Spectroscopy (PAS). The dominant type of defect in the irradiated oxide layers has been previously identified by electron spin resonance (ESR) technique [115−117] as E′ centers. An E′ center is a trivalent silicon atom that has an unpaired electron in the dangling orbital and is back bonded to three oxygen atoms. The strained Si−O bond in the oxide layer is easily broken by ionizing radiation and can form associated nonbridging oxygen and a trivalent silicon structure, i.e. an E′ center.

The samples used in this experiment had a oxide layer of 1172 Å, grown in dry O_2 under no HCl, on both n– and p-type Si(100) substrates with no post-oxidation forming gas anneal. These samples were irradiated with X-rays at the National Synchrotron Light Source (NSLS) X-ray beamline with doses in the range of 50–2000 mJ/cm^2, with an average energy of 1 keV. The γ-ray irradiation was carried out at the ^{60}Co gamma pool facility at Brookhaven National Laboratory (BNL). The irradiation was carried out at a temperature of 10 C. Some samples were exposed to a cumulative radiation dose ranging from 7×10^4 Rad to 9×10^6 Rad (1 Rad = 100 ergs/gm), at a constant dose rate of 7.3×10^3 Rad/min, while others were exposed to a cumulative dose of 1×10^5 Rad, at different dose rates ranging from 100 Rad/min to 1.8×10^4 Rad/min. Measurements on some samples were carried out immediately after irradiation, while others were allowed to age for few weeks at room temperature before measurement. The positron beam intensity during these measurements was $\sim 5 \times 10^5$ e^+/sec, too low to produce any measurable radiation damage during the experiment.

S-parameter measured for different beam energies E, for both unirradiated and irradiated samples is shown in Fig. 5.5.1. The data in Fig. 5.5.1 is normalized to the silicon bulk value, S_b. The bulk S-parameter, S_b, is calculated by taking the average of the measured S-parameter values in the S-E data set for energies greater than 15 keV. At a penetration depth of 50 nm, S-parameter for the oxide layer of the irradiated SiO_2/Si(100) sample shows

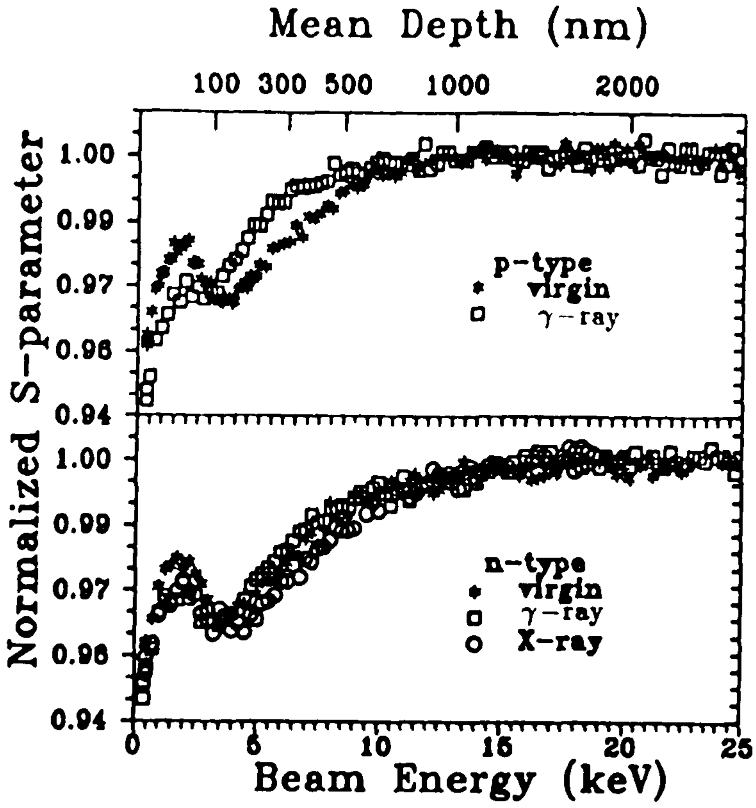

Figure 5.5.1 S-parameter *vs* E for 1172 Å thick oxide layer on n- and p-type Si(100) substrate, for both unirradiated and irradiated samples with X-rays and γ-rays. For the X-ray case, the sample was exposed to X-rays of an average energy of 1 keV and a total cumulative dose of 500 mJ/cm^2. The cumulative dose for the γ- rays irradiated sample was 1 × 10^5 Rad, at a dose rate of 1.8 × 10^4 Rad/min. Other cumulative doses and different dose rates measurements, not shown here, showed similar behavior.

a change as compared with the unirradiated sample, which could be due to defects created by irradiation. These changes in S-parameter are found to be independent of the dopant type, irradiation dose rate, and cumulative dose of up to 9 × 10^6 Rad. Also there was no indication that these defects annealed out with time, when the samples stored for few weeks at room temperature. The drop in the value of S–parameter in the oxide layer suggests that positrons are annihilating with defect sites created during irradiation and, together with the information that strained Si–O bonds in the oxide are easily broken during the irradiation process, leads to the suggestion that this change in S–parameter could be due to these broken strained bonds. It is also observed that S–parameter value at the interface increases in the irradiated samples. Usually the interface states are passivated with hydrogen but when irradiated, perhaps this hydrogen is activated out of these states, leaving a dangling bond at the interface. These changes in the S–parameter at the interface are consistent with previous measurements done on the hydrogen activation energy with PAS [111] and the results discussed in the last section.

The series of S–E curves in Fig. 5.5.2 correspond irradiated samples annealed at different temperatures. Fig. 5.5.3 shows the change in S–parameter at a fixed energy of 2 keV, which corresponds to ~ 50 nm inside the oxide layer of the $SiO_2/Si(100)$ sample. It is evident from the S–parameter *vs* annealing temperature curves at 2 keV that the S–parameter value recovers to the value corresponding to the unirradiated sample around 250 C (±25 C). Isochronal annealing for these measurements was carried out for 30 min. at each temperature.

Annealing of defects created due to the irradiation of the sample with γ–rays at this temperature suggests that these defects are E' centers. These

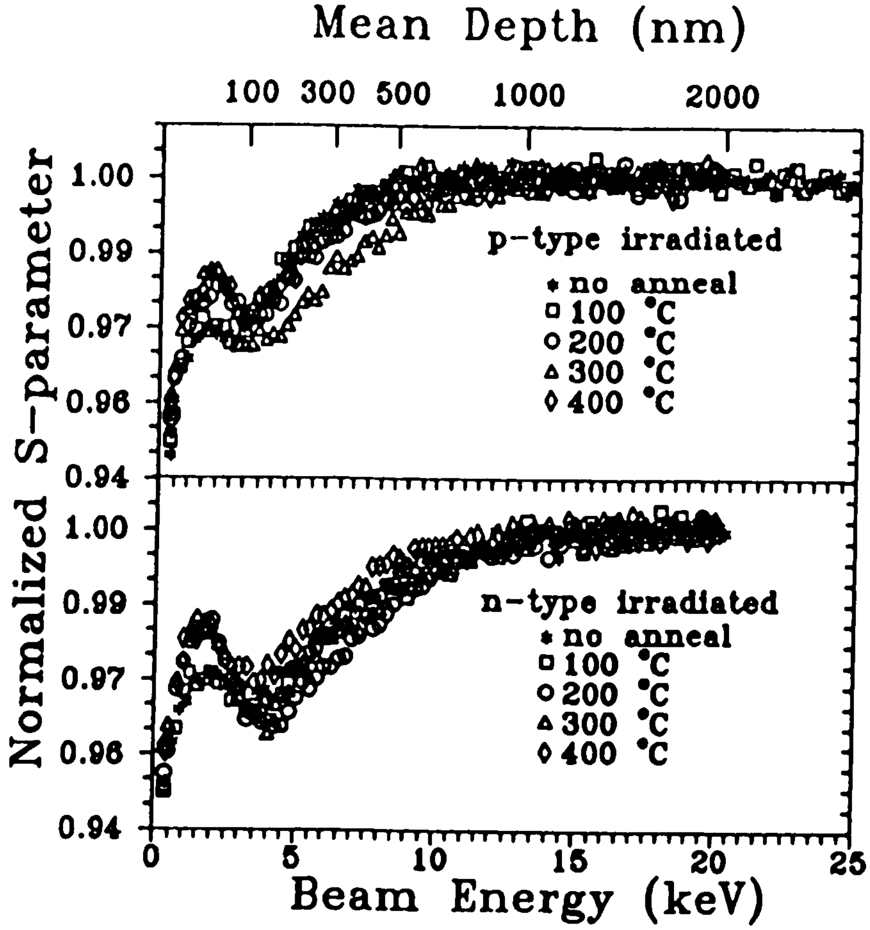

Figure 5.5.2 S-parameter *vs* E for γ-ray irradiated $SiO_2/Si(100)$, at different temperatures in steps of 100 C, although the measurements were carried out in steps of 50 C. The sample for this measurement had a cumulative dose of 1×10^5 Rad, at a dose rate of 1.8×10^4 Rad/min.

centers are known to start annealing out rapidly around these annealing temperatures [118-121].

Fitting of the data in Fig. 5.5.1 was carried out with a program called VEPFIT [105]. A three layer model was used to fit the experimental data. The diffusion length, electric field, and the S-parameter of each layer was varied to obtain the best fit to the data. The diffusion length of the positrons in

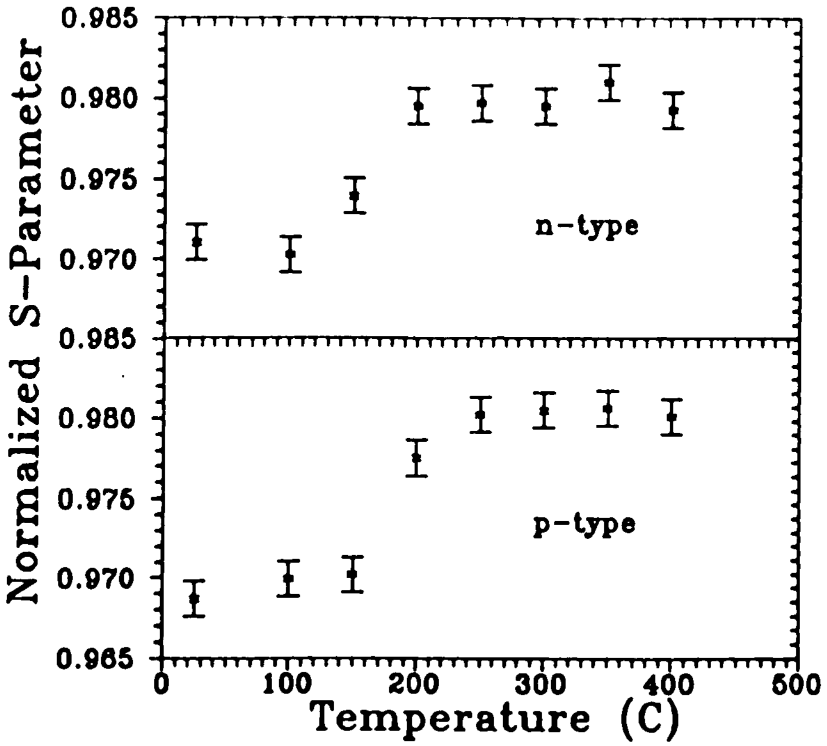

Figure 5.5.3 S-parameter *vs* annealing temperature for γ-rays irradiated SiO_2/Si(100). The plotted S-parameter is measured at 2 keV implantation energy (which corresponds to ~ 50 nm deep inside the oxide layer) and is extracted from the S-parameter *vs* energy curves at different temperatures in Fig. 5.5.4.

the irradiated and unirradiated samples was found to be within the errors associated with the fitting model. The fitted normalized S - parameter for the oxide on a n-type substrate changes on irradiation with γ-rays from 0.9800 (11) to 0.9701 (11), whereas the S-parameter for the interface changes from 0.9276 (11) to 0.9365 (11). The S-parameter values obtained for the oxide grown on a p-type substrate also changes in a similar manner from 0.9200 (11) to 0.9325 (11) for the interface, while from 0.9804 (11) to 0.9709 (11) for the oxide layer.

In related work with ion implantation (B and Si) on SiO_2/Si structures, much larger changes in S-parameter of the oxide layer were produced as compared to the present experiment. The annealing behavior observed in irradiated sample was clearly different from that of the ion implanted oxides. The different isochronal annealing behavior and the correlation with ESR measurements has indicated the dominance of other kinds of defects such as nonbridging-oxygen hole center (NBOHC), peroxy radicals (PR), and others [122] [123]. The changes in S-parameter and the correlation with the annealing behavior of the irradiated samples, suggests that there is indication of the presence of E′ centers and these are observed for the first time using Doppler broadening annihilation spectroscopy [124].

Chapter 6.

Summary

This chapter summarizes the results of the work performed for this thesis as described in the previous chapters. The work performed can be broadly divided into three sections. The first is mainly related to the rare gas solid moderator. The second is the design and construction of the time pulsed positronium beam, used to carry out investigations of the pulsed positronium beam. The last section is based on the experiments performed on the $SiO_2/Si(100)$ system, using Positron Annihilation Spectroscopy (PAS). The experiments on the $SiO_2/Si(100)$ systems were mainly concentrated on measurement of the activation energy of hydrogen at the interface of oxide and silicon, and studies of the creation of defects in $SiO_2/Si(100)$ on irradiation with X−rays and γ−rays.

The study of the rare gas solid moderator in this thesis was motivated by the necessity to know the positron moderation efficiency for a bare source in order to obtain a high flux positron beam with an intense ^{64}Cu radioactive source from High Flux Beam Reactor (HFBR) at Brookhaven National Laboratory (BNL). These studies were carried out by constructing a beam line at BNL, utilizing a sealed 350 μCi ^{22}Na radioactive source, with a moderator in different geometrical configurations. The neon moderator in conical geometrical configuration provided an efficiency of $(4.6 \pm 0.1) \times 10^{-3}$ for positron moderation, underestimated by a factor of (3.1 ± 0.5) as compared to the efficiency of a bare radioactive source. Among different rare gas solid moderators investigated, neon in the conical geometry outperformed other rare gas solid moderators by a factor of 6. The conical configuration moderator also performed better by a factor of (2.2 ± 0.2) than the cylindrical configuration moderator. The corrected efficiency for a neon moderator in the conical configuration with a bare ^{22}Na source was as high as $(1.4 \pm 0.2)\%$. This moderator when used with a ^{64}Cu radioactive source from HFBR could provide positron flux as high as 7.8×10^9 e^+/sec. Presently, the neon moderator is in use with a 100 mCi ^{22}Na source in Bldg. 480 at BNL and preparation are underway for its use with a ^{64}Cu radioactive source from HFBR.

In order to continue the previous experiments at BNL on positronium reflection from the surface of a solid, a time pulsed positron beam was built at BNL with the capability to carry out surface sensitive experiments in ultra high vacuum. This beam has the ability to store low energy positrons in a magnetic bottle, with a magnetic mirror at one end and an electrostatic mirror at the other. These stored positrons can then be bunched with the use of a buncher, developed under the direction of Dr. Allen Mills, Jr. at AT&T Bell Laboratory. This buncher when pulsed at a rate of 1 kHz, provides pulses of positrons with a FWHM of 17 nsec, which includes a contribution of 8 nsec from the buncher alone. With this beam line, it is also possible to carry out time of flight measurements and hence energy distribution measurements. Qualitatively it was estimated that the pulses had at least one positron per pulse. In order to obtain a positronium beam, these positron pulses were made to hit a 50 Å carbon foil. The present investigation led to the conclusion that with present positron flux, it is not possible to obtain a good estimate of the efficiency of positronium production and hence more information on the energy and angular distribution of the positronium beam. It is expected that this work will continue with a higher positon flux in Bldg. 480 at BNL. This will be able to provide information on positronium formation efficiency, angular distribution, and energy distribution. Further this positronium beam will be used to carry out investigations on reflection and diffraction of the positronium atoms from solid surfaces. Time of flight measurements would be able to provide useful information on the energy losses of the positronium during their interaction with solid surfaces.

The sensitivity of positrons to defects has shown a great potential in providing useful information on technological important $SiO_2/Si(100)$ systems. The variable energy positron beam at BNL was utilized to carry out experiments on this system. Positron Annihilation Spectroscopy (PAS) was used to measure the activation energy of hydrogen at the interface of oxide and a silicon (100) substrate. In addition to PAS the ESR technique is also frequently used to extract this information. The sensitivity of ESR is due to the paramagnetic nature of the defects, which is not so for positrons. The activation energy of hydrogen at the interface of a $SiO_2/Si(100)$ sample with a n− and p− type substrate was measured to be 2.60(6) eV and 2.47(6) eV respectively. The importance of radiation damage in the device industry led us to carry out investigations on the irradiated samples of $SiO_2/Si(100)$. The irradiation was carried out with X−ray and γ−ray sources at NSLS X−ray beamline and ^{60}Co gamma pool facility at BNL respectively. Using

PAS, it was observed that the oxide layer of $SiO_2/Si(100)$ suffered significant damage. The correlation of the observed change in the S parameter with annealing behavior of the created defects due to irradiation of the sample led us to suggest that these defects were E′ centers, which are trivalent silicon atoms that have an unpaired electron in the dangling orbital and are back bonded to three oxygen atoms. It is expected that in the future the high sensitivity of positrons to defects together with other techniques using positrons such as 2D ACAR and lifetime measurements, will be able to provide defect specific information in SiO_2/Si based systems, which is presently very difficult to obtain with other techniques.

References

1. P. A. M. Dirac, Proc. Cambridge Philos. Soc. 26, 361 (1930).

2. Carl D. Anderson, Science 76, 238 (1932).

3. Carl D. Anderson, Phys. Rev. 41, 405 (1932).

4. Carl D. Anderson, Phys. Rev. 43, 491 (1933).

5. S. Mohorovičić, Astron. Nachr. 253, 94 (1934).

6. M. Deutch, Phys. Rev. 82, 455 (1951).

7. M. Deutch, Phys. Rev. 83, 866 (1951).

8. S. DeBenedetti, C. E. Cowan, and W. R. Ronncker, Phys. Rev. 76, 440 (1949).

9. A. T. Stewart and L. O. Roellig, *Positron Annihilation*, Proceeding of the 1st International Conference on Positron Annihilation, Detroit, New York and London, Academic Press (1965).

10. L. Madanski and F. Rasetti, Phys. Rev. 79, 397 (1950).

11. W. Cherry, Ph.D. Dissertation, 1958 (Princeton University), available from University Microfilms Inc., Ann Arbor, Michigan, USA.

12. K. F. Canter, P. G. Coleman, T. C. Griffith, and G. R. Heyland, J. Phys. B5, L167 (1972).

13. P. J. Schultz, K. G. Lynn, Rev. of Mod. Phys. 60, 701 (1988).

14. K. G. Lynn and A. P. Mills, Jr., in *Positron Solid-State Physics*, Lecture notes for the International School of Physics Enrico Fermi Course

LXXXIII edited by W. Brandt and A. Dupasquier, North Holland, Amsterdam (1983).

15. K. F. Canter, in *Positron Scattering in Gases*, edited by John W. Humberston, and M. R. C. McDowell, New York and London, Plenum Press (1984), p. 219.

16. S. Berko and Hugh N. Pendelton, Annu. Rev. Nucl. Part. Sci. 30, 543 (1980).

17. A. Rich, Rev. Mod. Phys. 53, 127 (1981).

18. L. O. Roellig, M. Weber, S. Berko, B. L. Brown, K. F. Canter, K. G. Lynn, A. P. Mills, Jr., S. Tang, and A. Viescas, in *Atomic Physics with Positrons* edited by J. W. Humberston and E. A. G. Armour, New York, Plenum (1987), p. 283.

19. M. H. Weber, S. Tang, S. Berko, B. L. Brown, K. F. Canter, K. G. Lynn, A. P. Mills, Jr., L. O. Roellig, and A. Viescas, Phys. Rev. Lett. 61, 2542 (1988).

20. S. Tang, Ph.D. Dissertation, 1990 (City University of New York), available from University Microfilms Inc., Ann Arbor, Mich., USA.

21. R. N. West, Adv. Phys. 22, 263 (1973).

22. I. K. MacKenzie, T. L. Khoo, A. B. McDonald, and B. T. A. McKee, Phys. Rev. Lett. 19, 946 (1967).

23. M. H. Weber, Ph.D. Dissertation, 1989 (City University of New York), available from University Microfilms Inc., Ann Arbor, Mich., USA.

24. R. H. Howell, R. A. Alvarez, and M. Stanek, Appl. Phys. Lett. 40, 751 (1982).

25. G. Graff, R. Ley, A. Osipowicz, and G. Werth, Appl. Phys. A 33, 59 (1984).

26. B. Saam, M. Skalsey, and J. Van House, Phys. Rev. C 40, R1563 (1989).

27. C. M. Lederer, Jack M. Hollander, and Isadore Perlamn, *Table of Isotopes*, John Wiley & Sons, New york, London, Sydney, (1967) p. 98.

28. Werner Brandt and Robert Paulin, Phys. Rev. B 15, 2511 (1977).

29. A. P. Mills, Jr., Appl. Phys. Lett. 35, 427 (1979).

30. C. D. Beling and M. Charlton, Contemp. Phys. 28, 241 (1987).

31. E. M. Gullikson, A. P. Mills, Jr., W. S. Crane, and B. L. Brown, Phys. Rev. B 32, 5484 (1985).

32. D. A. Fisher, K. G. Lynn, and D. W. Gidley, Phys. Rev. B 33, 4479 (1986).

33. A. P. Mills, Jr. and W. S. Crane, Phys. Rev. Lett. 53, 2165 (1984).

34. K. F. Canter, Contemp. Phys. 13, 457 (1972).

35. A. P. Mills, Jr. and E. M. Gullikson, Appl. Phys. Lett. 49, 1121 (1986).

36. R. Khatri, M. Charlton, P. Sferlazzo, K. G. Lynn, A. P. Mills, Jr., and L. O. Roellig, Appl. Phys. Lett. 57, 2374 (1990).

37. K. G. Lynn, E. Gramsch, S. G. Usmar, and P. Sferlazzo, Appl. Phys. Lett. 55, 87 (1989).

38. M. Weber, S. Tang, R. Khatri, S. Berko, K. F. Canter, K. G. Lynn, A. P. Mills, Jr., L. O. Roellig, and A. J. Viescas, *Proceeding of the Workshop on Annihilation in Gases and Galaxies*, edited by Richard J. Drachman, NASA Conference Publications 3058 (1990), p. 137.

39. L. Wolfstein and D. G. Ravenhall, Phys. Rev. 88, 279 (1952).

40. T. Chang, T. Hsiaowei, and Li Yaoqing, in *Positron Annihilation*, edited by P. C. Jain, R. M. Singru, and K. P. Gopinathan, World Scientific, Singapore (1985), p. 212.

41. A. Ore and J. L. Powell, Phys. Rev. 75, 1696 (1949).

42. P. A. M. Dirac, Proc. Cambridge Philos. Soc. 26, 361 (1930).

43. G. C. McCoyd, Ph.D. Dissertation, 1965 (St. Johns University), available from University Microfilms Inc., Ann Arbor, Mich., USA.

44. J. Pirenne, Arch. Sci. Phys. Nat. 28, 233 (1946).

45. J. A. Wheeler, *Ann. N. Y. Acad. Sci.* 48, 219 (1946).

46. Michael A. Stroscio, Phys. Reports 22, 215 (1975).

47. D. M. Schrader and Y. C. Jean, *Positron and Positronium Chemistry*, Elsevier, Amsterdam, Oxford, New York, and Tokyo (1988).

48. V. G. Baryshevsky, Phys. Stat. Sol. (B) 124, 619 (1984).

49. V. G. Baryshevsky, O. N. Metelista, V. V. Tikhomirov, S. K. Andrukhovich, A. N. Berestov, B. A. Martsinkevich, and E. A. Rudak, Phys. Lett. A 136, 428 (1989).

50. V. G. Baryshevsky, O. N. Metelitsa, and V. V. Tikhomirov, J. Phys. B 22, 2835 (1989).

51. M. L. Lewis and V. W. Hughes, Phys. Rev. A 8, 625 (1982).

52. Martin Deutsch and Everett Dulit, Phys. Rev. 84, 601 (1951).

53. K. F. Canter, A. P. Mills, Jr., and S. Berko, Phys. Rev. Lett. 34, 177 (1975).

54. A. P. Mills, Jr., S. Berko, and K. F. Canter, Phys. Rev. Lett. 34, 1541 (1975).

55. Steven Chu and A. P. Mills, Jr., Phys. Rev. Lett. 48, 1333 (1982).

56. Steven Chu, A. P. Mills, Jr., and J. L. Hall, Phys. Rev. Lett. 52, 1689 (1984).

57. P. Sferlazzo, S. Berko, and K. F. Canter, Phys. Rev. B 35, 5315 (1987).

58. A. K. Bhatia and Richard J. Drachman, Phys. Rev. A 32, 3745 (1985).

59. A. P. Mills, Jr., Phys. Rev. Lett. 50, 671 (1983).

60. A. P. Mills, Jr., Phys. Rev. Lett. 46, 717 (1981).

61. A. P. Mills, Jr. and William S. Crane, Phys. Rev. A 31, 593 (1985).

62. D. W. Gidley, R. Mayer, W. E. Frieze, and K. G. Lynn, Phys. Rev. Lett. 58, 595 (1987).

63. T. C. Griffith, in *Positron Scattering in Gases*, edited by John W. Humberston and M. R. C. McDowell, Plenum Press, New York and London (1984) p. 53.

64. P. Mandal, S. Guha, and N. C. Sil, J. Phys. B 12, 2913 (1979).

65. P. Khan and A. S. Ghosh, Phys. Rev. A 28, 2181 (1983).

66. P. Khan, P. S. Mazumdar, and A. S. Ghosh, Phys. Rev. A 31, 1405 (1985).

67. R. Khatri, K. G. Lynn, A. P. Mills, Jr., and L. O. Roellig, in *Positron Annihilation*, edited by Z. Kajcsos and C. Szeles, Trans Tech Publications, Switzerland, Germany, UK, Australia, USA (1992), p. 1915.

68. H. Huomo, R. Jones, J. Hurst, A. Vehanen, J. Throwe, S. G. Usmar, and K. G. Lynn, Nucl. Inst. and Meths. A 284, 359 (1989).

69. J. M. Dale, L. D. Hulett, and S. Pendyala, Surf. Interface Anal. 2, 199 (1980).

70. E. Gramsch, J. Throwe, and K. G. Lynn, Appl. Phys. Lett. 51, 1862 (1987).

71. J. D. Jackson, *Classical Electrodynamics*, 2^{nd} edt., John Wiley & Sons, New York, USA (1978).

72. A. P. Mills, Jr., Appl. Phys. 22, 273 (1980).

73. A. P. Mills, Jr., E. D. Shaw, R. J. Chichester, and D. M. Zuckerman, Rev. of Sci. Inst. 60, 825 (1989).

74. A. P. Mills, Jr., in *Positron Scattering in Gases*, edited by J.W. Humberston and M. R. C. McDowell, Plenum, New York (1983), p. 121.

75. J. L. Wiza, Nucl. Inst. and Meths. 162, 587 (1979).

76. Arizona Carbon Foils Co., Inc., 2239 East Kleindale Road, Tucson, AZ 85719.

77. E. H. Nicollian and J. R. Brews, *MOS (Metal Oxide Semiconductor) Physics and Technology*, John Wiley & Sons, New York (1982).

78. B. Nielsen, K. G. Lynn, Y. C. Chen, and D. O. Welch, Appl. Phys. Lett. 51, 1022(1987).

79. C. J. Frost and L. Derrick, J. Electrochem. Soc. 104, 547(1957).

80. P. Balk, edt., *The Si–SiO_2 System*, Materials Science Monogrames 32, Elsevier Science Publishers, Amsterdam (1988).

81. S. T. Pantelides, Ed., *The Physics of SiO_2 and its Interfaces*, Pergamon Press, New York (1978).

82. C. R. Helms and B. E. Deal, Ed., *The Physics and Chemistry of SiO_2 and the Si–SiO_2 Interface*, Plenum Press, New York (1988).

83. B. E. Deal, J. Electrochem. Soc. 121, 198C (1974).

84. B. E. Deal, J. Electrochem. Soc. 127, 979 (1980).

85. S. P. Murarka, Appl. Phys. Lett. 34, 587 (1979).

86. B. E. Deal, M. Sklar, A. S. Grove, and E. H. Snow, J. Electrochem. Soc. 114, 266 (1967).

87. T. Sakurai and T. Sugano, J. Appl. Phys. 52, 2889 (1981).

88. R. R. Razouk and B. E. Deal, J. Electrochem. Soc. 126, 1573 (1979).

89. P. L. Castro and B. E. Deal, J. Electrochem. Soc. 118, 280 (1971).

90. P. J. Caplan and E. H. Poindexter, J. Appl. Phys. 50, 5847 (1979).

91. E. H. Poindexter, P. J. Caplan, B. E. Deal, and R. R. Razouk, J. Appl. Phys. 52, 879 (1981).

92. T. C. Leung, Ph.D. Thesis, State University of New York at Stony Brook, 1991 (available from University Microfilms Inc., Ann Arbor, Michigan, USA).

93. I.K. MacKenzie, J. A. Eady, and R. R. Gingerich, Phys. Lett. 33A, 279 (1970).

94. J. L. Campball, Appl. Phys. 13, 365 (1977).

95. A. P. Mills, Jr. and R. Wilson, Phys. Rev. A 26, 490(1982).

96. K. G. Lynn and H. Lutz, Phys. Rev. B 22, 4143(1980).

97. B. Nielsen, K. G. Lynn, T. C. Leung, G. J. van der Kolk, and L. J. van Ijzendoorn, Appl. Phys. Lett. 65, 728(1990).

98. P. Asoka-Kumar and K. G. Lynn, Appl. Phys. Lett. 57, 1634(1990).

99. A. F. Makhov, Sov. Phys. Solid State 2, 1934, 1942, and 1945 (1960).

100. K. G. Lynn, D. M. Chen, B. Nielsen, R. Pareja, and S. Myers, Phys. Rev. B 34, 1449 (1986).

101. A. Vehanen, K. Saarinen, P. Hautojarvi, and H. Huomo, Phys. Rev. B 35, 4606 (1987).

102. A. P. Mills, Jr. and C. A. Murray, Appl. Phys. 21, 323 (1980).

103. H. H. Jorch, K. G. Lynn, and T. McMullen, Phys. Rev. B 30, 93 (1984).

104. K. G. Lynn, D. O. Welch, J. Throwe, and B. Nielsen, Inter. Materls. Rev. 36, 1 (1991).

105. A. van Veen, H. Schut, J. de Vries, R. A. Hakvoort, and M. R. IJpma, AIP Conference Proceedings 218, *Positron Beams for Solids and Surfaces*, edited by P. J. Schultz, G. R. Massoumi, and P. J. Simpson, p. 171 (1990).

106. A. Vehanen, K. Saarinen, P. Hautojarvi, and H. Huomo, Phys. Rev. B 35, 4606 (1987).

107. K. L. Brower, Phys. Rev. B 42, 3444 (1990).

108. K. G. Lynn, B. Nielsen, and D. O. Welch, Can. J. Phys. 67, 818 (1989).

109. P. Hautojärvi, H. Huomo, P. Saariaho, A. Vehanen, and J. Yli Kauppula, J. Phys. F 13, 1415 (1983).

110. H. E. Hansen, R. Talja, H. Rajainmäki, H. K. Nielsen, B. Nielsen, and R. M. Nieminen, Appl. Phys. A 36, 91 (1985).

111. P. Asoka--Kumar, K. G. Lynn, T. C. Leung, B. Nielsen, and X. Y. Wu, J. Appl. Phys. 69, 6603 (1991).

112. B. Nielsen, K. G. Lynn, Y. C. Chen, and D. O. Welch, Appl. Phys. Lett. 51, 1022 (1987).

113. T. Fare, A. Spetz, M. Armgarth, and I. Lundstrom, J. Appl. Phys. 63, 5507 (1988).

114. T. P. Ma and Paul V. Dressendorfer, edt., *Ionization Radiation Effects in MOS Devices and Circuits*, John Wiley & Sons, New York (1989).

115. R. A. Weeks, J. Appl. Phys. 27, 1376 (1956).

116. R. H. Silsbee, J. Appl. Phys. 32, 1459 (1961).

117. F. J. Feigl, W. B. Fowler, and K. L. Yip, Solid State Commun. 14, 225 (1974).

118. V. Danchenko, U. D. Desai, and S. S. Brashears, J. Appl. Phys. 39, 2417 (1968).

119. S. W. McKnight in *The Physics of MOS Insulators*, edited by G. Lucovsky, Pergamon Press, Elmsford, New York (1980), p. 137.

120. D. L. Griscom, J. Appl. Phys. 58, 2524 (1985).

121. F. B. McLean, E. H. Boesch, Jr., and T. R. Oldham, in *Ionizing Radiation Effects in MOS Devices and Circuits*, edited by T. P. Ma and Paul V. Dressendorfer, John Wiley & Sons, New York (1989), p. 164 & 169.

122. B. Nielsen *et al.*, in preparation (1992).

123. M. Fujinami and N. B. Chilton, submitted to Appl. Phys. Lett., (1992).

124. R. Khatri, P. Asoka-Kumar, B. Nielsen, and K. G. Lynn, in preparation.